



**Università
degli Studi
di Ferrara**

DOTTORATO DI RICERCA IN

Scienze chimiche

CICLO XXXIII

COORDINATORE

Prof. Cavazzini Alberto

**Advanced Electrolyte and Electrode Materials for High-
performance Lithium Batteries**

Settore Scientifico Disciplinare CHIM/02

Dottoranda

Dott. Shuangying Wei

Tutore

Prof. Jusef Hassoun

Anni 2017/2020

Abstract

ENGLISH: The storage capabilities, longevity, and safety characteristics in existing rechargeable lithium-ion batteries (LIBs) using graphite as anode materials, are regarded as insufficient to meet the vigorous requirements of energy storage market. A renewed interest is now devoted towards high-energy lithium-metal anode (attractive theoretical specific capacity of 3860 mAh g^{-1}) though the issues of uncontrolled lithium dendrite growth need to be resolved urgently. To this end, the focus of this thesis is optimization of suitable electrolyte solutions that can mitigate the issues affecting the lithium metal anode, and search for alternative anode materials with high Li^+ storage capacity.

Chapter 1 introduces the background knowledge of the world energy demands, focusing on the importance of developing LIBs. **Chapter 2** presents the fundamental concept of lithium battery technologies, including the historical outlook of battery, battery basics, cathode materials, anode materials, electrolytes, and lithium metal batteries. **Chapter 3** reports a description of the used chemical reagents and an overview of the instrumentation principles. The preparation of electrode materials, cell configurations, and working principles of the characterization techniques are detailed in **Chapter 4**.

An electrochemical study of end-capped glymes (diethylene glycol dimethyl ether, DEGDME; triethylene glycol dimethyl ether, TREGDME) dissolving lithium salts, namely, lithium bis(fluorosulfonyl)imide (LiFSI), lithium bis(trifluoromethanesulfonyl)imide (LiTFSI), and lithium bis(pentafluoroethanesulfonyl)imide (LiBETI) as electrolyte solutions for lithium metal batteries is given in **Chapter 5**. The ion transport properties, the lithium/electrolyte interphase characteristics, and the electrochemical stability window of six electrolyte solutions are thoroughly explored. The comparative study indicates that the electrolyte composition has a remarkable effect on the cell performances by using lithium iron phosphate (LFP) cathode and lithium metal anode and indicate the solutions of LiTFSI salt in glymes as the most adequate formulations for possible applications.

High-performance lithium-metal batteries are achieved by using six electrolyte solutions mentioned above, enhanced with a LiNO_3 additive and an olivine cathode, as can be seen in **Chapter 6**. The best Li/LFP battery delivers 154 mAh g^{-1} at C/3 ($1\text{C} = 170 \text{ mA g}^{-1}$) without any decay after 200

cycles. Tests at 1C and 5C show initial capacities of about 150 and 140 mAh g⁻¹, a retention exceeding 70 % after 500 cycles, and suitable electrode/electrolyte interphases evolution.

A NiO@C composite is prepared through an alternative synthesis route involving precipitation of a carbon precursor on NiO nano powder, annealing under argon to form a Ni core, and oxidation at moderate temperature, as shown in **Chapter 7**. The NiO@C exhibits highly improved behavior in a lithium half-cell compared to bare NiO due to faster electrode kinetics and superior stability over electrochemical displacement, leading to a reversible capacity approaching 800 mAh g⁻¹, much-enhanced cycle life, and promising rate capability. The applicability of the NiO@C anode is further investigated in a lithium-ion NiO@C/LiNi_{1/3}Co_{1/3}Mn_{1/3}O₂ cell, which operates at about 2.5 V, delivering about 160 mAh g⁻¹ with respect to the cathode mass. The cell exhibits stable response upon 80 cycles at a C/2 (where 1C is 170 mA g⁻¹ as referred to the positive electrode) rate with coulombic efficiency ranging from 97% to 99%.

ITALIAN: Le capacità di stoccaggio energetico, la longevità e la sicurezza delle batterie litio-ione (LIBs) ricaricabili esistenti che utilizzano la grafite come materiale anodico sono considerate insufficienti per soddisfare i rigorosi requisiti del mercato dell'accumulo di energia. Un rinnovato interesse è ora dedicato all'anodo di litio metallico ad alta energia (capacità specifica teorica di 3860 mAh g^{-1}), sebbene i problemi dovuti alla crescita incontrollata di strutture dendritiche di litio debbano ancora essere risolti. A tal fine, il focus di questa tesi è l'ottimizzazione di soluzioni elettrolitiche in grado di mitigare i problemi che interessano l'anodo di litio metallico, e la ricerca di materiali anodici alternativi con elevata capacità di accumulo di ioni Li^+ .

Il **Capitolo 1** introduce la conoscenza di base delle richieste energetiche mondiali, concentrandosi sull'importanza dello sviluppo di LIBs. Il **Capitolo 2** presenta il concetto fondamentale delle tecnologie delle batterie al litio, inclusa la prospettiva storica della batteria, le basi del dispositivo, i materiali catodici, i materiali anodici, gli elettroliti e le batterie al litio metallico. Il **Capitolo 3** riporta una descrizione dei reagenti chimici utilizzati e una panoramica dei principi della strumentazione. La preparazione dei materiali elettrodici, le configurazioni delle celle e i principi di funzionamento delle tecniche di caratterizzazione sono descritti in dettaglio nel **Capitolo 4**.

Nel **Capitolo 5** viene fornito uno studio elettrochimico di soluzioni elettrolitiche dette "end-capped glymes" (dietilenglicole dimetil etere, DEGDME; trietilenglicole dimetil etere, TREGDME) che dissolvono sali di litio, vale a dire, litio bis(fluorosulfonyl)immide (LiFSI), litio bis(trifluorometansulfonyl)immide (LiTFSI), e litio bis(pentafluoroethanesulfonyl)immide (LiBETI) per batterie al litio metallico. Le proprietà di trasporto ionico, le caratteristiche dell'interfase litio/elettrolita e la finestra di stabilità elettrochimica di sei soluzioni elettrolitiche sono state studiate. Lo studio comparativo indica che la composizione elettrolitica ha un effetto notevole sulle prestazioni delle celle utilizzando il catodo di litio ferro fosfato (LFP) e l'anodo di litio metallico ad alta energia e indicano le soluzioni di sale LiTFSI in glymes come le formulazioni più adeguate per una possibile applicazione.

Le batterie al litio metallico ad alte prestazioni vengono ottenute utilizzando le sei soluzioni elettrolitiche sopra menzionate migliorate con l'additivo LiNO_3 , e un catodo olivinic, come viene mostrato nel **Capitolo 6**. La migliore batteria Li/LFP eroga 154 mAh g^{-1} a C/3 ($1\text{C} = 170 \text{ mA g}^{-1}$) senza alcun decadimento dopo 200 cicli. I test a 1C e 5C mostrano capacità iniziali di circa 150 e

140 mAh g⁻¹, una ritenzione superiore al 70% dopo 500 cicli e un'adeguata evoluzione dell'interfase elettrodo/elettrolita.

Un composto NiO@C viene preparato attraverso un percorso di sintesi alternativo che coinvolge la precipitazione di un precursore di carbonio su polvere nanometrica di NiO, la ricottura sotto argon per formare un nucleo di Ni, e l'ossidazione a temperatura moderata, come mostrato nel **Capitolo 7**. Il materiale NiO@C mostra un comportamento altamente migliorato in una semicella al litio rispetto al semplice NiO grazie alla cinetica degli elettrodi più rapida e alla superiore stabilità rispetto al trasferimento elettrochimico, portando a una capacità reversibile che si avvicina a 800 mAh g⁻¹, un ciclo di vita molto migliorato e una promettente rate capability. L'applicabilità dell'anodo NiO@C è ulteriormente studiata in una cella litio-ione NiO@C/LiNi_{1/3}Co_{1/3}Mn_{1/3}O₂, che opera a circa 2.5 V erogando 160 mAh g⁻¹ rispetto alla massa del catodo. La cella mostra una risposta stabile su 80 cicli ad una corrente di C/2 (dove 1C è 170 mA g⁻¹ riferendosi all'elettrodo positivo) con efficienza coulombica che va dal 97% al 99%.

List of abbreviations

Symbol	Definition
AC	Alternating Current
BSD	Backscattered electron detector
BSEs	Back scattered electrons
CV	Cyclic voltammetry
CE	Counter electrode
CPE	Composite polymer electrolyte
DEGDME	Diethylene glycol dimethyl ether
DMC	Dimethyl carbonate
EC	Ethylene carbonate
EDS	Energy dispersive X-ray spectroscopy
EELS	Electron energy loss spectroscopy
EIS	Electrochemical impedance spectroscopy
EVs	Electric vehicles
ESW	Electrochemical stability window
FFT	Fast Fourier transformation
FWHM	Full width at half maximum
GPE	Gel polymer electrolyte
HEVs	Hybrid electric vehicles
HPEVs	Hybrid plug-in electric vehicles
JCPDS	Joint committee on powder diffraction standards
ICSD	Inorganic crystal structure database
ILs	Ionic liquids
LiFSI	Lithium bis(fluorosulfonyl)imide

LiTFSI	Lithium bis(trifluoromethanesulfonyl)imide
LiBETI	Lithium bis(pentafluoroethanesulfonyl)imide
LCO	Lithium cobalt oxide
LISICON	Lithium-ion super ionic conductor
LFP	Lithium iron phosphate
LIBs	Lithium-ion batteries
LMO	Lithium manganese oxide
LNO	Lithium nickel oxide
LSV	Linear sweep voltammetry
LiPF ₆	Lithium hexafluorophosphate
OCV	Open circuit voltage
NASICON	Sodium ion super ionic conductor
NCA	Lithium nickel cobalt aluminate oxide
NLLSQ	Nonlinear least squares
NMP	N-methyl-2-pyrrolidone
NCM	Lithium nickel cobalt manganese
PAN	Poly(acrylonitrile)
PDF	Powder diffraction file
PEO	Poly(ethylene oxide)
PMMA	Polymethylmethacrylate
PVDF	Polyvinylidene difluoride
PVP	poly(vinyl pyrrolidone)
RE	Reference electrode
RES	Renewable energy sources
SAED	Selected area electron diffraction
SEM	Scanning electron microscopy
SEI	Solid electrolyte interphase

SEs	Secondary electrons
SHE	Standard hydrogen electrode
SIBs	Sodium-ion batteries
SPE	Solid polymer electrolyte
STEM	Scanning transmission electron microscope
TREGDME	Triethylene glycol dimethyl ether
TEM	Transmission electron microscopy
TGA	Thermogravimetric analysis
XRD	X-ray diffraction
WE	Working electrode

Table of contents

Abstract	I
List of abbreviations	V
Table of contents	VIII
Chapter 1 Introduction	1
Chapter 2 Fundamentals	3
2.1 Overview of battery	3
2.2 Historic outlook of battery	4
2.2.1 Lithium-ion battery applications	5
2.2.2 Lithium-ion battery manufacturing	6
2.3 Battery basics.....	6
2.3.1 Component costs and working principle of lithium-ion battery	7
2.3.2 Battery specification	8
2.3.3 Important performance parameters of lithium-ion battery	9
2.3.4 Strengths and weaknesses of lithium-ion battery	10
2.4 Cathode materials	12
2.4.1 Layered materials	13
2.4.2 Spinel-type materials.....	14
2.4.3 Olivine-type materials.....	15
2.5 Anode materials.....	15
2.5.1 Intercalation materials.....	17
2.5.2 Alloying-type materials.....	17
2.5.3 Conversion-type materials	18

2.5.4 Lithium metal	19
2.6 Electrolytes	20
2.6.1 Nonaqueous electrolytes	20
2.6.2 Aqueous electrolytes	21
2.6.3 Ionic liquids	21
2.6.4 Polymer electrolytes.....	21
2.6.5 Inorganic solid electrolytes	22
2.6.6 Glyme electrolytes	22
2.6.7 Additives	23
2.7 Lithium metal battery	23
2.8 Aim of the thesis.....	24
Chapter 3 Experimental techniques	29
3.1 Experimental chemical reagents	29
3.2 X-ray diffraction (XRD).....	30
3.3 Thermogravimetric analysis (TGA)	32
3.4 Scanning electron microscopy (SEM)	32
3.5 Energy disperse X-ray spectroscopy (EDS)	33
3.6 Transmission electron microscopy (TEM)	34
Chapter 4 Characterization techniques	50
4.1 Electrode preparation.....	50
4.2 Coin cell assembly	51
4.3 T-type cell.....	51
4.4 Chronoamperometry	52
4.5 Electrochemical impedance spectroscopy (EIS).....	53
4.6 Cyclic voltammetry (CV)	56
4.7 Linear sweep voltammetry (LSV)	57

4.8 Galvanostatic measurements	57
Chapter 5 Glyme-based electrolytes for lithium metal batteries using insertion electrodes...	50
5.1 Introduction	50
5.2 Results and discussion	51
5.3 Conclusion	61
5.4 Experimental section	62
5.4.1 Electrolyte preparation.....	63
5.4.2 Electrode preparation	63
5.4.3 Electrochemical measurements for electrolyte	63
5.4.4 Galvanostatic cycling tests.....	65
Chapter 6 Towards a high-performance lithium-metal battery with glyme solution.....	65
6.1 Introduction	65
6.2 Results and discussion	65
6.3 Conclusion	78
6.4 Experimental section	79
6.4.1 Electrode preparation.....	80
6.4.2 Electrolyte characterization.....	80
6.4.3 Tests in lithium-metal cell.....	82
6.4.4 <i>Ex Situ</i> analysis of the cycled LFP electrodes.....	83
Chapter 7 Electrochemical behavior of nanostructured NiO@C anode in a lithium-ion battery	84
7.1 Introduction	84
7.2 Results and discussion	85
7.3 Conclusion	99
7.4 Experimental section	100
7.4.1 NiO@C samples	100

7.4.2 Material characterization.....	101
7.4.3 Electrode preparation.....	102
7.4.4 Electrode measurements.....	103
7.4.5 Full cell measurements.....	103
Chapter 8 Conclusions.....	105
Chapter 9 Outlook.....	107
References.....	109
Publications and conferences.....	121
Publications.....	121
Conferences.....	122
Acknowledgments.....	124
Resume.....	126

Chapter 1 Introduction

Environmental sustainability and energy security are the two priority issues in the 21st century for safeguarding national security and development as well as regional peace and steadiness [1]. With the ever-increasing global population, the world energy demands will double by 2050 to 28 terawatts (TW), as revealed in **Figure 1.1** [2].

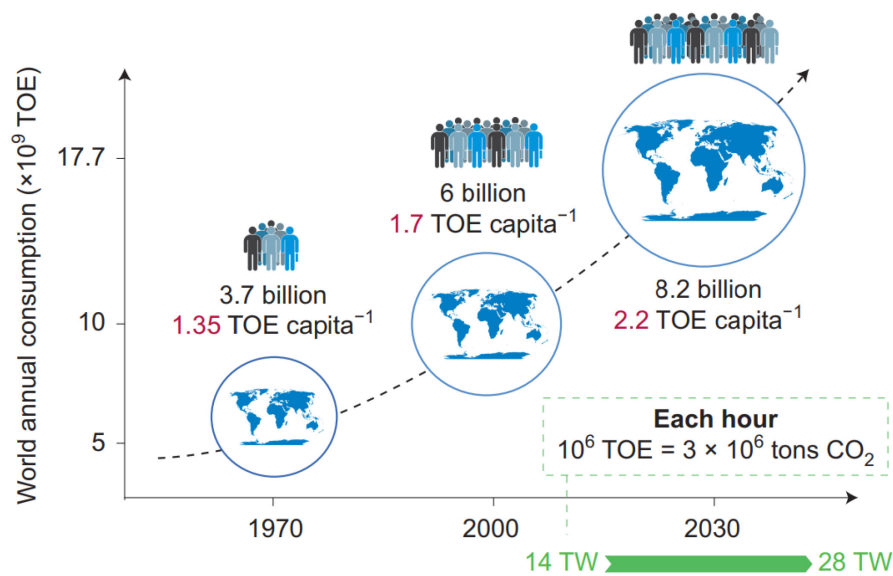


Figure 1.1 Forecasts through 2050 about global energy need. Reprinted from Ref. [2].

As fossil fuels are on the edge of being exhausted, the renewable energy sources (RES) have drawn much attention due to intriguing characteristics in terms of huge development potential, green and pollution-free, recyclable use, and low exploiting costs [3]. As the representatives of thriving RES, the production of solar and wind energy is highly dependent on the natural resources [4]. Nevertheless, the fickle nature of the weather may produce power fluctuations and cause difficulties to capture, store, and transport these renewable energies. Taking the well-known energy source solar energy as an example, incorporation of solar energy into the electrical grid would be not only a good solution, but also a challenging issue due to its intermittent and stochastic character [5]. Thus, the development of electrical energy storage technologies, for example, rechargeable batteries (or called secondary batteries) become crucial.

Among the various options, lithium-ion batteries (LIBs) are currently in the forefront and have been utilized in our daily lives, from portable electronic devices, cordless power tool systems to grid-scale storage. Because of their unique benefits in terms of suitable energy density, reliability, long lifespan, high coulombic and energy efficiency, LIBs are expected to implement large-scale applications ranging up to tens of MWh [6,7]. On the other hand, the emergence of enhanced capabilities (e.g., video players, music players, mobile navigation, web browsing) and available processing power (e.g., mobile cloud sensing, big data, 5G networks) has contributed to the development of advanced electrolytes and alternative electrode materials.

Driven by the above-mentioned widespread diffusion, academia and industries have been attempting to achieve substantial enhancements in battery performance [8]. In this thesis, we thoroughly investigated the electrochemical characteristics of glyme-based electrolytes without and with a LiNO_3 additive for lithium cells and studied the electrochemical properties of new electrode materials, e.g., transition metal oxide anode (NiO) and transition metal oxide cathode, layered $\text{LiNi}_{1/3}\text{Co}_{1/3}\text{Mn}_{1/3}\text{O}_2$ (NCM), aiming at expanding new strategies for the next-generation high-energy and safe lithium batteries.

Chapter 2 Fundamentals

2.1 Overview of battery

The benefits of LIBs in terms of high energy and power density, nonexistent memory effect, high efficiency, and low-cost, have made them become the most efficient and successful rechargeable battery within the last three decades as well as stand out in the 2019 Nobel Prize in Chemistry [9]. The comparison chart displayed the specific power and energy density in different types of rechargeable batteries, as shown in **Figure 2.1**. Compared to other rechargeable battery systems, it is possible to see that LIBs exhibit higher specific power of about 300 W kg^{-1} and energy density approaching 160 Wh kg^{-1} and the energy densities of some batteries are almost double of Nickel-metal hydride (NiMH) batteries. Furthermore, lithium battery technologies (Li metal-polymer, Li ion $\text{LiFePO}_4\text{-C}$, and Li ion $\text{Li(TM)O}_2\text{-C}$) dominate the field of energy storage (see **Figure 2.1**).

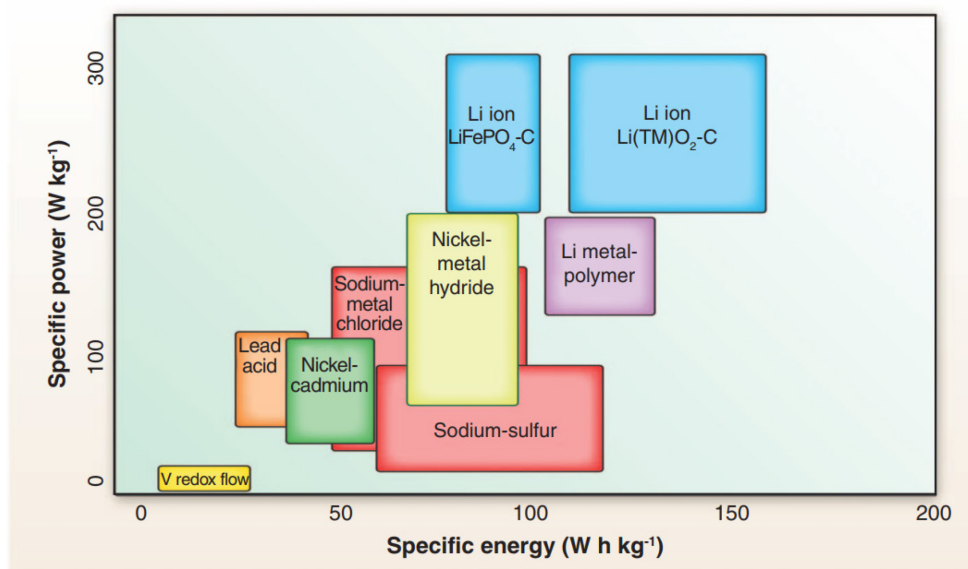


Figure 2.1 Comparison of specific power and energy density in difference batteries. Reprinted from Ref. [10].

In this content, LIBs have been widely utilized as power supplies for hybrid electrical vehicles (HEVs) and hybrid plug-in electrical vehicles (HPEVs), and thereby strong demand for efficient rechargeable

batteries has been ignited [11]. The worldwide sales of LIBs are expected to approach \$213.5 billion by 2020, with a 63% ratio in all storage systems [12]. Nowadays, its practical energy density can ensure 250 Wh kg^{-1} , but it still could not meet the high requirements of $500 - 700 \text{ Wh kg}^{-1}$ [12].

2.2 Historic outlook of battery

It should be noted that the development of batteries is very daunting and challenging. In 1799, the first electric battery, namely, Voltaic pile, was presented by an Italian physicist Alessandro Volta, when he was able to reveal that by preparing some pairs of alternating copper and zinc discs, separated by a cloth saturated in a sodium chloride solution one can generate current by connecting wires [13]. Shortly after, other storage systems have experienced vigorous development, such as the Daniell Cell in 1836, the lead-acid battery in 1859, the Leclanché cell in 1866, the commercially dry cell (zinc-carbon battery) in 1881, the nickel-cadmium (NiCd) battery in 1899, and the nickel-metal hydride (NiMH) battery in 1967 [14–16].

The early stage in 1958, a student at the University of California, William Sidney Harris, investigated the solubility of lithium in some nonaqueous (aprotic) electrolytes, which marked the beginning of studies on the primary lithium-ion batteries [17]. In the 1970s, a French scientist, Michel Armand, first proposed using two different intercalation electrodes to build a lithium-ion battery, “rocking chair” or “shuttle” battery [18]. A researcher at the Exxon Laboratories, Michael Stanley Whittingham, proposed the first rechargeable lithium-ion battery in 1976 and patented in 1977 using a lithium-aluminum (Li/Al) alloy as the negative electrode and a dichalcogenides titanium sulfide (TiS_2) as the positive electrode, Li/ TiS_2 batteries [19]. Though TiS_2 has good intercalation characteristics as cathode material in rechargeable batteries, metallic lithium is prone to react with moisture in atmospheric conditions, which quickly leads to significant safety issues [20]. Following that, in 1980, a Moroccan scientist, Rachid Yazami, pioneered the graphite (C) anode [18]. An American chemist, John Bannister Goodenough, discovered the lithium cobalt oxide (LiCoO_2) cathode ($3.9 \text{ V vs. Li}^+/\text{Li}$) in the same year [21]. A Japanese chemist, Akira Yoshino, a research fellow at Asahi Kasei Corporation, created the prototype of LIBs by replacing the lithium-metal

anode with petroleum coke in 1985 [22]. Inspired by this, five years later, this lithium-ion battery by pairing graphite anode with LiCoO_2 cathode became a thriving commercial reality through Sony corporation [23]. Since then, LIBs have progressively revolutionized electrochemical energy storage and have occupied a significant market share.

2.2.1 Lithium-ion battery applications

LIBs are ubiquitously applied in modern society from tablets, laptops, robots, medical electronics, emergency backup battery, rail traffic, industrial equipment, exploring to surveying [24,25]. Among them, LIBs play a significant role in mainstream automotive applications. Some of the most recent examples include Tesla model S60 (2013), Chevrolet Spark (2014), Volkswagen e-Golf (2015), BYD e6 (2015), and Nissan Leaf (2017) [26].

Several typical application fields are described in detail in **Figure 2.2** [27]. It is clear that the applications of LIBs are rapidly expanding from consumer electronics and devices (e.g., personal cares, smartphones) to transportation (e.g., cars, auto bicycles) and grid energy and industry (e.g., portable energy storage, stationary energy storage). In addition, the rapid growth of new energy automobile and smart grid will further promote the development of LIBs with higher power and specific energy, and higher safety content [28].

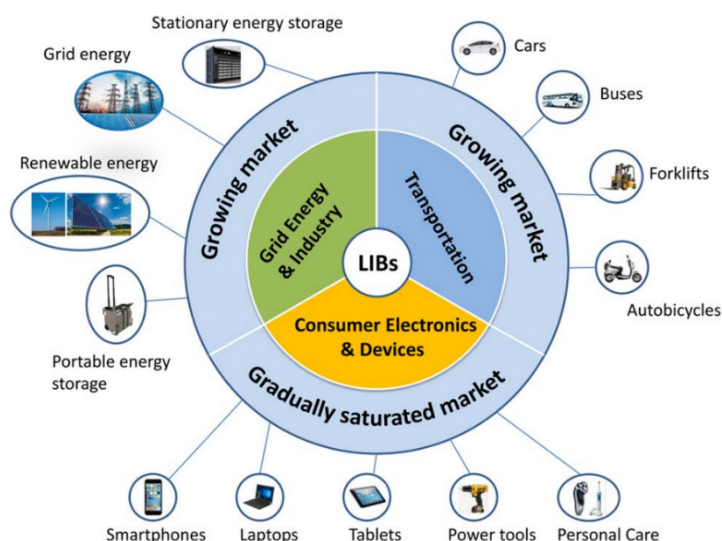


Figure 2.2 Various applications of LIBs from consumer electronics and devices, transportation, to grid energy and industry. Reprinted from Ref. [27].

2.2.2 Lithium-ion battery manufacturing

Over the past decade, lithium-ion battery manufacturing is concentrated in four countries, China, the United States, Japan, and South Korea [29]. According to an analysis by BloombergNEF (BNEF), the global lithium cell manufacturing capacity was approaching 316 gigawatt-hours (GWh) in early 2019 [30]. The leading ten battery companies on the 2019 ranking in the world by shipments have five Chinese companies, Contemporary Amperex Technology (CATL), Build Your Dreams (BYD), Automotive Energy Supply Corporation (AESC acquired by Envision), Guoxuan High-tech (Gotion), and Tianjin Lishen Battery. In the United States, Panasonic Energy of North America and LG Chem Michigan Inc. hold the largest market share in the lithium battery manufacturing industry. Japan has world-class battery manufacturers, such as Nippon Electric Company (NEC), Sony, Toshiba, Sanyo, Hitachi, Ltd., and Goldman Sachs Group (GS). As one of the four dragons in Asia, South Korea is at the forefront in battery production. LG Chem, Samsung SDI, and SK innovation are the typical representatives [29].

2.3 Battery basics

Cathode: The positive electrode associated with the reduction reaction which accepts electrons from the external circuit during discharge. The conductive current collector for the cathode consists of aluminum.

Anode: The negative electrode associated with the oxidation reaction which gives off electrons to the external circuit during charge. The conductive current collector for the anode consists of copper.

Separator: It usually refers to a permeable membrane placed between the cathode and anode. It sets a barrier on both sides but allows exchange Li^+ between each other. A separator usually adopts a polymeric membrane based on microporous monolayer or trilayer polyolefins, such as single-layer or multi-layer polyethylene (PE) and polypropylene (PP) film. Examples of separators used in LIBs include Whatman® glass microfiber filters, Grade GF/A, GF/D, microporous monolayer PP membrane, and Celgard 2400.

Electrolyte: It generally refers to a lithium salt dissolved in soluble ionic compound or an organic solvent whose primary function is the carrier of ion transmission and electron conduction between the cathode and anode.

2.3.1 Component costs and working principle of lithium-ion battery

Figure 2.3a shows an illustration of a common battery and its component costs. It should be noticed that cathode materials mostly limit the energy density, and determine the cell chemistry as well as the overall 30 – 40% battery costs [9]. **Figure 2.3b** displays the components and configuration of a typical lithium-ion battery, including LiCoO_2 cathode, graphite anode, and separator immersed in electrolyte. It reveals the movement of lithium ions (Li^+) from one side to the other, while the electrons move in the opposite direction at the same cycle. Upon the charging process, Li^+ ions depart from LiCoO_2 and are insert into graphite through electrolyte and separator, which corresponds to the oxidation reaction of LiCoO_2 , meanwhile, the graphite is reduced. During discharging, the process is reversed.

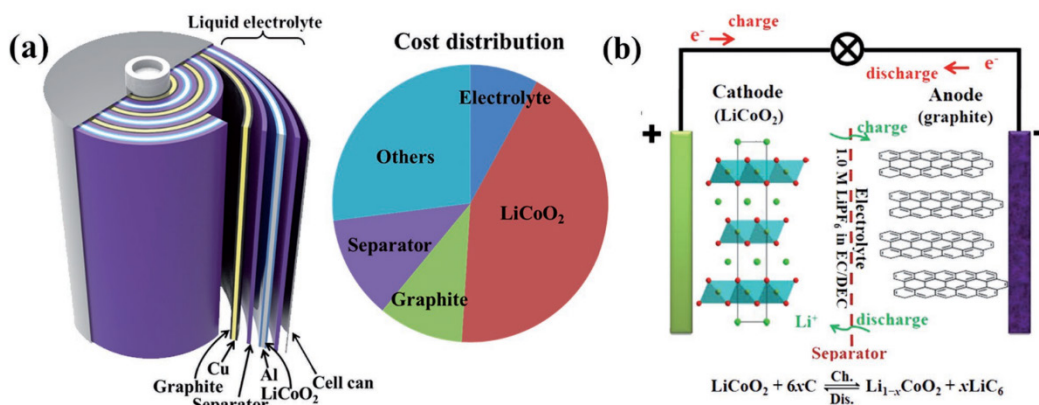
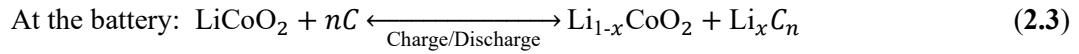
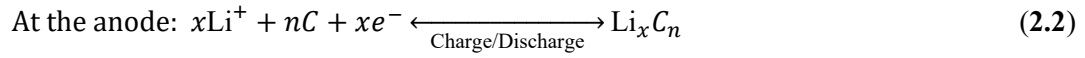
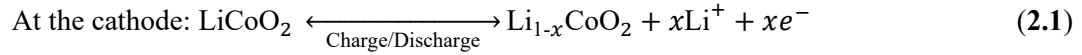


Figure 2.3 (a) Illustration of a common battery and its component costs. (b) Schematic diagram of a LiCoO_2/C lithium-ion battery. Modified from Ref. [31].

The **Equations 2.1, 2.2, and 2.3** show the electrochemical reaction of a LiCoO_2/C cell, which occurs at a potential of about 3.9 V vs. Li^+/Li . A complete electrochemical reaction of a LiCoO_2/C cell during charge and discharge processes is displayed in **Equation (2.3)**. In that procedure, the overall equation can be broken down into two half-reactions, at the cathode **Equation (2.1)** during charging and at the anode **Equation (2.2)** during discharging. Meanwhile, the two Faradaic half-cell reactions occur at electrode/electrolyte interfaces.



2.3.2 Battery specification

Numerous studies have demonstrated that cell design plays a pivotal part in determining the property and safety of lithium-ion battery modules or packs [32]. By shape and component, these cells can be typically categorized into following four types, cylindrical cells, prismatic cells, button (or coin) cells, and pouch cells, as can be seen in **Figure 2.4**.

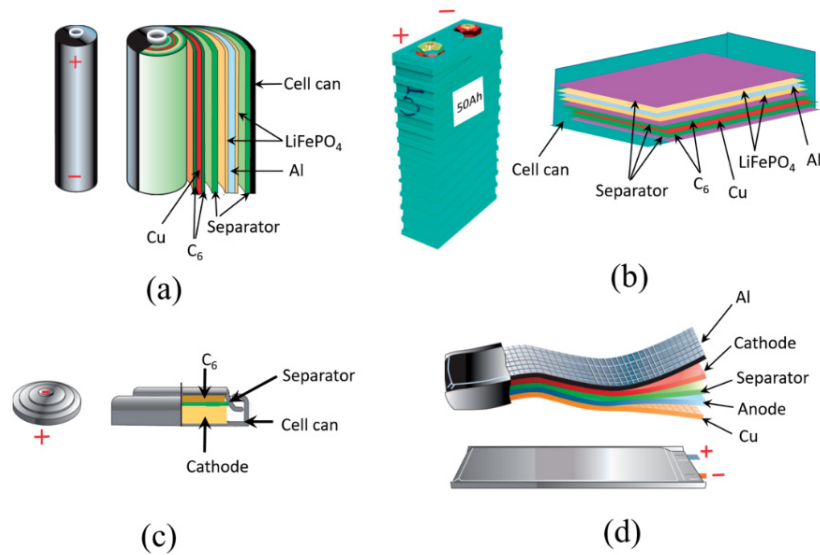


Figure 2.4 Images showing the four different shapes and components used in LIBs: **(a)** Schematic of a cylindrical cell, **(b)** Schematic of a prismatic cell, **(c)** Schematic of a button cell, and **(d)** Schematic of a pouch cell. Modified from Ref. [23].

The cylindrical cell is characterized by good mechanical stability, cheapness, and advanced safety features, which is often used in portable electronic devices, including medical instruments, flashlights, digital cameras, and walkie-talkies [33]. It can offer a long cycle and calendar life but has less than ideal packaging density [34]. The prismatic cell has a large capacity, and its prismatic shape (Jelly-rolled or stacked) is easily to connect more cells [33]. It is usually encased in aluminum or steel. A

prismatic cell is space-saving, but its manufacturing cost may be more expensive than the cylindrical cell. Furthermore, cylindrical cells and prismatic cells are the most popular and well-known batteries.

Button cells have an advantage of low manufacturing costs due to the small size but have no safety vent that they can only be charged for 10 to 16 hours [35]. Most button cells are non-rechargeable on the market, for example, hearing aids. A button cell can easily swell if it is charged too fast. The pouch cell is light, flat, and cost-effective, and usually adopts a laminated structure in a bag, offering a great possibility for stacking, which has been successfully applied to electric vehicles (EVs). At the same time, it is sensitive to humidity and high temperature [23].

2.3.3 Important performance parameters of lithium-ion battery

Capacity: The amount of charge a battery can store, which depends on the amount and redox characteristics of the active material in a battery. It is typically expressed as mAh or Ah. The specific capacity of the active material refers to the capacity per unit weight (C , mAh g^{-1} , or Ah kg^{-1}). The theoretical specific capacity (C) can be described as **Equation 2.4**.

$$C = \frac{nF}{3.6M} \quad (2.4)$$

where n : the number of charge carriers,

F : Faraday constant (approximately 96485 C mol^{-1}),

M : the molecular weight of any given active material.

Energy density: It can be described as the energy output capability of a battery. There are two expression forms.

Volumetric energy density: How much energy is available from a battery in a certain volume for a given material. It is most expressed as Watt-hours/liter (Wh L^{-1}).

Gravimetric energy density (specific energy): How much energy is available from a battery in a certain weight for a given material. It is given as Watt-hours/kilogram (Wh kg^{-1}).

Specific power: The energy in a battery that can release per unit weight or unit volume of active material in unit time. It is often expressed as $W\text{ kg}^{-1}$ or $W\text{ L}^{-1}$.

C-rate: It is a measure of the rate to reveal the maximum charge or discharge current that a battery can afford, which is numerically equal to the Ah (Ampere-hour) rating of a battery. For example, a 1C rate refers to allowing the cell to release a maximum charge/discharge capacity in 1 hour.

Coulombic efficiency (faradaic efficiency or current efficiency): The ratio of output charge from a battery versus the input charge into a battery within one cycle. A coulombic efficiency in a full cycle is usually less than 100 %, mainly because of the loss of charge in irreversible reactions.

Cell voltage: The potential difference (ΔE) between the cathode and anode. ΔE equals the cell potential. It can be given by **Equation 2.5**.

$$\Delta E = E_{\text{cathode}} - E_{\text{anode}} \quad (2.5)$$

Open circuit voltage: The electric potential difference of a cell which is disconnected from the circuit.

Operating voltage: The electric potential difference of a cell which is connected to the circuit, while the current flows in it.

2.3.4 Strengths and weaknesses of lithium-ion battery

The advantages of LIBs are listed below:

- High energy density: Some lithium-ion cells can reach the energy densities of about 250 Wh kg^{-1} and 650 Wh L^{-1} , respectively.
- High open circuit voltage: The nominal cell voltage of a lithium-ion cell is about 3.6 V, which is nearly two times that of NiCd and NiMH batteries.
- Long cycle life: Lithium-ion cells can provide hundreds or thousands of charge/discharge cycles. Many advanced lithium-ion cells still have adequate capacity after 2000 cycles.

-
- Low self-discharge: After being charged, their rates of self-discharge are typically around 5.0% in the first 4 hours but then fall to around 1.5 ~ 3.0% per month, which are much lower than the self-discharge rates of NiCd batteries (about 10%) and NiMH batteries (about 20%).
 - No memory effect: Zero to minimal memory effect in LIBs. but other rechargeable batteries, such as nickel-based batteries have strong memory effect.
 - Long storage time: Some lithium-ion cells even have a shelf life of more than 10 years.
 - Quick charging: For example, charging by 1C for 30 minutes, some batteries can reach 80% of the rated capacity.
 - Green and environmentally friendly.

The energy density will be able to reach tens of MWh by developing a variety of emerging advanced electrolytes, anode materials, and cathode materials [31]. Although LIBs are more popular than many other types of batteries, their drawbacks could not be ignored.

- ✧ High production costs: The early LiCoO_2 cathode materials, have made the total costs of LIBs too high, which is around 40 percent higher than NiMH batteries. The development of LiMn_2O_4 , LiFePO_4 , and ternary materials have gradually replaced LiCoO_2 , but their costs still have room for further reduction.
- ✧ Intolerant to over-charge/over-discharge: It can shorten the battery lifespan and cause possibly hidden trouble, for instance, fire danger and explosion.
- ✧ Sensitivity to high temperature: The electrochemical impedance of LIBs is particularly sensitive to the operating temperature. Overheating may ignite the electrolyte and cause the cells or batteries to degrade faster.
- ✧ The aging effects: Once LIBs leave the factory; they will naturally degrade. Special protective equipment is therefore required. For instance, a lithium-ion cell is charged with 40 ~ 50% capacity and stored in a cool place, which will reduce the aging effects.

2.4 Cathode materials

Among the main components, cathode has a significant influence on the volumetric energy/power densities of a lithium-ion cell, which can largely determine the battery performance and cost [36–38]. A comparison of electrochemical performance (achievable capacity and voltage) of the most popular cathode materials are shown in **Figure 2.5a**. In current LIB technologies, a large number of research has focused on these materials and their derivatives [39,40]. **Figure 2.5b** displays three typical crystal structures in these materials [41]. They are Li-insertion compounds, layered LiCoO_2 , spinel LiMn_2O_4 , and olivine LiFePO_4 .

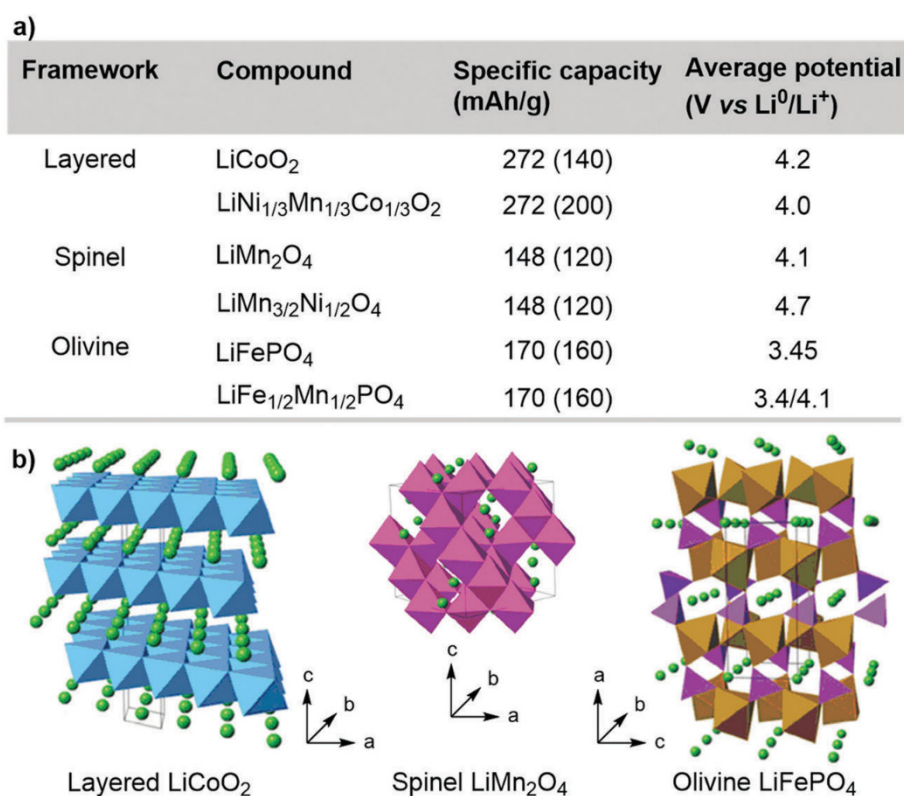


Figure 2.5 (a) Electrochemical features of commercially available three classes of cathode materials, and (b) their corresponding crystal structures. Reprinted from Ref. [41].

In addition, to further enhance the energy density, the introduction of other transition metals into the cathode compounds has been explored. Among the various alternative cathode materials proposed so far [42], lithium nickel cobalt aluminum oxide (NCA, $\sim 200 \text{ mAh g}^{-1}$, $\sim 3.8 \text{ V vs. Li}^+/\text{Li}$) with high energy density has been extensively used in Tesla cars. Yet, with the price of cobalt increased by 2.56 times only in one and a half years (US\$ 26,500 per ton in September 2016, vs. US\$ 94,250 per

ton in March 2018) [43], the traditional lithium-ion battery technology urgently needs to be upgraded to improve the energy density and the safety content, particular the use of expensive and hazardous cobalt in commercial cells [44]. Currently, many efforts are being undertaken to exploit the cobalt-free, less toxicity, and high-abundance cathode materials [45].

2.4.1 Layered materials

Lithium cobalt oxide (LCO) possesses the layered α -NaFeO₂ structure, whose space group is $Fd\bar{3}m$ [46]. As the extensively used cathode materials [47], LCO was firstly introduced by Goodenough and his colleagues in 1980 [48], and after a few years, wildly commercialized by Sony. In the Li_{1-x}CoO₂ structure, when the amount of inserted/extracted Li⁺ exceed 0.55 per formula unit, the additional flowing holes will be transferred to the 2p molecular orbital of oxygen to form O²⁻ ions over the surface of the particles, which subsequently oxygen evolves, leading to the formation of oxygen defects [9]. Therefore, up to 0.55 amount of Li⁺ ions can be extracted from the host structure of LCO.

Even though LCO has a theoretical specific capacity of 274 mAh g⁻¹, it contributes to a maximum capacity of 165 mAh g⁻¹ at the working voltage of 4.35 V [44]. High volumetric energy density, relative high Li⁺/electron conductivity, low self-discharge rate, and reliability make LCO maintain its dominant position in the portable applications almost two decades. Driven by the realization that cobalt is a high toxicity, expensive, and scarce resource, academia and industries have been trying to seek for low-cost alternatives [49].

The isostructural lithium nickel oxide (LNO) is a promising alternative material to replace LCO, which has been very actively studied during the 1990s due to its higher specific energy, and cost advantages [50]. However, the gradual structural degradation of LNO during prolonged cycling leads to noticeable capacity fading, preventing the commercial applicability [51]. Further improvements can be made by surface coating and partial doping/substitution with Co or other transition metals [52], before LNO become more competitive and possibly be used in practical devices.

The so-called NCM type materials with the formula Li(Ni_{1-x-y}Co_yMn_x)O₂ is the most prominent representative [53,54]. LiNi_{1/3}Co_{1/3}Mn_{1/3}O₂ was reported for the first time in 2001 by Ohzuku and Makimura [55], although this material can only deliver a specific capacity of 165 mAh g⁻¹ at the first

cycle. NCM can be regarded as a solid solution of LiNiO_2 , LiCoO_2 , and LiMnO_2 as well as integrate the features of these three, which is expected to benefit from Ni, Co, Mn in terms of capacity, rate performance, and structural stability, respectively. NCM exhibits a high reversible capacity of about 200 mAh g^{-1} when being cycled up to high voltage of $4.6 \text{ V vs. Li}^+/\text{Li}$, though it has an ideal theoretical capacity of 278 mAh g^{-1} . In the near future, NCM still remains as an extremely interesting alternative if the full benefits of NCM with high capacity can be released [56].

2.4.2 Spinel-type materials

In 1981, Hunter first reported the complete extraction of Li^+ ions from spinel lithium manganese oxide (LiMn_2O_4 , referred to as LMO) with acidic solutions to form $\lambda\text{-MnO}_2$ [57]. LMO has the cubic spinel structure in which Li and Mn ions occupy the 8a sites (tetrahedral) and 16d sites (octahedral), while the oxygen ions have a cubic close-packed framework occupying the 32e positions [58]. LMO is a cheap, non-toxic, easily accessible material, offers a suitable operating voltage at $4.1 \text{ V vs. Li}^+/\text{Li}$, and demonstrates a reversible capacity of about 120 mAh g^{-1} , which has been regarded as a viable option for large-scale storage [59]. During electrochemical cycling, the loss of oxygen, Jahn-Teller effect, the deposition of Mn^{3+} on the anode, and the leaching of Mn^{2+} ($\text{Mn}^{3+} \rightarrow \text{Mn}^{4+} + \text{Mn}^{2+}$) in the electrolyte easily lead to poor cyclability [45].

As derived from LMO, spinel-structured $\text{LiNi}_{0.5}\text{Mn}_{1.5}\text{O}_4$ (LNMO) has emerged as one of the most prospective materials in view of its theoretical capacity of 147 mAh g^{-1} and working voltage as high as $4.7 \text{ V vs. Li}^+/\text{Li}$, which might lead to an energy density of about 690 Wh kg^{-1} [60], namely, in approaching the values of the NCA [61], and $\text{LiNi}_{0.8}\text{Co}_{0.1}\text{Mn}_{0.1}\text{O}_2$ (NCM811) [62] materials in lithium cells. LNMO may crystallize in either simple cubic (space group $P4332$) or face-centered structures (space group $Fd\bar{3}m$) depending on the ordering of Ni^{2+} and Mn^{4+} ions in octahedral sites of the lattice, as well as on the presence of Mn^{3+} in the spinel framework to compensate oxygen vacancies [63]. Both structures enable three-dimensional (3D) lithium-ion (de)insertion at high current rates, although the latter has a higher bulk electronic conductivity than that of the former [64]. Furthermore, the suitable characteristics of LNMO in terms of good thermal stability, and modest toxicity are expected to lower environmental impact of the cell [65].

Though there has been a flurry of research about LNMO, the ideal cycling performance, including the small irreversible capacity, slow capacity fading, and satisfactory rate capability especially at elevated temperatures ($> 45\text{ }^{\circ}\text{C}$), could not be achieved simultaneously in the last decade [66–69] due to manganese dissolution, which currently hinders its possible applications [70]. In the regards, the optimization of structure and morphology of LNMO may improve the insertion kinetics and stabilize the electrode/electrolyte interphase [71], while a proper tuning of the electrode composition, e.g., by transition metal substitution, may mitigate the electrode degradation, limit the parasitic phenomena affecting the cycle life, and further enhance the electrode charge transfer [72], thereby optimizing the electrochemical behavior in lithium cells.

2.4.3 Olivine-type materials

Olivine-type lithium iron phosphate (LFP) was first proposed by Goodenough in 1997 [73], which has been recognized as a very promising cathode materials that can be used in large vehicles or facilities thanks to its naturally abundant, environmentally benign, good thermal stability, and improved safety [74]. LFP is characterized by a voltage plateau of 3.45 V vs. Li^+/Li based on the $\text{Fe}^{3+}/\text{Fe}^{2+}$ redox couple, which may provide an energy density of around 580 Wh kg^{-1} [75]. It adopts a typical orthorhombic olivine-type structure, whose space group is $Pnma$ [76]. Nevertheless, LFP has suffered from a gradual loss of capacity during long-term cycling, originating from the low bulk electronic conductivity ($< 10^{-9}\text{ S cm}^{-1}$) and weak Li^+ diffusion coefficient ($\approx 10^{-14}\text{ cm}^2\text{ s}^{-1}$), which greatly impede its wide utilization in energy storage appliances [77].

2.5 Anode materials

Recent years have witnessed tremendous expansion of LIBs in portable electronic devices, and various EVs. To meet the expectations for higher energy density, considerable efforts have been devoted to the search for either high-voltage cathode materials or high-capacity anode materials [78]. For the latter, developing anode materials with high capacity, enhanced safety, low electrode potential, and high reversibility are of the utmost importance [79]. The typical anode materials

include but not limit graphitic carbon, hard carbon, lithium titanate oxide (LTO), metallic lithium, silicon (Si), tin (Sn), germanium (Ge), antimony (Sb) and their oxides and alloys, and transition metal oxides (e.g., NiO, Fe₂O₃). Their reaction mechanism basically can be divided into three categories (intercalation, alloying, and conversion), e.g., $6C + Li \leftrightarrow LiC_6$, $Sn + 4.4Li \leftrightarrow Li_{4.4}Sn$, and $Fe_2O_3 + 6Li \leftrightarrow 2Fe + 3Li_2O$. The schematic diagram of three types of reaction mechanisms and their advantages and disadvantages are shown in **Figure 2.6**. For intercalation-type materials, Li⁺ can be reversibly incorporated into the host structures without major damages, which can ensure stable cycling behavior and good capacity retentions but relative low capacities [42]. Alloying- and conversion-type materials offer fast lithium storage capacities and carry on the deep redox reactions, delivering relatively high capacities [80]. However, the weak conductivity, large voltage hysteresis, and the accompanying large volume variation limit their commercial availability [81]. Notably, priority is given to discuss conversion materials in this section.

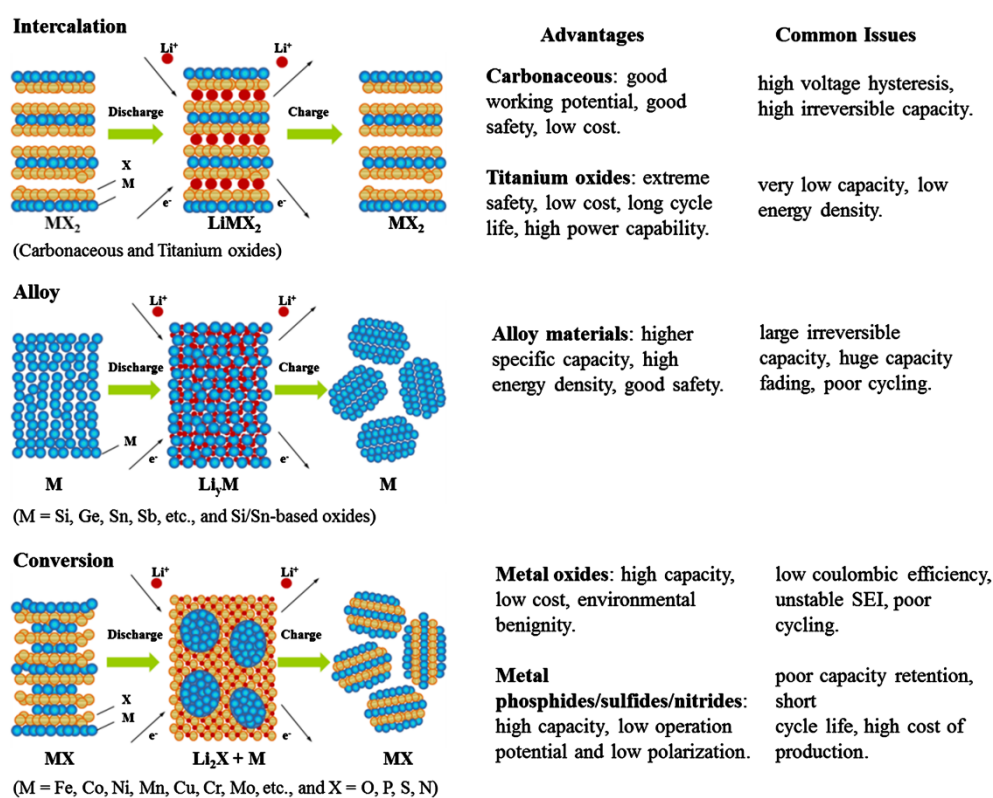


Figure 2.6 Three different types of anode reaction mechanisms in lithium battery and their strengths and weaknesses. Reprinted from Ref. [82].

2.5.1 Intercalation materials

As the earliest intercalation and commercialized anode material, graphite is still extensively used in the commercial cells up to now because of its inexpensive, layered structure, and good stability [83,84]. Graphite has a similar potential to that of a Li^+/Li redox couple and a comparatively low theoretical capacity of 372 mAh g^{-1} . The actual specific capacity of graphite is in a range between 330 and 350 mAh g^{-1} because it allows only one Li^+ involving the intercalation reactions [85]. However, the shortcomings of graphite cannot be ignored, for example, a low diffusion rate of Li^+ [86].

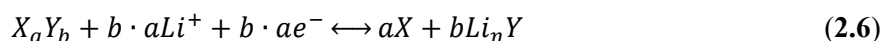
Titanium-based materials sacrifice a certain reversible capacity (theoretical capacity of 175 mAh g^{-1}), but their excellent features of non-toxicity, safe operating voltage, and a small volume expansion, as well as stable chemical properties, have made them stand out in anode materials [87]. The best example is lithium titanate oxide (LTO), which has been widely recognized as a zero-strain insertion material, with a flat discharge/charge potential of around $1.5 \text{ V vs. Li}^+/\text{Li}$ [88].

2.5.2 Alloying-type materials

Alloying-type materials (mainly in the IV and V groups) have higher theoretical capacities than intercalate-type materials and suitable voltage plateaus, which have attracted great concerns [89]. Taking the well-known silicon (Si) as an example, Si is capable of releasing high amounts of lithium at low potential plateaus ($< 0.5 \text{ V vs. Li}^+/\text{Li}$) and offers an high theoretical specific capacity (for the $\text{Li}_{22}\text{Si}_5$ phase at high temperature, 4200 mAh g^{-1}) that is more than eleven times that of graphite [90,91]. Another example is Tin (Sn) that provides the maximum lithium insertion of 4.4. Sn possesses a theoretical specific capacity of 999 mAh g^{-1} [92], that is, about the quarter of Si. Si (Sn) undergoes an alloy reaction to form a Si-Li (Sn-Li) alloy, without lithium dendrites, but Si (Sn) also undergoes a serious volume expansion (almost 300%, $> 300\%$, respectively) upon lithiation and (de)lithiation processes that induces electrode pulverization, fragmentation, and even shedding [93]. A direct consequence is the fast capacity decays in the long-term cycling [94] that ultimately restricts its practical application [95].

2.5.3 Conversion-type materials

The amounts of intercalated and deintercalated Li^+ ions in traditional carbon materials are limited, usually less than one unit [25]. Their low theoretical capacities have become the main bottleneck for applications in LIBs. In this regards, conversion-type materials offer higher theoretical capacities (e.g., 712 mAh g^{-1} for NiO, 1007 mAh g^{-1} for Fe_2O_3), have a safer lithiation potential, and are environmentally friendly, which accordingly are receiving extensive interest [96]. Lithiation and delithiation of Li^+ ions in X_aY_b during the discharge and charge processes, are described in **Equation (2.6)**



Where X is a metallic cation (Fe^{3+} , Bi^{3+} , V^{3+} , Ti^{3+} , Cu^{2+} , Co^{2+} , Ni^{2+} , etc.),

Y refers to the anion (F, O, N, S, P).

X_aY_b is fully electrochemically converted to metallic X , embedded within a Li_nY matrix during discharge. The structure of X_aY_b is reversibly collapsed and reconstructed during electrochemical reactions. This conversion reaction can utilize all the oxidation valence states of the metal cation, which can realize multi-electron transfer [97]. Therefore, the lithium storage capacities in conversion materials are higher than the traditional graphite materials 2 to 4 times [98].

The caveat is that fluoride can react at high voltage, approaching 3.0 V vs. Li^+/Li . An outstanding example is iron fluoride (712 mAh g^{-1} for $3 e^-$ transfer), which has become an promising candidate for cathode materials in high-rate LIBs and sodium ion batteries (SIBs) [99,100].

Transition metal oxides, for instance, NiO [101], CuO [102], Fe_2O_3 [103], and MnO_2 [104] based on the conversion reaction mechanism, are capable of insertion/extraction between one and six Li^+ ions per formula unit, resulting in desirable reversible capacities [105]. However, they typically show higher working voltages than graphite and Li-alloying anodes [106]. The severe electrode reorganization may cause pulverization and loss of electric contact of the active materials, which is reflected as a rapid capacity fade [107]. At the same time, the voltage signature may limit the effective use in full lithium-ion cells due to relatively low energy and gradual electrode unbalancing

during cycling [108]. Furthermore, the huge irreversible capacity of conversion electrodes typically occurring upon the initial cycles requires anode pre-lithiation strategies, which further hinder their commercialization [109].

Numerous strategies have been proposed to optimize the cycling stability of transition metal oxides in lithium cells, as revealed in the following:

- ✧ Morphological tailoring is conducive to optimize the structure, increase the specific surface area, and improve the electrochemical activity [110].
- ✧ Preparation nano-sized materials contribute to shorten the electrons and Li^+ diffusion pathways as well as increase the structural flexibility, such as nanomembranes [111], nanofibers [112], nanobelts [113], and nanosheets [114].
- ✧ Preparation of composite materials by combining different materials, including carbon materials and conducting polymers with high molecular, are beneficial to improve the ionic and electronic conductivity and partially accommodate the volume changes [115].

Therefore, a careful tuning of the morphological features of metal oxide-carbon composites and carbon-coated metal oxide electrodes is a key requirement to effectively enhance the conversion reaction whilst limiting possible parasitic processes [116]. Nanostructures may mitigate the expansion of conversion materials upon electrochemical reduction in lithium cells and increase the active surface [78], while incorporation into carbon matrices of various morphologies may enhance the conductivity and buffer volume variations [117]. Hence, one of the purposes in this work is investigate the electrochemical characteristics of the NiO@C anode in lithium half-cells and full cells.

2.5.4 Lithium metal

The most attractive anode material in all possible candidates would be pure metallic lithium, because it has the highest theoretical capacity of 3800 mAh g^{-1} , and lowest electrochemical potential (-3.04 V vs. the standard hydrogen electrode). Nevertheless, its commercialization in lithium metal batteries has not been implemented because of the safety and efficiency reasons, which arises from the formation of dendritic/mossy lithium and low stripping/plating efficiency upon repeated cycling [118]. Uncontrolled growth of lithium dendrites and large volume changes easily cause cracks, which

exposes plentiful fresh lithium metal out, leading to irreversible loss of both working lithium and electrolyte [119,120]. Ultimately, lithium dendrites connect with electrolyte and separator, which results in battery internal short circuits and even thermal runaway [121].

2.6 Electrolytes

The electrolyte is normally a solution (solvent) containing dissociated salts that can efficiently conduct electricity and ensure the ion movement from one electrode to the other [122]. An ideal electrolyte requires the following characteristics [123]:

- ◆ Excellent chemical and thermal stability under operating temperatures.
- ◆ Higher ionic conductivity and negligible electronic conductivity.
- ◆ Broad electrochemical window.
- ◆ Environmentally friendly and low toxicity.
- ◆ Low cost and easily available.
- ◆ Inert towards cell components.

In general, five classes electrolytes can be discriminated: nonaqueous electrolytes, aqueous electrolytes, ionic liquids, polymer electrolytes, and inorganic solid electrolytes.

2.6.1 Nonaqueous electrolytes

The commercial electrolytes used in LIBs are nonaqueous solutions, which refer to lithium salts dissolved in organic solvents or blends of solvents. Lithium perchlorate (LiClO_4), lithium hexafluoroarsenate (LiAsF_6), lithium triflate (LiCF_3SO_3), and lithium tetrafluoroborate (LiBF_4) are the mainly employed lithium salts. The well-known examples include 1 M lithium hexafluorophosphate (LiPF_6) dissolved in a mixture of cyclic and linear carbonates. The former includes ethylene carbonate (EC) and propylene carbonate (PC), while the latter contains dimethyl carbonate (DMC), diethyl carbonate (DEC), and ethyl methyl carbonate (EMC). However, regarding

their high vapor pressure, poor viscosity, flammable features, especially the solvents, this formulation still has some drawbacks, for example, when combined with a high voltage cathode it exhibits the poor chemical and thermal stability at elevated temperatures [124].

2.6.2 Aqueous electrolytes

An aqueous solution is the one that water is the solvent. Using water as the solvent has several distinct advantages like high ionic conductivity, inexpensive, environmentally friendly nature, operating stability, and non-flammable [125]. In this regard, many salt solutions, such as KOH, LiCl, Na₂SO₄, LiNO₃, Li₂SO₄, Na₂SO₄, and K₂SO₄ have been reported [125,126].

2.6.3 Ionic liquids

Ionic liquids (ILs) are generally considered as being green solvents that possess high thermal stability and almost null vapor pressure [127]. ILs usually consist of large asymmetric organic cations and inorganic or organic anions, whose chemical and physical properties can be fine-tuned [128]. The commonly-used cations are ammonium, phosphonium, imidazolium, pyrrolidinium, while the typically used anions are tetrafluoroborate (BF₄)⁻, hexafluorophosphate (PF₆)⁻, triflate (OTf)⁻, bistriflimide (NTf₂)⁻, and acetate(OAc)⁻. Two crucial merits (non-volatility and non-flammability) have made ILs become one of the most promising candidates to replace conventional electrolytes based on either aqueous or organic solvents. However, the relatively high viscosity, sluggish transport properties, and high costs still limit their wide electrochemical applications [129].

2.6.4 Polymer electrolytes

Polymer electrolytes (PEs) are macromolecular compounds that offer improved mechanical properties, flexibility, and safety [130]. They can be divided into three different classes: solid, gel, and composite [130]. Poly(ethylene oxide) (PEO), poly(acrylonitrile) (PAN), poly(methyl methacrylate) (PMMA), poly(vinylidene fluoride) (PVdF), poly(vinyl pyrrolidone) (PVP), and their derivatives have been suggested to use as the host polymers in PEs [131,132].

Solid polymer electrolytes (SPEs) have exhibited a wide thermal stability, stretchable, flexible, and low volatility [133]. Gel polymer electrolytes (GPEs) combine the merits of high ionic conductivity of the liquid electrolytes and good mechanical properties of the SPEs, which have aroused great interest [134]. At the same time, the development of composite polymer electrolytes (CPEs) based on the attempts to overcome the limitations of SPEs, are of great importance. The strategies for preparation and designing of CPEs have been intensively investigated, including polymer blending, incorporation of plasticizers, adding ceramic fillers, and so forth [132,135,136].

2.6.5 Inorganic solid electrolytes

Inorganic solid electrolytes (ISEs) are an ideal choice for battery researchers due to their particular advantages in terms of non-flammable and high ionic conductivity ($10^{-2} \sim 10^{-4} \text{ S cm}^{-1}$) [137]. ISEs can be classified into two categories: oxide solid electrolytes and sulfide solid electrolytes. A series of oxide solid electrolytes including perovskite, garnet, lithium ion super ionic conductor (LISICON), sodium ion super ionic conductor (NASICON), $\gamma\text{-Li}_3\text{PO}_4$, and LiPON-related materials, have been extensively explored in recent years [138]. Sulfide solid electrolytes mainly consist of Li_2S and sulfides, such as $\text{Li}_2\text{S-SiS}_2$, $\text{Li}_2\text{S-P}_2\text{S}_5$, and $\text{Li}_2\text{S-GeS}_2$ systems. Furthermore, they have much higher ionic conductivities than oxide solid electrolytes [139,140].

2.6.6 Glyme electrolytes

Poly(ethylene glycol) dimethyl ethers with small n numbers in $\text{R}_1\text{O}(\text{CH}_2\text{CH}_2)_n\text{R}_2$, also called end-capped glymes, are liquid oligomers suitable as aprotic solvents for lithium battery electrolytes [141]. They have been investigated as possible solvents for various lithium salts, such as those employing the bis(fluorosulfonyl)imide (FSI^-) [142], bis(trifluoromethanesulfonyl)imide (TFSI^-) [143], bis(pentafluoroethanesulfonyl)imide (BESI^-) [144], and trifluoromethanesulfonate anions (CF_3SO_3^-) [145].

Indeed, glyme-based electrolytes have demonstrated suitable Li^+ transport and adequate electrochemical stability window (ESW) for battery application, higher flash point than carbonate-based and 1,3-dioxolane/1,2-dimethoxyethane-based solutions [146], as well as tunable chemical and

physical properties by changing the chain length [147,148], which are receiving plenty of attention in view of their compatibility with the high-energy C/O₂ and sulfur cathodes [145].

2.6.7 Additives

To ensure a stable lithium/electrolyte interphase at both the positive and negative side, the electrolyte properties may be possibly improved by the introduction of small quantities of electrolyte additives (0 to 10 wt.%) [149]. The use of suitable additives remarkably enhanced the electrode passivation behavior [150], leading to promising cell performances.

Literature works have shown that vinylene carbonate (VC) [151], fluoroethylene carbonate (FEC) [152], and lithium nitrate (LiNO₃) [153] may improve the SEI between electrode and electrolyte. In particular, it is widely demonstrated that LiNO₃-containing electrolytes may form a uniform and stable anode passivation layer containing both organic (e.g., ROLi and ROCO₂Li) and inorganic (e.g., Li_xNO_y, Li₃N, and Li₂O) species, which can mitigate the parasitic reactions in the cell and limit the lithium dendrite growth [154,155]. Moreover, LiNO₃ has been extensively studied in Li–S cells as a lithium protective agent able to prevent the chemical reduction at the anode side of the long-chain polysulfides (Li₂S_x, 4 ≤ x ≤ 8) [156]. Many works suggested the beneficial effects of LiNO₃ in cells using electrolyte solutions of triethylene, tetraethylene, and polyethylene glycol dimethyl ethers with LiCF₃SO₃ and olivine cathodes [157]. Thus, one of the main purposes in this thesis is focus on the electrochemical properties of glyme solutions without LiNO₃ and with a LiNO₃ additive in lithium metal batteries.

2.7 Lithium metal battery

Lithium metal anode first appeared in the 1970s, and its research in secondary batteries has been continuous but slow in the past four decades, not to mention commercialization [158]. Though the lithium-metal electrode has a theoretical specific capacity as high as 3860 mAh g⁻¹ (vs. 372 mAh g⁻¹ for graphite), the lowest electrochemical potential (3.040 V vs. SHE compared to 2.84 V vs. SHE for graphite), and a density of 0.59 g cm⁻³ (vs. 2.25 g cm⁻³ for graphite) [159].

Analogously to graphite, meanwhile, with different features and magnitude, the lithium metal anode is thermodynamically unstable in most electrolyte solutions. The growth of lithium dendrites on the lithium surface become uncontrollable during cycling due to the non-uniform current/ion distributions [119], accompanied by the mossy lithium, leading to the formation of a fragile solid electrolyte interphase (SEI) layer. Moreover, the unstable SEI layer and the formation of dead lithium during electrodeposition can further aggravate dendrite growth, leading to rapid capacity fade and low coulombic efficiency (CE) [160]. In severe cases, the separator is penetrated as the dendrites connect the cathode and anode, causing battery internal short-circuit even explosion. An adequate SEI layer is thereby required to kinetically prevent parasitic reactions, which affect anode, electrolyte, and cycling performance [120], and possibly limit hazardous dendritic growth [161]. Therefore, an improved lithium/electrolyte interphase is crucial for ensuring, at the same time, fast charge transfer and electrochemical stability upon long-term cycling [119].

A renewed interest has been recently devoted to the high energy lithium metal anode as LIBs are approaching the lithium storage limit [162]. Secondary lithium metal batteries might ensure higher gravimetric and volumetric energy density than lithium-ion ones by properly addressing the metal electrodeposition and safety issues [120]. Moreover, the high reactivity of lithium metal requires *ad hoc* formulations with lower flammability than conventional electrolytes [163].

2.8 Aim of the thesis

The primary goal of this thesis is to identify and develop novel electrolytes for lithium metal batteries and advanced anode materials for LIBs.

The end-capped glymes based on the formula $R_1O(CH_2CH_2)_nR_2$ are receiving increasing interest owing to their non-flammability, suitable Li^+ transport ability, and wide electrochemical window. As for the anode materials, nickel oxide (NiO) may be electrochemically reduced to metallic Ni and Li_2O , delivering a high theoretical capacity of 718 mAh g^{-1} .

The electrolytes and electrode materials are summarized in **Chapter 2**. The electrochemical properties of the glyme electrolytes and NiO materials are investigated by various experimental methods and electrochemical techniques, as described in **Chapters 3** and **4**.

A comparative electrochemical study is carried out on six solutions in order to clarify the effect of the electrolyte formulation on the ionic conductivity, the lithium transference number, the electrochemical stability window, as well as the lithium/electrolyte interphase characteristics under static and dynamic conditions. Furthermore, **Chapter 5** also investigates the electrochemical properties of glyme-based solutions of various lithium salts as electrolytes for Li/LFP cells.

Chapter 6 studies the effect of a LiNO₃ addition to the above-mentioned electrolyte solutions. The cathode/electrolyte interphase behavior during galvanostatic charge/discharge over 200 cycles is further investigated. Meanwhile, this chapter tests the most optimized formulation over 500 charge/discharge cycles and measures the cell resistance and the coulombic efficiency to propose the use of LiNO₃-containing, glyme-based electrolytes as an effective strategy enabling rechargeable lithium-metal batteries.

Investigation of the conversion electrodes in full lithium-ion cells appears particularly important considering the issues in terms of electrode stability upon cycling, working voltage, and coulombic efficiency. A NiO anode in a lithium-ion battery using the high-performance NCM layered cathode is thoroughly investigated in **Chapter 7**. The electrochemical measurements performed with the support of a lithium reference electrode shed light on the effect of anode and cathode features on the full cell, thus elucidating the role played by a suitable electrode balancing.

Finally, **Chapter 8** summarizes the comprehensive studies and presents the conclusion. **Chapter 9** outlines the future research problems, challenges, and opportunities within glyme electrolyte formulations and transition metal oxide materials from a scientific and practical perspective.

Chapter 3 Experimental techniques

This chapter mainly describes the various experimental techniques employed in this thesis. Firstly, a description of the experimental chemical reagents is given. The rest part contains an overview of the principle of the experimental techniques used.

3.1 Experimental chemical reagents

The lists of the chemicals, materials, and their supplier are presented in **Table 3.1**.

Chemical	Formula or acronym	Purity or specification	Supplier
Aluminum	Al	Battery grade	MTI Corporation
Acetone ENSURE	C ₃ H ₆ O	99%	Sigma-Aldrich
Copper	Cu	Battery grade	MTI Corporation
Coin cell	CR-2032	Battery grade	Hohsen Corporation
Ethanol	C ₂ H ₅ OH	99.5%	Sigma-Aldrich
Lithium foil	Li	Battery grade	Sigma-Aldrich
Lithium iron phosphate	LiFePO ₄	Commercial product	Aleees
Nickel (II) oxide	NiO	99.8%	Sigma-Aldrich
N-methyl pyrrolidone	C ₅ H ₉ NO (NMP)	99.5% Anhydrous	Sigma-Aldrich
Polyvinylidene fluoride	PVDF 6020	Battery grade	Solvay
Super P carbon	C	Battery grade	Timcal
Sucrose	C ₁₂ H ₂₂ O ₁₁	99%	Sigma-Aldrich

Table 3.1 Primary experiment reagents.

3.2 X-ray diffraction (XRD)

XRD is a highly versatile, rapid, and non-destructive analytical technique that is extensively used for the qualitative and quantitative identification of crystallographic structure. The wavelength of X-rays has a range from 0.01 to 10 nm. Because the specific arrangement of atoms in the crystal forms a certain crystal plane and subsequently forms a regular diffraction pattern, the lattice parameters, cell volume, and crystallite sizes in the material can be calculated from the diffraction pattern.

A formula relating the interplanar spacing, Miller indices, and the lattice constant exists for each crystal system. For one orthorhombic system, it can be described in **Equation 3.1**.

$$d_{hkl} = \left[\frac{h^2}{a^2} + \frac{k^2}{b^2} + \frac{l^2}{c^2} \right]^{-1/2} \quad (3.1)$$

Where d_{hkl} is interplanar spacing (nm),

a, b, c is lattice parameters,

h, k, l is Miller indices.

A cathode X-ray tube is a vacuum tube where the characteristic X-rays are generated. The electrons are produced inside this tube by heating a tungsten filament. These electrons are pushed by applying a high voltage between 20 and 60 kV and then accelerated towards an anode target (e.g., copper). Once accelerated electrons accumulate sufficient energy to collide with the atoms' inner shell, the continuous X-rays spectra are generated. As the components of spectra, the K_α radiations are needed for XRD analysis rather than the K_β or L_α radiations.

When a ray of incident X-rays reflects off the surface of crystals, the path difference of the two waves reflected from successive planes is an integer multiple of the wavelength. Constructive interference is observed, as graphically presented in **Figure 3.1**.

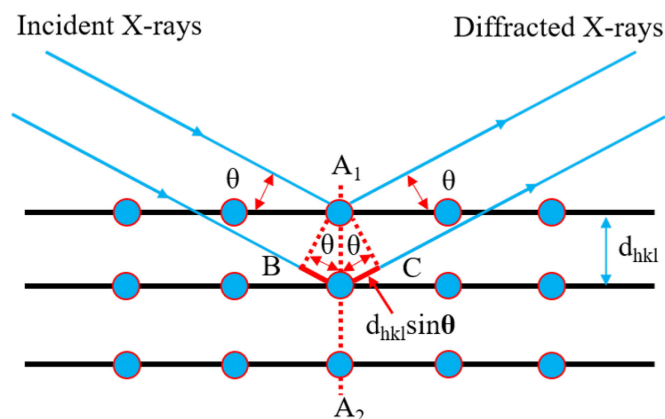


Figure 3.1 A simple illustration of the operational principle of the XRD facility.

When the condition for constructive interference is fulfilled, it is defined by the Bragg Law, as expressed on **Equation 3.2**.

$$n \cdot \lambda = 2 \cdot d_{hkl} \cdot \sin \theta \quad (3.2)$$

Equation 3.2 reveals the characteristic relationship between the wavelength (λ) and the angle (θ). In this equation,

n is an integer, the order of the reflection,

λ is the wavelength of incident wave,

d_{hkl} is the interplanar spacing specified by the Miller indices hkl ,

θ is angle between the hkl atomic planes with respect to both incidence and reflected beams.

An X-ray tube with copper target produces Cu $K\alpha_1$ radiation ($\lambda = 0.154$ nm), operated at 40 kV and 40 mA. For the XRD analyses carried out in this thesis, all the powders (LFP, NiO, Ni, and NiO@C) were measured on a Bruker D8 Advance diffractometer in Unife. The collected data were subjected to Rietveld refinement, which is a technique used to compare the calculated XRD value with the observed one by means of MAUD software. It can accurately calculate the lattice parameters, cell volume, and bond lengths. The calculated XRD diffraction peaks and the observed one can achieve better fitting through a least-squares fitting procedure to adjust

the crystal structure parameters and peak shape parameters, thereby obtaining suitable weighted-profile ($R_{wp}\%$) and goodness-of-fit (σ) values.

3.3 Thermogravimetric analysis (TGA)

In TGA, the changes in the mass of material are monitored as it is put in a crucible by varying instrument parameters (temperature or time) while being heated at a constant rate. By checking the weight loss or gain, this technique is very useful to understand the processes that a material undergoes, such as the loss of chemicals, oxidation of the material, and adsorption of gas.

TGA test in this thesis was conducted using a TGA Q500 from TA instruments in oxidizing atmosphere (usually refers to air) under flow rate of 50 mL min^{-1} . The sample (NiO@C) was filled in an alumina crucible (typically with masses around 15 mg) and heated at $10 \text{ }^\circ\text{C min}^{-1}$ rate over the maximum temperature of 800°C .

3.4 Scanning electron microscopy (SEM)

SEM is a very intuitive and useful technique for surface investigations (morphology, size, and composition) of the sample, which can produce two-dimensional images (from the nanometer up to the millimeter scale) by scanning the selected area. In a scanning electron microscope, an electronic gun produces and accelerates an electron beam. Subsequently, a high-energy electron beam scans the sample surface by the means of a raster scan pattern. This electron beam interacts with atoms at different depths and penetrates deep underneath the surface. Several signals are generated, such as secondary electrons (SEs) and back scattered electrons (BSEs).

The collection of low-energy (less than 50 eV) SEs is the conventional imaging mode in SEM. In this mode, SEs are emitted only very near the surface of the sample by inelastic scattering. BSEs are the primary electrons, reflected from the specimen through elastic scattering, which

are detected by the backscattered electron detector (BSD). Meanwhile, heavier elements appear brighter than lighter elements in the image because they have more giant nuclei and can deflect incident electrons more strongly. In addition to that, BSEs present higher energy than SEs, which can enter deeper into the specimen, providing more information about the sample morphology. For the imaging of the material, SEs and BSEs are generally collected.

3.5 Energy disperse X-ray spectroscopy (EDS)

EDS is a surface microanalysis technique based on the detection of characteristic X-rays, which can effectively identify the elements and composition of a specimen. Besides, it is commonly combined with SEM or TEM. As shown in **Figure 3.2**, characteristic X-ray emission spectra consist of spectral series, for instance, K, L, M, etc. When the inner shell of an atom strikes by the electron beam, the inner shell electron becomes excited and is banished from the atomic shell, leaving a positively charged electron-hole. The outer-shell higher-energy electrons fill up the vacancy in the inner shells, accompanied by the release of X-ray beams which are specific for each element.

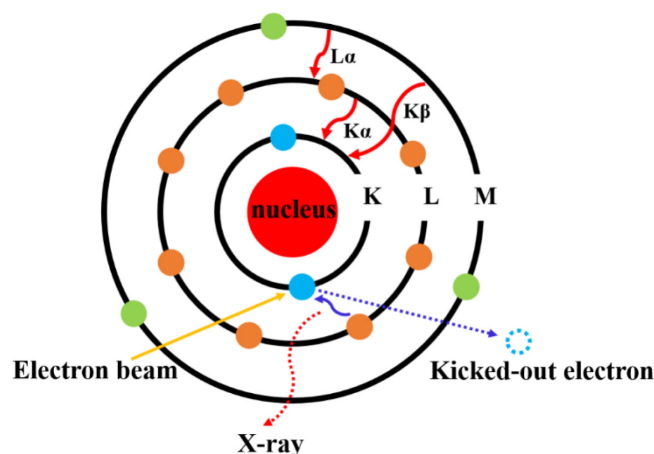


Figure 3.2 A simple illustration of the principle of EDS.

SEM images and SEM-EDS spectra acquired during this thesis were recorded through a Zeiss EVO MA10 microscope employing a thermionic electron gun with tungsten filament and an

INCA X-ACT Oxford instrument analyzer, respectively. Some SEM images were taken by a Zeiss EVO 40 microscope at Unife, equipped with a LaB₆ thermionic gun.

3.6 Transmission electron microscopy (TEM)

TEM has emerged as a powerful and ultrasensitive tool to observe and analyze the morphology of any given material, which can provide a much higher resolution image than SEM (in the range of a few angstroms). An incoming electron is transmitted through the specimen to form an image. The principle of TEM is that the focused and accelerated electrons formed by a certain voltage are projected onto the extremely thin specimen. After these electrons collide with the atoms within the specimen, their motive direction will be changed, yielding the scattering angle, resulting in the formation of a TEM image with different brightness. The TEM image is magnified, focused, and then shown in the imaging device. The size of the scattering angle is highly dependent on the density and thickness of the specimen.

A high voltage of 100–300 kV is the essential requirement for the majority of TEM system. The thickness of a sufficiently thin (less than 100 nm) is a basic choice for the specimen.

In TEM, an aperture that helps to limit the beam size can be inserted, for example, a metal strip with holes. When a beam of electrons goes through this aperture and is focused on a size-limited area, some of them will be scattered to particular angles, generating a diffraction pattern, which is called selected area electron diffraction (SAED).

High-angle annular dark-field scanning transmission electron microscopy (HAADF-STEM) is a scanning transmission electron microscope (STEM) technique. High-angle annular darkfield images are produced using an annular dark-field detector to collect most of the elastically scattered electrons at high angles.

Energy-filtered transmission electron microscopy (EFTEM) is a very helpful tool for the characterization of any given material, which can be used to obtain the phase distribution and

chemical bonding information at the material interface, thus acquiring high-resolution spatial mapping of elements.

Electron energy loss spectroscopy (EELS) is an effective characterization technique that monitors the ionization losses of incident electrons after the inelastic interaction with the specimen. EELS can obtain the physical and chemical information of the surface atoms by using the energy lost, yielding images with strong contrast effects.

TEM under different imaging modes can be combined with EELS, HAADF-STEM, or EFTEM, which provide a variety of effective methods for detecting the structure, composition, bonding, and spin of a specimen on the atomic size as well as understanding the structure-activity relationship.

In this doctoral work, TEM analyses were conducted on a JEOL JEM-2200FS microscope (Schottky emitter), operated at 200 kV, equipped with a CEOS' corrector for the objective lens and an in-column image filter (Ω -type).

Chapter 4 Characterization techniques

A series of techniques have been used in this thesis, such as chronoamperometry and galvanostatic measurements. This chapter contains detailed electrochemical and physical characterization techniques together with their basic principles.

4.1 Electrode preparation

An electrode was prepared by mixing the active material (i.e., LFP, NCM, NiO, Ni@C, and NiO@C), PVDF, and Super P carbon in a weight ratio of 8:1:1, respectively. These materials were grinded for about 10 to 15 minutes with NMP solvent, forming a uniform slurry. The slurry was then brought out and cast through a doctor blade on an aluminum or copper foil, dried at 70 °C for 3 h to remove NMP. The coated foil was cut into different size of disks (14 and 10 mm), pressed, and dried at 110 °C for 12 h under high-vacuum conditions. The final electrode was weighed for the battery assembly. The technological process of prepared electrodes is shown in **Figure 4.1**, see **Chapter 3** in the initial section for chemical acronyms.

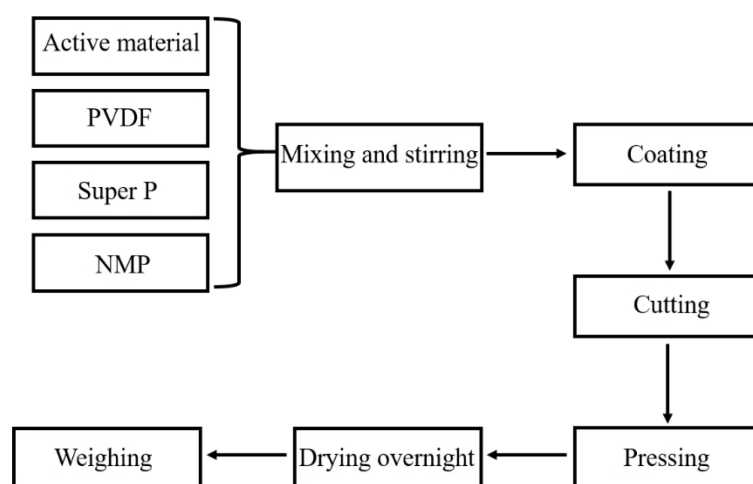


Figure 4.1 The technological process for preparing an electrode.

4.2 Coin cell assembly

The CR2032 coin cells were assembled in the glove box by using an active material coated electrode as the working electrode and a Whatman® GF/A glass-fiber as the separator. Lithium metal foils were served as counter and reference electrodes, and 1 M LiPF₆ in a mixture of EC and DMC was employed as the electrolyte. First, a lithium foil was cut into a disk (diameter of 14 mm). One spacer was gently pressed into the lithium disk with the aid of tweezers. The lithium disk glued with a spacer was placed facing upwards on the CR2032 coin cell case bottom. Subsequently, one separator moistened with electrolyte solution by the aid of a pipette was put over the lithium disk. The weight of the electrode disk was recorded, and the side with active material was put facing downwards over the separator sheet. Meanwhile, the other spacer was placed onto the electrode disk, stainless steel (SS) wave spring was put on it, and then the coin cell cap was put onto the top of all parts. Finally, the coin cell was pressed to finalize the battery assembly.

4.3 T-type cell

A typical T-type cell is composed of a three-way polyethylene holder and cylindrical stainless steel (SS) current collectors, as presented in **Figure 4.2**. The two-electrode T-type cells were fabricated by stacking a counter electrode (CE), a separator soaked with the electrolyte solution, and a working electrode (WE). Meanwhile, a reference electrode (RE) with or without lithium can be freely used in this cell configuration. Each electrode (WE, CE, and RE) is supported by one SS current collector.

Because the T-type cell is easily disassembled, the anode can be electrochemically activated by galvanostatic cycling in a two-electrode T-type half-cell as well as further employed in the lithium-ion full-cell [164]. As for the electrochemical measurement in lithium cells, using lithium metal disks as the reference and counter electrodes in three-electrode T-type cells are the common strategies for analyzing the electrode materials.

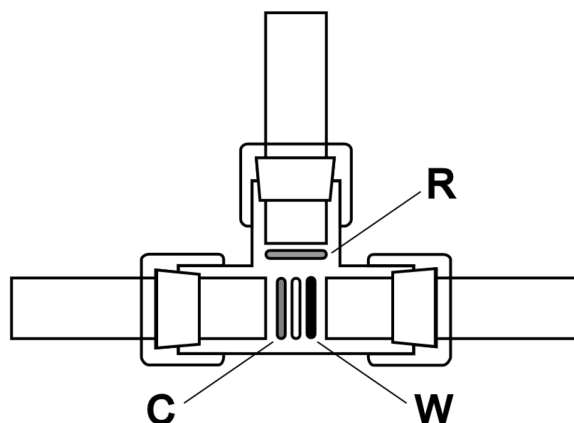


Figure 4.2 Schematic sketch of the three-electrode T-type cell assembly. Modified from Ref. [164].

4.4 Chronoamperometry

Resort of supplementary means, for example, chronoamperometry method can obtain the current value for the calculation of lithium transference number. Chronoamperometry is a technique that investigates the variation of the current response with time, also known as current transient technique.

The well-known Cottrell **Equation (4.1)** is used [165], which depicts the observed current as a function of $\frac{1}{\sqrt{t}}$ (from 0 to diffusion-limited conditions) after applying a large forward voltage step over the planar electrode.

$$I = \frac{nFSC\sqrt{D}}{\sqrt{\pi t}} \quad (4.1)$$

Where n refers to the number of electrons transferred in the reaction,

F is Faraday constant (around 96485 C mol^{-1}),

S is the area of the planer electrode (cm^2),

C and D refer to the concentration (mol cm^{-3}) and the diffusion coefficient ($\text{cm}^2 \text{s}^{-1}$) of the electroactive species, respectively.

Applying a single voltage step at t_0 , the electrode potential of the initial state (E_1) is changed to the working state (E_2), and the redox reaction occurs. The resulting current change is recorded as well. The alteration of the electrode potential and resulting current with time in the chronoamperometry are shown in **Figure 4.3**.

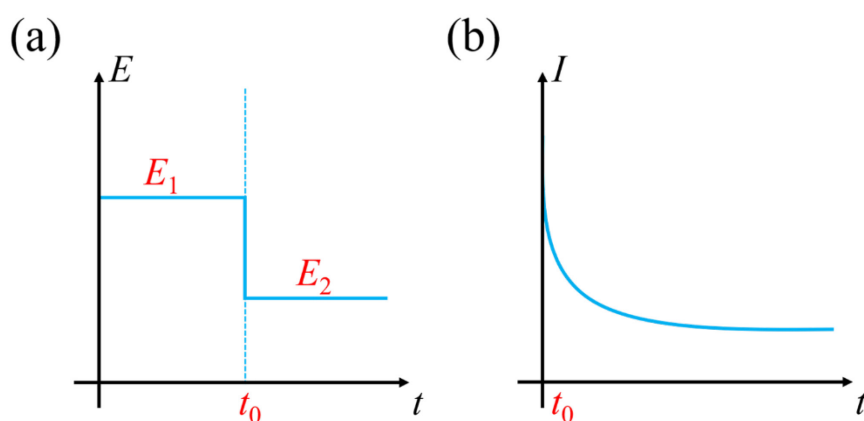


Figure 4.3 In the chronoamperometry; (a) electrode potential vs. time, and (b) the resulting current vs. time response.

Chronoamperometry technique in this doctoral work was carried out on a VersaSTAT MC Princeton Applied Research (PAR, AMETEK) potentiostat.

4.5 Electrochemical impedance spectroscopy (EIS)

Since EIS measurements are used extensively through the thesis, this section covers its key principles in detail. EIS is a versatile and highly sensitive characterization technique for studying the alternating current (AC) impedance characteristics of any given lithium cell. Herein, the ionic conductivity (denoted by σ), the lithium transference number, and the characteristics of the Li/electrolyte interphase of the electrolyte solutions were studied mainly by using the EIS measurements directly or indirectly.

A small amplitude sinusoidal voltage is used as a disturbance signal to measure the resulting current response over a wide frequency range. The resulting perturbing (voltage) wave (E_t) and current sine wave (I_t) can be given by **Equations 4.2** and **4.3**:

$$E_t = E_0 \sin(\omega t) \quad (4.2)$$

$$I_t = I_0 \sin(\omega t + \varphi) \quad (4.3)$$

The ratio E_t/I_t is defined as the impedance (Z).

It is possible to use the expression similar to Ohm's law to describe the impedance, described by **Equation 4.4**:

$$Z = \frac{E_t}{I_t} = \frac{E_0 \sin(\omega t)}{I_0 \sin(\omega t + \varphi)} = Z_0 \frac{\sin(\omega t)}{\sin(\omega t + \varphi)} \quad (4.4)$$

Where ω and φ are the radial frequency and the phase shift.

By applying Euler's relationship, the cell impedance $Z(\omega)$ is expressed as a complex function, as can be seen in **Equation 4.5**.

$$Z(\omega) = Z_0 (\cos \varphi + j \sin \varphi) \quad (4.5)$$

Where Z_0 and j are the impedance magnitude and the phase shift.

The impedance, Z_{eq} , in series is shown by **Equation 4.6**, whose contributions are additive. The contributions of Z_{eq} in parallel are inverse additive, as described in **Equation 4.7**.

$$Z_{eq} = \sum Z_n \quad (4.6)$$

$$Z_{eq} = \left(\sum \frac{1}{Z_n} \right)^{-1} \quad (4.7)$$

The Equivalent circuit model for EIS is composed of three basic electrical circuit elements in a combination of series or parallel, namely, resistors (R), capacitors (C), and inductors (L).

The expression for $Z(\omega)$ consists of a real and an imaginary part. The Nyquist plot can be applied to analyze the complex impedance function. In an ideal condition, a capacitor in parallel

with a resistor leads to a perfect semicircle, as represented in **Figure 4.4**. In this type of chart, the real part (Z_{re}) and the imaginary part (Z_{im}) lies on the X-axis and the Y-axis, respectively. The high-frequency data corresponds to the left side of the chart, and the lower frequencies are put on the right part, as can be seen from **Figure 4.4**. In this semicircle, the vector (arrow) of length $|Z|$ represents the impedance. When ω equals to zero, R refers to the electrolyte impedance.

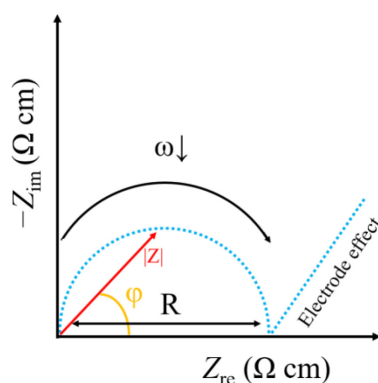


Figure 4.4 Nyquist plot for an ideal capacitor in parallel with a resistor.

According to the **Equation 4.8**, the ionic conductivity (σ) of the electrolyte can be obtained.

$$\sigma = \frac{L}{SR} \quad (4.8)$$

Where L is the thickness of the Teflon separator,

S is the inner area of circle on the Teflon separator,

R refers to the electrolyte impedance.

The EIS experiment was performed in an electrochemical cell by applying an alternating current voltage between the reference and working electrodes as well as measuring the resulting AC current at the working electrode. In this doctoral thesis, EIS tests were performed mainly to compare the lithium/electrolyte interphase resistance of different electrolytes and to investigate the resistance during the cycling tests at different rates by using the selected electrolyte formulation. The settings of experimental conditions (e.g., frequency of AC impedance and the applied voltage amplitude) are varying from the chapters.

4.6 Cyclic voltammetry (CV)

CV is the most widely used voltammetric technique for analyzing the reaction mechanism and kinetics of the electrode [166].

In the CV test, the electrode potential is swept repeatedly with time (scanning rate: mV s^{-1}) between the initial potential (E_{ini}) and the reverse potential (E_{rev}), as presented in **Figure 4.5a**. In the forward scan, the reduction process occurs from E_{ini} to E_{rev} , namely, $A + e^- \rightarrow B$. The resulting current and its peak potential are called anodic current (I_{pa}) and anodic peak potential (E_{pa}), as revealed in **Figure 4.5b**. In the reversible process, the potential scans backwardly from E_{rev} to E_{ini} to cause oxidation ($B - e^- \rightarrow A$). Its current and peak potential corresponds to the cathodic current (I_{pc}) and cathodic peak potential (E_{pc}), respectively.

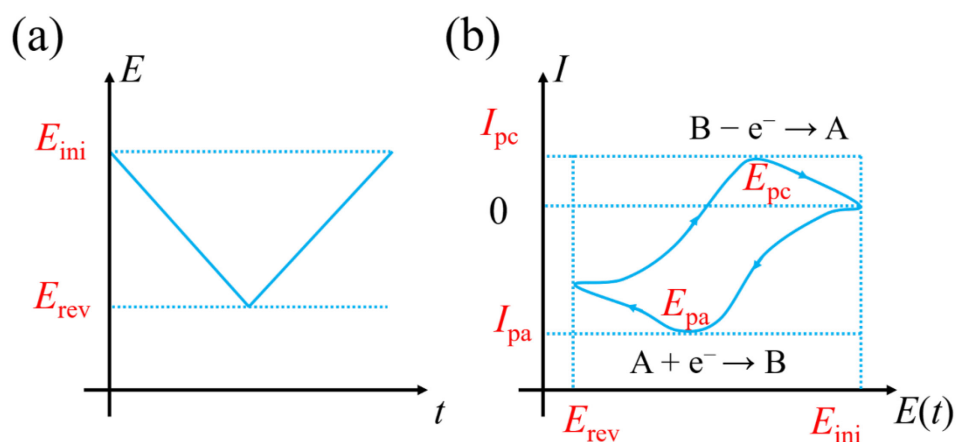


Figure 4.5 (a) Cyclic potential sweep, (b) typical cyclic voltammogram.

Peak shape is observed in the CV, which is affected by the diffusion of reactants and the rate of electron transfer. It should be mentioned that the electrode potential can affect the electrode transfer rate, but it has no effect on the diffusion speed.

The peak potential difference (ΔE) delivers critical information during the redox process (**Equation 4.9**).

$$\Delta E = E_{\text{pa}} - E_{\text{pc}} \quad (4.9)$$

For a reversible $n e^-$ transferred reaction, the ideal potential value of ΔE is $56.5/n$ mV. However, the observed values are usually greater.

4.7 Linear sweep voltammetry (LSV)

LSV is a well-used voltammetric technique for investigating the electron transfer kinetics and transport properties of the electrochemical systems [167].

This technique is similar to that of CV, but the applied potential is scanned from a lower value (V_1) to an upper one (V_2), as described in **Figure 4.6a**. It is related to simultaneously measuring the current at a working electrode when the voltage is swept from V_1 to V_2 at a constant rate between a working electrode and a reference electrode, see **Figure 4.6b**.

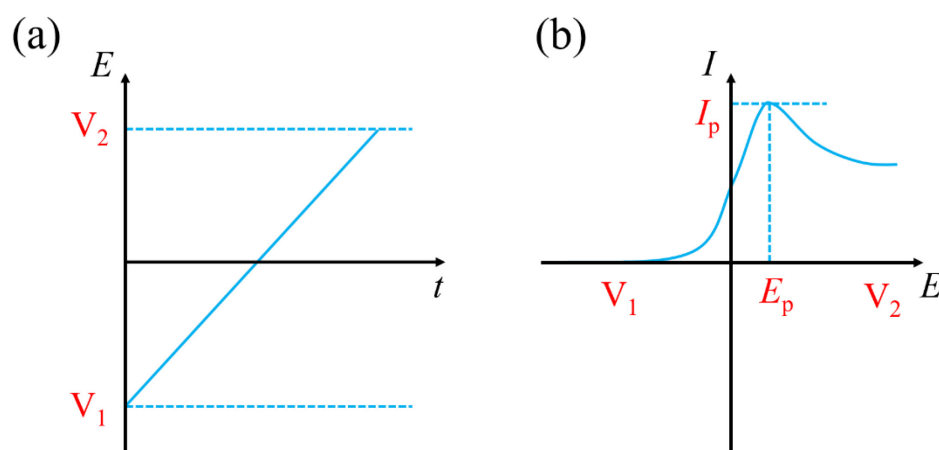


Figure 4.6 (a) Linear potential sweep, (b) typical linear sweep voltammogram.

The LSV in this thesis were performed mainly to obtain the ESW of the selected electrolyte, which contributes to widely investigate the stability of the electrolyte in battery systems [168].

4.8 Galvanostatic measurements

Galvanostatic measurements are generally used to assess the electrochemical properties (e.g., capacity retention, cycling stability, and rate performance) of the given material. All the

electrochemical tests in this doctoral thesis were performed on CR2032 coin-type cells and T-type cells. It involves applying a constant current to a cell while the capacity and potential are monitored.

The galvanostatic measurements in this thesis were carried out by means of a MACCOR Series 4000 battery test system. As for the potential ranges and current rates in galvanostatic measurements, the experimental settings can be found in different chapters.

Chapter 5 Glyme-based electrolytes for lithium metal batteries using insertion electrodes

5.1 Introduction

This chapter is based on the content presented in *Electrochimica Acta*, 306 (2019) 85-95, entitled “Glyme-based electrolytes for lithium metal batteries using insertion electrodes: An electrochemical study”, copyright (2019) Elsevier.

Lithium metal cells have been limited mainly to the primary configuration so far, except for a few examples of rechargeable cells, owing to possible growth of lithium dendrites upon cycling and low stripping/plating efficiency [169]. The optimization of suitable electrolyte solutions plays a crucial role in mitigating the issues affecting the lithium metal anode and allowing reversible electrodeposition processes and low risks of thermal runaways [170]. Glyme-based electrolytes are typically lowlily flammable with respect to the standard carbonate-based electrolytes. Their physical-chemical and electrochemical features may be favorably tuned by changing the ether chain length [145]. High-molecular-weight glymes ensure good thermal stability and broad electrochemical stability window, although they have high viscosity and high freezing point [145].

In this chapter, we studied the electrochemical features of glyme-based solutions of various lithium salts as electrolytes for Li/LFP cells. DEGDME and TREGDME were selected as suitable solvents to achieve low viscosity, hence higher conductivity with respect to long-chain glymes [150,171], while either LiFSI or LiTFSI, or LiBETI were chosen as salts. A comparative electrochemical study was done on the six solutions using a series of electrochemical techniques, namely, voltammetry, impedance spectroscopy, chronoamperometry, and galvanostatic cycling measurements. The possible use of the glyme-based solutions in lithium cells with LiFePO₄ insertion cathode were also evaluated.

5.2 Results and discussion

A suitable electrolyte solution for lithium metal battery applications should ensure fast ion transport to achieve high current density [172]. It is noteworthy that the electrolyte formulation in terms of ether chain extension and lithium salt composition may play a crucial role by determining viscosity, ion solvation ability, and ion association degree, i.e., parameters that strongly affect ionic conductivity and lithium transference number (t^+) [173]. The ionic conductivity was investigated by EIS within the temperature range from about 20 to about 80 °C (**Figure 5.1**), and the t^+ number (**Figure 5.2**) was calculated by the electrochemical method [174].

Figure 5.1 reveals the expected remarkable effect of the glyme-chain length on the ionic conductivity, with values of the order of 10^{-2} S cm^{-1} for the DEGDME-based solutions (panel **a**) and 10^{-3} S cm^{-1} for the TREGDME-based ones (panel **b**), which are normally considered suitable for battery application [145]. As for the lithium salt composition, EIS suggests that the anion size controls the charge mobility within DEGDME-based electrolyte solutions, most likely due to the effects of the anion charge density on the solvation shell characteristics [175,176]. Thus, the ionic conductivity of DEGDME-based solutions increases as the anion size increases from LiFSI to LiTFSI and to LiBETI, as demonstrated in **Figure 5.1a**. On the other hand, TREGDME-based electrolytes do not exhibit the same trend, while they have ionic conductivity barely depending on the salt composition (see **Figure 5.1b**). This observation may suggest a complex effect of chain length on the ion solvation ability [177], which may be further investigated using different techniques than electrochemistry.

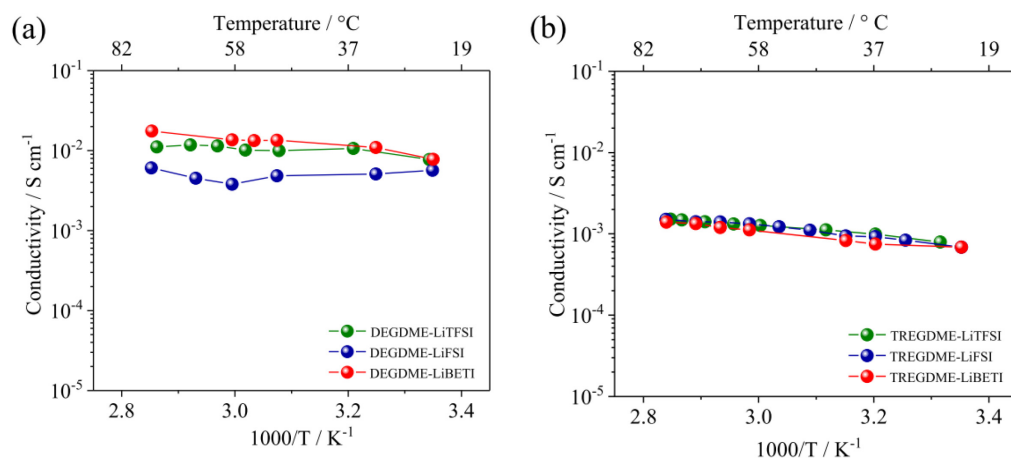


Figure 5.1 Ionic conductivity of the (a) DEGDME-LiTFSI, DEGDME-LiFSI, DEGDME-LiBETI, and (b) TREGDME-LiTFSI, TREGDME-LiFSI, TREGDME-LiBETI electrolyte solutions determined by EIS measurements within the 20 – 80 °C temperature range in symmetric blocking electrodes cell.

The t^+ number shown in **Figure 5.2** represents the fraction of charge carried by Li^+ through the electrolyte solutions. This parameter has been determined at 25 and 50 °C by performing EIS and chronoamperometry measurements on symmetrical lithium cells. The measurements indicate a raise of lithium transference number with increasing chain length from DEGDME (**Figure 5.2a**) to TREGDME (**Figure 5.2b**), likely due to stronger solvation of the relatively big anions promoted by a longer glyme with respect to a shorter one, which decreases the anion mobility compared to the easily solvated small Li^+ . Meanwhile, increasing anion size reduces its mobility and consequently leads to the rise of the lithium transference number from LiTFSI and LiFSI, which exhibit comparable values, to LiBETI (panels **a** and **b** of **Figure 5.2**). These observations further suggest that the relative size of anion and glyme can control the solvation characteristics, leading to significant effects on conductivity and Li^+ transport [176].

Li^+ transference numbers at 50 °C are represented in **Figure 5.2**. The results indicate a general decrease of the t^+ number by increasing the temperature as likely because of the increase of anions and solvent molecules motion into the electrolyte and to enhanced solvation, which hinders the transport of the Li^+ [177]. Hence, the transference numbers drop from values of about 0.5 – 0.8, depending on the electrolyte solution, to the values of about 0.3 – 0.5.

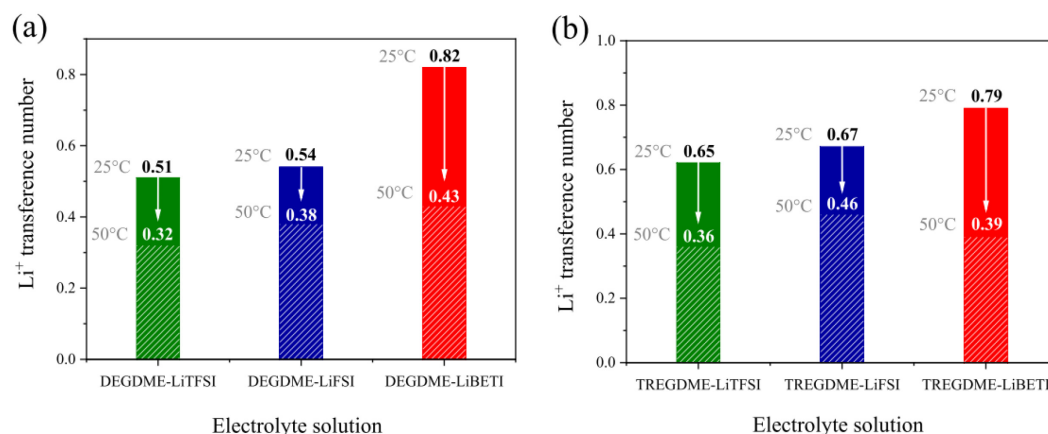


Figure 5.2 Lithium transference number at 25 °C and 50 °C of the **(a)** DEGDME-LiTFSI, DEGDME-LiFSI, DEGDME-LiBETI and **(b)** TREGDME-LiTFSI, TREGDME-LiFSI, TREGDME-LiBETI electrolyte solutions.

A remarkable effect of the electrolyte composition on the ESW is observed in **Figure 5.3** in which voltammetry experiments are performed in lithium cells employing carbon coated on metal foils (either Cu or Al). Panels **a** and **c** of **Figure 5.3** show that the solutions employing LiBETI have the highest oxidative stability (up to 4.6 V vs. Li⁺/Li), which suggests possible application with cathodes that have working voltage above 4.0 V vs. Li⁺/Li [164], while solutions using LiFSI reveal the lowest one (about 4.1 – 4.2 V vs. Li⁺/Li). Intermediate values of the stability to oxidation are observed for solutions using LiTFSI (about 4.2 – 4.4 V vs. Li⁺/Li). On the other side, the rise of the chain length from DEGDME (**Figure 5.3a**) to TREGDME (**Figure 5.3c**) hardly affects the oxidative stability of solutions using LiBETI salt, increases one of solutions using LiFSI from about 4.1 to about 4.2 V vs. Li⁺/Li, and decreases one of solutions using LiTFSI from about 4.4 to about 4.2 V vs. Li⁺/Li, thereby revealing a slight effect of the increasing of chain length from 2 to 3 ether groups, depending on the chemical nature of the dissolved salt [145]. It is worth mentioning that all the electrolyte solutions exhibit stability to oxidation suitable for application with LiFePO₄ olivine insertion cathode, which operates at about 3.5 V vs. Li⁺/Li [48]. The high-potential range is surveyed in panels **b** and **d** of **Figure 5.3**, which show the CV profiles for the DEGDME-based and TREGDME-based electrolytes, respectively. The first reduction scan in **Figure 5.3b** reveals the formation of the SEI over the carbon electrode coated on copper below 1.1 and at about 0.4

and 0.6 V vs. Li^+/Li for DEGDME dissolving LiTFSI, LiFTSI, and LiBETI, respectively [178]. The subsequent cycles display for all the DEGDME-based electrolytes reversible electrochemical processes ranging between 1.4 and 0 V vs. Li^+/Li , which may be attributed to Li^+ insertion/deinsertion within the carbon material and to possible lithium plating/stripping [179]. The TREGDME-based electrolytes show a similar voltammetry response in the high-potential range (**Figure 5.3d**), with SEI formation over carbon around 1.3, 0.6, and 0.7 V vs. Li^+/Li upon the first reduction scan for LiTFSI, LiFTSI, and LiBETI, respectively, and reversible lithium insertion and plating below 1.4 V vs. Li^+/Li . Therefore, all the electrolytes show suitable stability to reduction characterized by the absence of parasitic reactions after the first cycle, which is characterized by a SEI formation at potential depending on the chemical nature of the dissolved lithium salt, with particular focus on LiTFSI, which has the highest value, that is, above 1 V vs. Li^+/Li .

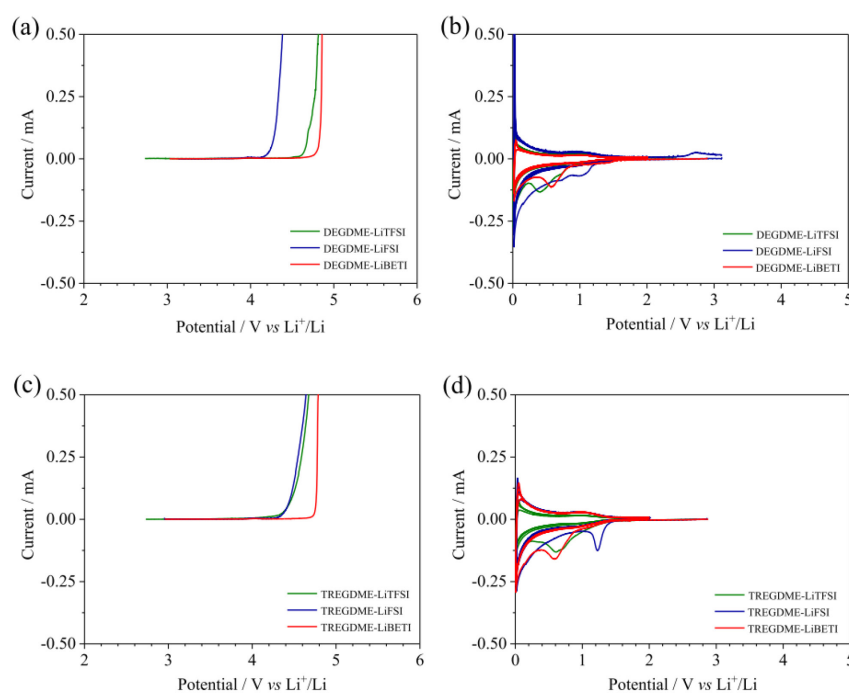


Figure 5.3 Electrochemical stability window of the (a, b) DEGDME-LiTFSI, DEGDME-LiFTSI, DEGDME-LiBETI and (c, d) TREGDME-LiTFSI, TREGDME-LiFTSI, TREGDME-LiBETI electrolyte solutions determined by LSV (high-potential region, panels a and c) and by CV (low-potential region, panels b and d).

Figure 5.4 shows the lithium/electrolyte interphase resistance trend upon 30 days of storage of symmetrical lithium cells as determined by NLLS analysis of impedance spectra [180,181]. **Figure 5.4a** reveals for the DEGDME-based solutions interphase resistance values increasing during the first day of aging to about 300 Ω for LiFSI, 150 Ω for LiTFSI, and 720 Ω for LiBETI. The resistance further rises to 500 Ω after 6 days for DEGDME-LiFSI and to 830 Ω after 4 days for DEGDME-LiBETI, while gradually decreases to about 300 and 350 Ω , respectively, upon 30 days of cell storage, according to SEI partial dissolution and consolidation phenomena [122]. Notably, the DEGDME-LiTFSI solution exhibits lower interphase resistance characterized by a slight, rather constant increase upon aging, with maximum values below 230 Ω . **Figure 5.4b** reveals different trends of R_i for the solutions using TREGDME upon the 1st day of aging, which depends on the lithium salt. Thus, the electrode/electrolyte interphase resistance increases during the 1st day from about 110 and 200 Ω to 190 and 390 Ω for TREGDME-LiFSI and TREGDME-LiBETI, respectively, while decreases from about 230 to 180 Ω for TREGDME-LiTFSI. Afterwards all the TREGDME-based solutions exhibit a fluctuation of the lithium/electrolyte interphase resistance around 300 Ω , thus suggesting stabilization of the SEI upon 30 days [122]. **Figure 5.4** clearly shows lower resistance values and excellent stability over time towards lithium metal for the DEGDME-LiTFSI, TREGDME-LiFSI, and TREGDME-LiTFSI compositions.

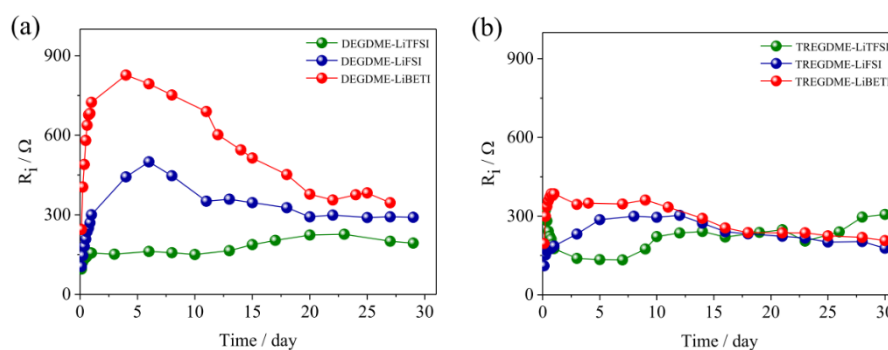


Figure 5.4 Lithium/electrolyte interphase resistance for the (a) DEGDME-LiTFSI, DEGDME-LiFSI, DEGDME-LiBETI and (b) TREGDME-LiTFSI, TREGDME-LiFSI, TREGDME-LiBETI formulations in Li/Li symmetrical cells as calculated by NLLS analysis of EIS data during 30 days of aging at 25 $^{\circ}\text{C}$.

Figure 5.5 shows the voltage profiles of lithium stripping/deposition measurements performed by galvanostatic cycling of symmetrical lithium cells for the electrolytes using DEGDME (panel **a**) and TREGDME (panel **b**). Indeed, Li/DEGDME-LiBETI/Li and Li/DEGDME-LiFSI/Li cells show a gradual increase of polarization during the first day from about 60 mV to about 90 mV, while the polarization of the Li/DEGDME-LiTFSI/Li cell increases from about 30 mV to about 40 mV due to the SEI modification by the electrochemical process (**Figure 5.5a**). Subsequently, the overvoltage of the Li/DEGDME-LiBETI/Li cell slightly decreases to 80 mV and remains rather stable by 10 days of cycling, while the DEGDME-LiFSI and DEGDME-LiTFSI solutions exhibit a reduction of the cell polarization to values lower than 30 mV upon cycling, likely due to the already observed partial SEI dissolution and consolidation phenomena [122]. The data of **Figure 5.5a** indicate that the cycling test leads to the formation of a very stable and lowly resistive SEI film for DEGDME solutions using LiTFSI and of remarkably resistive SEI film for solutions using LiBETI and LiFSI. Interestingly, the resistance of the cell using DEGDME-LiBETI solution remains stably high by cycling, while the cell using DEGDME-LiFSI solution gradually decreases, reaching a value similar to DEGDME-LiTFSI.

The change from DEGDME to TREGDME solvent significantly modifies both the trend and the steady-state values of cell polarization (**Figure 5.5b**). Indeed, the cell using TREGDME-LiBETI shows an initial polarization of about 30 mV, slightly increasing and stabilizing by 10 days of cycling to about 45 mV, which are remarkably lower values compared to DEGDME-LiBETI. Analogously, the cell using TREGDME-LiFSI reveals lower initial polarization with respect to DEGDME-LiFSI, with value decreasing from about 30 mV to about 15 mV by cycling, while TREGDME-LiTFSI electrolyte shows higher initial polarization value (about 90 mV) compared to DEGDME-LiTFSI during the early stages, which rapidly decreases by few cycles and stabilizes to at about 35 mV. **Figure 5.5** suggests LiTFSI and LiFSI as the most performing salts in terms of low polarization of lithium stripping/deposition process, and TREGDME as the preferred solvent.

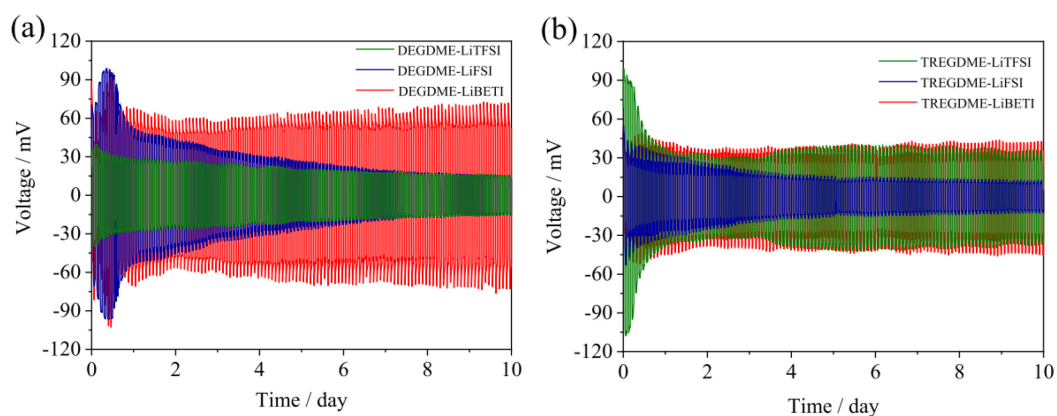


Figure 5.5 Voltage profiles of Li/Li symmetrical cells employing **(a)** DEGDME-LiTFSI, DEGDME-LiFSI, DEGDME-LiBETI, and **(b)** TREGDME-LiTFSI, TREGDME-LiFSI, TREGDME-LiBETI electrolyte solutions, cycled at a constant current density of 0.1 mA cm^{-2} . Step time: 1h.

A galvanostatic lithium stripping/deposition cycling in Li/Li symmetrical cells was performed and repeated after a rest period of 24 h, collecting electrochemical impedance spectroscopy before and after each test. **Figure 5.6** shows the related voltage profiles and the Nyquist plots of the EIS before the test (P_1), after 5 cycles (P_2), upon 24 h of rest after cycling (P_3), and after additional 5 cycles (P_4) for the various electrolytes.

Very interestingly, the measurements indicate a rather good Li/electrolyte interphase, with low values of stripping/deposition polarization (limited to values below 20 mV) stable or slightly decreasing by the ongoing cycles, and slightly changing resistances values upon a time. Hence, this measurement further demonstrates the suitability of the electrolyte studied herein for lithium batteries.

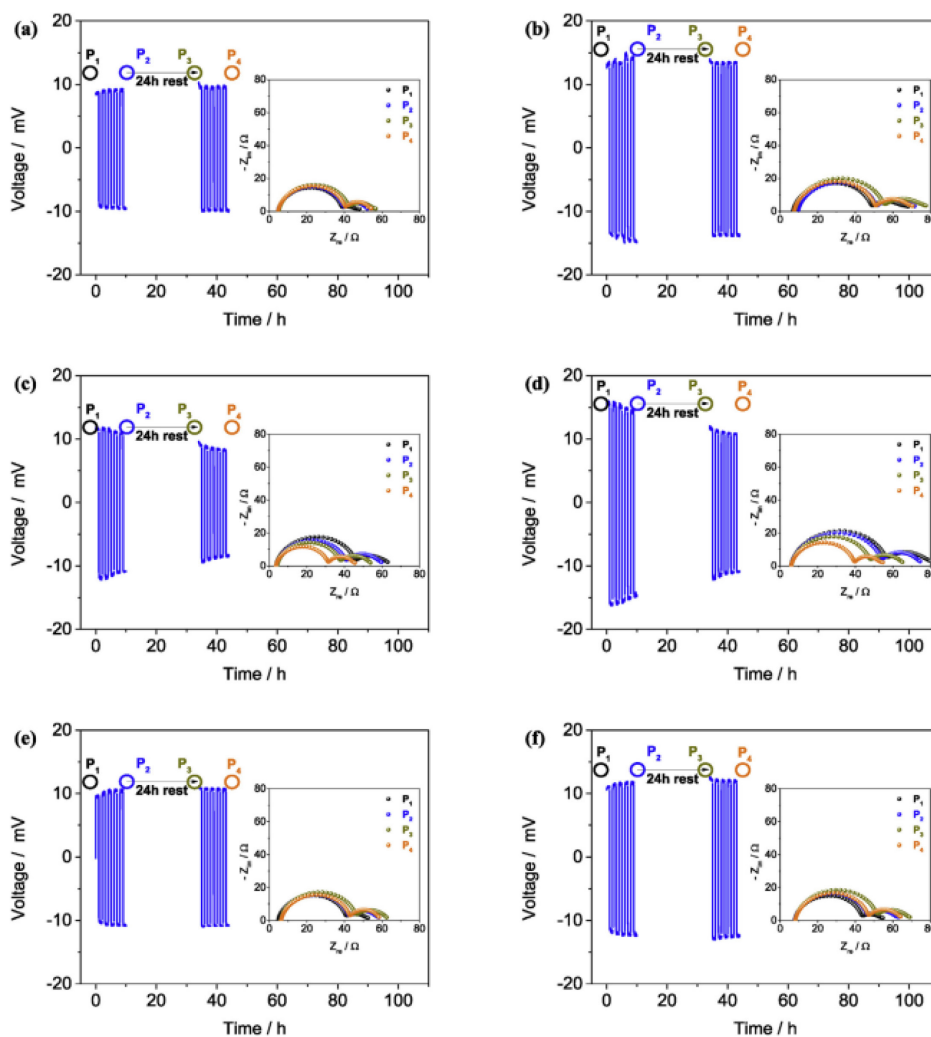


Figure 5.6 Voltage profiles of lithium stripping/deposition galvanostatic cycling tests in symmetrical Li/Li cells and corresponding Nyquist plots of the EIS before the test (P_1), after 5 cycles (P_2), upon 24 h or rest after above cycling (P_3), and after additional 5 cycles (P_4) using (a) DEGDME-LiTFSI, (b) TREGDME-LiTFSI, (c) DEGDME-LiFSI, (d) TREGDME-LiFSI, (e) DEGDME-LiBETI, and (f) TREGDME-LiBETI.

Additionally, lithium stripping/deposition cyclic voltammetry tests of Li/Cu cells have been performed using the various solutions studied, as reported in **Figure 5.7**. The CVs clearly reveal a polarization and a stripping/deposition magnitude (current) strongly depending on the adopted salt/solvent combination. Furthermore, the graphs generally indicate a low polarization value ranging from about 0.05 V to 0.15 V, thus further suggesting the suitability of the studied electrolytes for battery application.

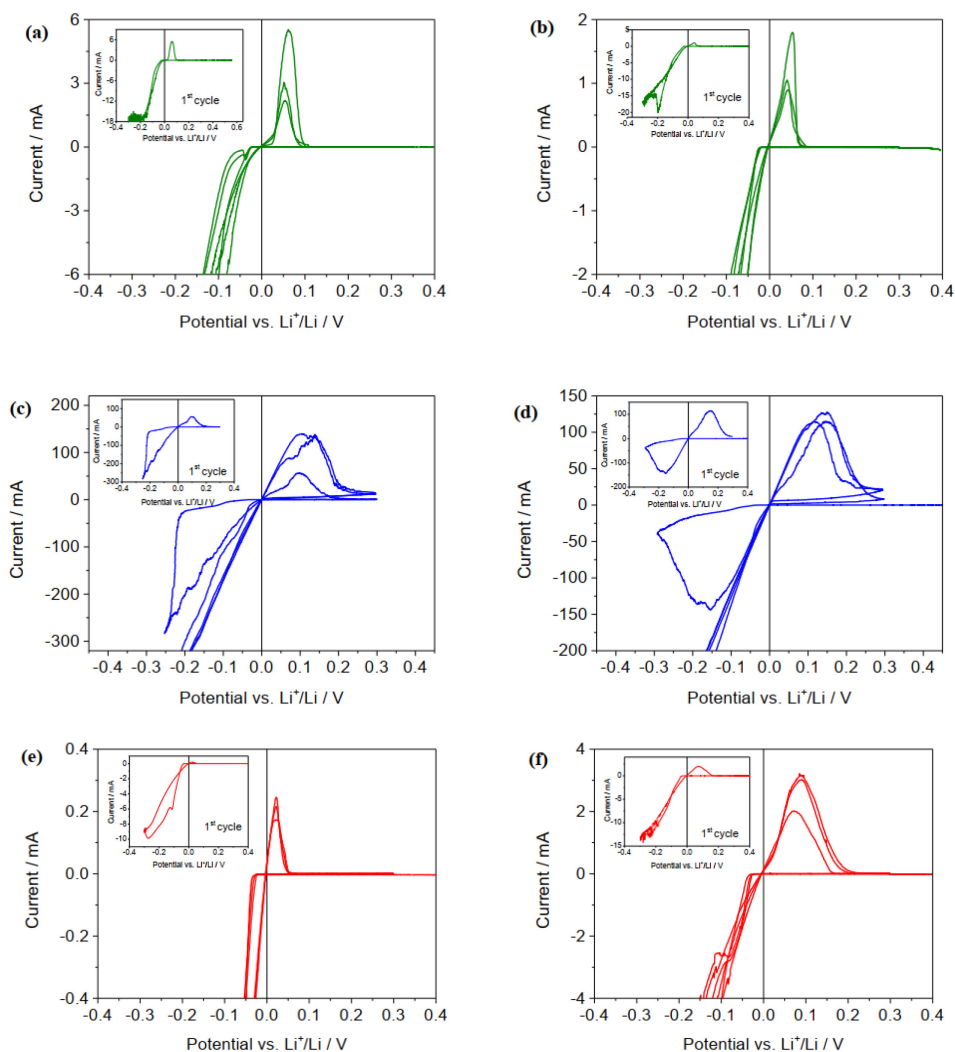


Figure 5.7 Lithium stripping/deposition voltammetry tests of Li/Cu cells using (a) DEGDME-LiTFSI, (b) TREGDME-LiTFSI, (c) DEGDME-LiFSI, (d) TREGDME-LiFSI, (e) DEGDME-LiBETI, and (f) TREGDME-LiBETI. CVs performed within -0.3 and 0.3 V using a scan rate of 0.1 mV s^{-1} .

Various Li/LFP cells employing the electrolyte solutions were assembled and comparatively studied by galvanostatic cycling at a rate of $C/3$ ($1C = 170 \text{ mA g}^{-1}$). **Figure 5.8** displays the cycling behavior (panels a and c) and the voltage profiles (panels b and d) for DEGDME- and TREGME-based electrolytes (**Figure 5.8a-b** and **c-d**, respectively). The measurements reveal a remarkable effect of the electrolyte formulation on the cell performances. The Li/DEGDME-LiBETI/LFP cell exhibits a reversible capacity approaching 130 mAh g^{-1} after initial activation,

likely because of the wetting of cathode. However, its capacity drops to 0 mAh g⁻¹ after 50 cycles (**Figure 5.8a**) owing to a gradual polarization increase. The Li/DEGDME-LiFSI/LFP cell exhibits a comparable activation trend and a steady-state capacity (134 mAh g⁻¹) without any decay upon 100 cycles. The Li/DEGDME-LiTFSI/LFP cell delivers an initial discharge capacity of 153 mAh g⁻¹ and a stable reversible capacity of 147 mAh g⁻¹ at the 100th cycle with capacity retention as high as 96.1% (**Figure 5.8a**). **Figure 5.8b** shows the related voltage profiles of the 5th cycle of the various electrolytes. The cells exhibit the typical voltage plateau of LFP materials centred at about 3.45 V [182] with small polarization. The Li/DEGDME-LiTFSI/LFP cell shows the best performances in terms of reversible capacity, cycling stability, and cell polarization among the three configurations (see panels **a** and **b** of **Figure 5.8**).

Panels **c** and **d** of **Figure 5.8** evidence a similar trend in terms of performances for the TREGDME-based solution but suitable cycling behavior for the Li/TREGDME-LiBETI/LFP cell. The cells using TREGDME-LiBETI, TREGDME-LiFSI, and TREGDME-LiTFSI deliver steady-state capacities of 137, 144, and 151 mAh g⁻¹, respectively, with negligible fading after 100 cycles (see **Figure 5.8c**). The Li/TREGDME-LiBETI/LFP and Li/TREGDME-LiTFSI/LFP cells exhibit at the 5th cycle similar polarization of the process at about 3.45 V [183], as displayed in **Figure 5.8d**, while the Li/TREGDME-LiFSI/LFP one has polarization as low as 7 mV. It is worth noting that **Figure 5.8** suggests a difference in the wetting ability of the cathode by the electrolyte solution among the six compositions investigated. The solutions using LiFSI are apparently more affected by wetting than those using the large BETI⁻ anion since they show an activation process leading to a gradual increase of capacity upon cycling. In contrast, the solutions employing LiTFSI are apparently not affected by the electrode wettability.

Therefore, both cells using LiTFSI show the most remarkable cycling performances, which may be ascribed to the high conductivity and favorable lithium passivation properties of the related electrolyte solutions with low-molecular-weight glymes. The other formulations exhibit suitable electrochemical behavior for application in lithium metal batteries, except for the DEGDME-LiBETI, which shows inferior performances.

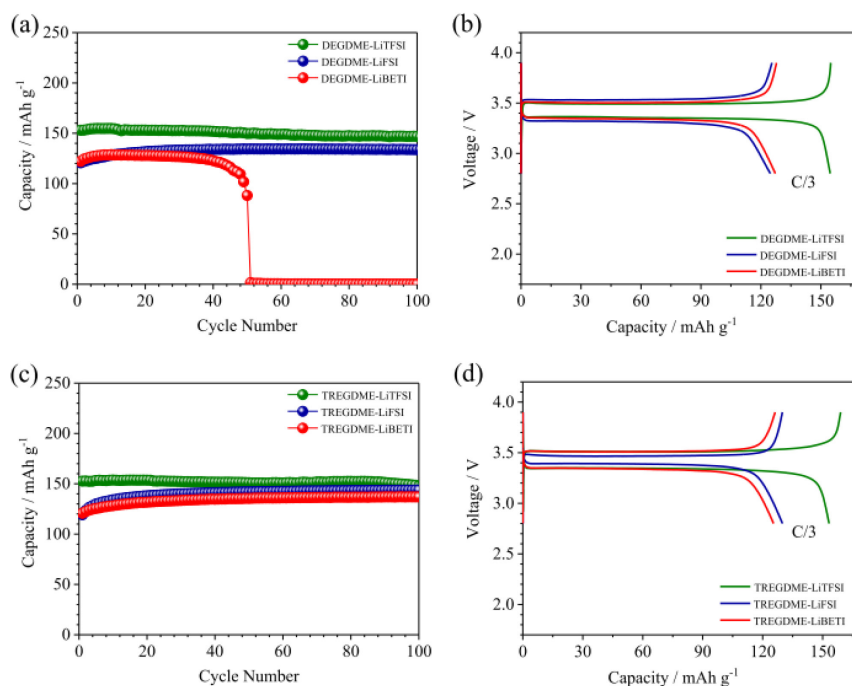


Figure 5.8 Galvanostatic cycling at a C/3 rate of Li/LFP cells using **(a, b)** DEGDME-LiTFSI, DEGDME-LiFSI, DEGDME-LiBETI, and **(c, d)** TREGDME-LiTFSI, TREGDME-LiFSI, TREGDME-LiBETI electrolyte solutions in terms of cycling behavior (panels **a** and **c**) and of voltage profiles of the 5th cycle (panels **b** and **d**).

5.3 Conclusion

In this chapter, the decrease of chain length from triglyme to diglyme led to an increase of the ionic conductivity from about 10^{-3} to about 10^{-2} S cm^{-1} , and to a decrease of the lithium transference number. The electrochemical investigation suggested an effect of the anion size on the cation transference number, with values of about 0.8 for DEGDME-LiBETI and TREGDME-LiBETI, 0.7 for TREGDME-LiTFSI and TREGDME-LiFSI, and 0.5 for DEGDME-LiTFSI and DEGDME-LiFSI.

All the electrolyte formulations were electrochemically stable within the potential range from 0 to above 4 V vs. Li^+/Li , with decomposition starting at a potential as high as 4.6 V vs. Li^+/Li when LiBETI was employed.

However, the use of LiBETI affected the formation of a stable and low-resistance SEI over the lithium metal anode, particularly in the DEGDME solvent. Accordingly, the Li/DEGDME-LiBETI/LFP cell showed abysmal performance, while the Li/TREGDME-LiBETI/LFP one exhibited suitable behavior but lower capacity than that of the other TREGDME-based cells.

The LiTFSI-based electrolytes presented the best electrochemical behavior in lithium metal cells with LFP cathode, delivering reversible capacity ranging from 147 mAh g⁻¹ to 153 mAh g⁻¹ during 100 cycles. Such results may be of definite interest to develop suitable electrolytes for rechargeable batteries employing the high-energy lithium metal anode.

5.4 Experimental section

Prior to electrolyte preparation, the salts were dried under vacuum at 110 °C for 24 h, while the solvents were dried under molecular sieves (5 Å, Sigma-Aldrich) until the water content was below 10 ppm, as determined by 899 Karl Fischer Coulometer, Metrohm. The electrolyte solutions are indicated below by the acronyms listed in **Table 5.1**.

Solvent	Salt	Acronym
Diethylene glycol dimethyl ether (DEGDME)	LiTFSI	DEGDME-LiTFSI
Diethylene glycol dimethyl ether (DEGDME)	LiFSI	DEGDME-LiFSI
Diethylene glycol dimethyl ether (DEGDME)	LiBETI	DEGDME-LiBETI
Triethylene glycol dimethyl ether (TREGDME)	LiTFSI	TREGDME-LiTFSI
Triethylene glycol dimethyl ether (TREGDME)	LiFSI	TREGDME-LiFSI
Triethylene glycol dimethyl ether (TREGDME)	LiBETI	TREGDME-LiBETI

Table 5.1. List of solvents and salts used for preparing the electrolyte samples and corresponding acronyms.

5.4.1 Electrolyte preparation

Six electrolyte solutions were prepared in an Ar-filled glovebox by dissolving either LiFSI, (Sigma-Aldrich), LiTFSI (Sigma-Aldrich), or LiBETI (Sigma-Aldrich) in both DEGDME (Sigma-Aldrich) and TREGDME (Sigma-Aldrich) solvents with a molar concentration of 1 mol kg⁻¹.

5.4.2 Electrode preparation

An electrode was prepared from slurry made of LiFePO₄ (LFP) powder, polymeric binder (PVDF 6020, Solvay), and conductive carbon (Super P, Timcal) in weight proportion of 80:10:10, using 1-methyl-2-pyrrolidinone (NMP) as solvent. The slurry was coated on an aluminum foil (thickness of 15 μm, MTI Corporation) through a doctor blade and then dried for 3 h at 70 °C. The obtained foil was cut into the form of 14 mm disks followed by vacuum drying at 110 °C overnight. The final active material loading over the electrode foil was about 5.4 mg cm⁻². Carbon electrodes coated on either aluminum (Al) or copper (Cu) were also prepared using the doctor blade technique by casting of Super P carbon and PVdF 6020 (Solvay) with a weight ratio of 80:20. These electrodes were cut into 10 mm disks and subsequently dried at 110 °C under vacuum for 12 h.

5.4.3 Electrochemical measurements for electrolyte

The ionic conductivity was studied by EIS within temperature ranging from 20 °C to 80 °C, using symmetric stainless steel/electrolyte/stainless steel CR2032 coin-cells equipped with a Teflon separator to fix the thickness. EIS was performed in the frequency range of 500 kHz to 10 Hz with an alternate signal amplitude of 10 mV.

The transference number for the cation (t⁺) of the electrolyte solutions was calculated by means of the classic electrochemical method [174]. The t⁺ number is given by **Equation 5.1**.

$$t^+ = \frac{I_{SS} (\Delta V - I_0 R_0)}{I_0 (\Delta V - I_{SS} R_{SS})} \quad (5.1)$$

Where ΔV is the applied potential,

I_0 is the initial current,

I_{SS} is the steady-state current,

R_0 and R_{SS} are the lithium/electrolyte interphase resistance before and after the polarization, respectively.

Chronoamperometry and EIS measurements were carried out on two-electrode Li/Li symmetrical T-type cells employing 10 glass fiber separators (Whatman®, GF/D). The increase of cell thickness due to many separators leads to higher electrolyte resistance with respect to standard cells using one separator. This condition favors the application of the method proposed by Evans et al. [174], which allows the determination of t^+ from a steady-state condition where the current flow is mainly controlled by the cation transport into the electrolyte bulk, thus limiting perturbations due to passivating layers at the electrode/electrolyte interphase.

EIS was performed before and after the chronoamperometry over frequency ranging from 500 kHz to 100 mHz with an alternate signal amplitude of 10 mV. Chronoamperometry was carried out on the cells by applying a voltage of 30 mV for 90 min. The data acquisition at the polarization starts (close to time 0) and upon the first 300 s was performed by recording 1 point each 0.05 s, and the maximum current (I_0) was obtained at the time 0.05 s after starting. The data acquisition near by the steady state upon polarization was performed by recording 1 point each 10 s, and the minimum current (I_{ss}) was obtained after 90 min.

The initial and steady-state resistances were determined through nonlinear least squares (NLLS) fit of the impedance spectra by Boukamp package [180,181]. The transference numbers were measured at least three times. The estimated errors on current and resistance were lower than 1% and 5%, and the chi-square was lower than 10^{-4} . Accordingly, the estimated error associated with t^+ is 10%.

The ESW of the electrolyte solutions was assessed in T-type cells by voltammetry measurements at a scan rate of 0.1 mV s^{-1} . The high-potential range was studied through LSV employing carbon-coated aluminum as the working electrode. The low-potential range was

studied through CV within 0.01 – 2 V vs. Li⁺/Li using carbon-coated copper as the working electrode.

The characteristics of the Li/electrolyte interphase were investigated by coupling EIS and galvanostatic cycling measurements on symmetrical Li/Li coin-cells. The Li/electrolyte interphase resistance upon cell storage was tested via EIS measurements. A frequency range of 500 kHz to 1 Hz was applied with an alternate voltage signal (amplitude of 10 mV). The spectra were analyzed by the NLLS method through the Boukamp package. Lithium stripping/deposition galvanostatic measurements were done using a current density of 0.1 mA cm⁻² and a step time of 1 h.

Chronoamperometry and all the EIS measurements were made through VersaSTAT MC (AMETEK, Princeton Applied Research) potentiostat.

5.4.4 Galvanostatic cycling tests

Electrodes having diameters of 14 and 10 mm were assembled into CR2032 coin-cells (MTI Corporation) and three-electrodes T-type cells, respectively, in an Ar-filled glovebox (MBraun, O₂ and H₂O content below 1 ppm). Lithium metal disks were employed as counter and reference electrodes, and glass fiber (Whatman®, GF/D) was used as separator soaked by the electrolyte solution. The electrolyte solutions were studied in Li/LFP cells by galvanostatic cycling through a MACCOR Series 4000 battery test system. The charge/discharge measurements were performed at a C/3 rate (1C = 170 mA g⁻¹) between 2.8 and 3.9 V.

Chapter 6 Towards a high-performance lithium-metal battery with glyme solution

6.1 Introduction

This chapter is based on the content presented in *ChemElectroChem*, 2020, 7, 2376 –2388, entitled “Towards a High-Performance Lithium-Metal Battery with Glyme Solution and an Olivine Cathode”, copyright (2020) Chemistry Europe.

In **Chapter 5**, six electrolyte solutions respectively formed by dissolving LiFSI, LiTFSI, and LiBETI in DEGDME and TREGDME have been fully investigated. The electrolyte composition had a remarkable effect on the cell performances and indicated the LiTFSI salt in glyme solutions as the most adequate formulations for possible applications.

It is widely demonstrated that LiNO₃-containing electrolytes may form a uniform and stable anode passivation layer, which can mitigate the parasitic reactions in the cell and limit the lithium dendrite growth [154,155].

In this chapter, we explore the effect of the addition of LiNO₃ to the above electrolytes in terms of cell performances, cycle life, and electrode/electrolyte interphase stability. In particular, the work sheds light on the different characteristics of various compositions for a possible application in Li/LFP batteries with expected enhanced safety compared to the lithium cells using conventional EC/DME solutions.

6.2 Results and discussion

The charge transport ability has been evaluated by coupling ionic conductivity (**Figure 6.1a**, main panel), and lithium transference number (t^+ , **Figure 6.1a**, panel inset) measurements. The

electrolytes display an ionic conductivity ranging from 10^{-3} to 10^{-2} S cm $^{-1}$ within the temperature window from 0 to 80 °C, which is a promising response for a possible application in lithium batteries [172]. The conductivity values may be interpolated by the Vogel-Tamman-Fulcher (VTF) equation (see **Figure 6.1a**) with squared correlation factors (R^2) higher than 0.99. The estimated t^+ values, ranging from 0.60 ± 0.06 (electrolyte D) to 0.74 ± 0.07 (electrolyte B), suggest high mobility of the Li^+ for all the investigated solutions. Therefore, electrolyte B shows the best characteristics in terms of both ionic conductivity (within the range from 6×10^{-3} to 8×10^{-3} S cm $^{-1}$) and Li^+ transference number (i.e., 0.74 ± 0.07).

The ESW of each electrolyte solution has been identified by LSV and CV on two different cells in the high and low voltage regions, respectively (see **Figure 6.1b**). The experimental data of **Figure 6.1b** indicate a current flow lower than $30 \mu\text{A cm}^{-2}$ at 4.3 V vs. Li^+/Li for all the solutions, thus suggesting the possible use in lithium cells with LiFePO_4 operating at 3.45 V [183]. Furthermore, the figure inset indicates higher oxidative stability for electrolytes B and E, i.e., using the LiTFSI salts, which fully decompose at a potential up to 4.5 V vs. Li^+/Li . Besides, Al corrosion via dissolution into the electrolyte above 3.5 V vs. Li^+/Li cannot be excluded [184]. Very weak peaks, with current flow below $20 \mu\text{A cm}^{-2}$ are observed from 3.5 to 4.1 V vs. Li^+/Li , thereby suggesting that the current collector is relatively stable in the solutions within the potential window of LFP.

As for the low-voltage region, the first cathodic CV scan shows the expected electro-reduction of LiNO_3 , which contributes to the SEI formation [150] occurring by a strong current signal within 1.7–1.4 V vs. Li^+/Li . **Figure 6.1b** inset reveals voltammetry peaks at about 1.45, 1.52, and 1.57 V vs. Li^+/Li for electrolytes A, B, and C, i.e., using diglyme, and at about 1.49, 1.47, and 1.47 V vs. Li^+/Li for electrolytes D, E, and F, i.e., using triglyme. An additional reduction likely affecting the SEI composition [185] is observed at a lower voltage, along with Li^+ insertion into the carbon electrode and lithium plating, which are partially reversible upon the subsequent oxidation scan [179].

Figure 6.1c indicates a relatively stable trend with R_i values lower than 45Ω (i.e., about $30 \Omega\text{cm}^{-2}$) during 1 month of storage. The diglyme-based electrolytes exhibit initial SEI

resistances of about $29.1 \pm 0.1 \Omega$ (A), $27.7 \pm 0.1 \Omega$ (B), and $22.9 \pm 0.1 \Omega$ (C), which slightly vary during the first day. Afterwards, the R_i values rise to $31.9 \pm 0.2 \Omega$ (A), $27.7 \pm 0.1 \Omega$ (B), and $35.7 \pm 0.2 \Omega$ (C) after 9 days and maintain a stable trend upon 31 days of cell storage with only a minor increase. The triglyme-based solutions show initial resistances of $40.6 \pm 0.1 \Omega$ (D), $27.7 \pm 0.07 \Omega$, and (E) $25.9 \pm 0.09 \Omega$ (F). As for electrolyte D, R_i drops to about $34.1 \pm 0.1 \Omega$ after 3 days, then slowly increases to $38.0 \pm 0.1 \Omega$ after 9 days and to $42.6 \pm 0.1 \Omega$ after 30 days, while electrolyte F exhibits values constantly rising to 38Ω after 20 days. Besides, electrolyte E shows an initial increase to about 31Ω throughout the first 7 days, followed by a stabilization and a slight fluctuation.

Figure 6.1c shows a similar decreasing trend of R_i during the first days for electrolytes A and D, i.e., the solutions containing LiFSI, followed by a slight increase. However, R_i in **Figure 6.1c** fluctuates during cell aging in a relatively narrow range (about 10Ω) for all the investigated formulations, leading to maximum values below 45Ω , which suggest full compatibility with the lithium-metal anode. Therefore, LiNO_3 leads to a marked improvement of the SEI according to the well-known beneficial effects [170], as clearly indicated by a comparison of the data of **Figure 6.1c** with previous results on similar electrolytes without additives [185].

The lithium stripping/deposition test in a symmetrical cell (**Figure 6.1d**) elucidates the stability of the solutions under the dynamic condition and evidences their compatibility with the lithium-metal battery [145], which is demonstrated by low overvoltage values (below 10 mV for electrolyte A, and below 13 mV for all the other electrolytes) during 25 days. Again, the data reveal a significant improvement compared with the LiNO_3 -free electrolytes [185], further demonstrating the crucial role of the additive as a stabilizing agent to enhance lithium-cell performance. Indeed, **Figure 6.1** shows evidence of efficient use of the electrolytes in lithium-metal batteries.

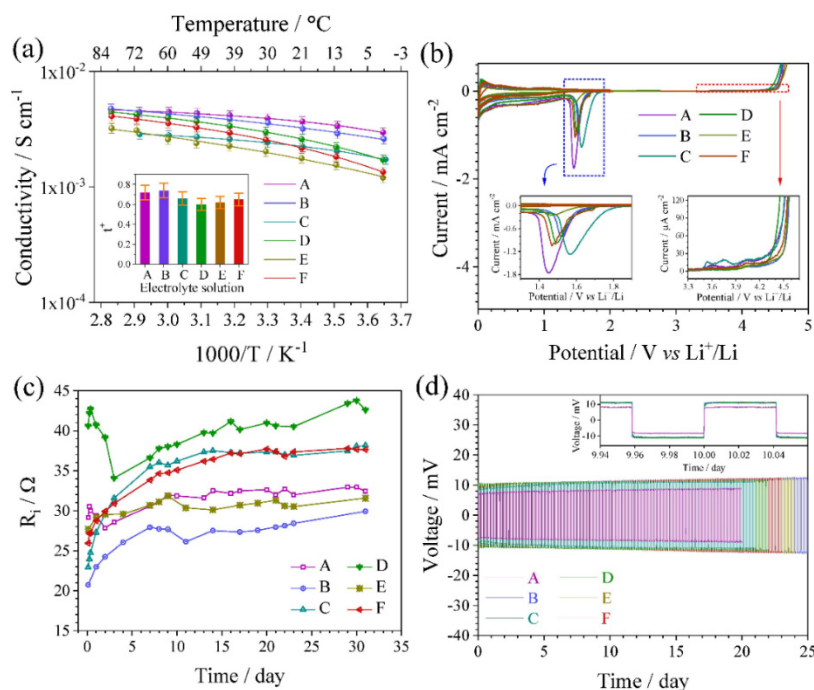


Figure 6.1 (a) Temperature dependence of ionic conductivity as obtained by EIS. Inset: lithium transference number (t^+) at 25 °C. (b) Electrochemical stability window assessed by LSV (high-potential region) and CV (low-potential region) at 0.1 mV s⁻¹ of three-electrode lithium cells using carbon-coated Al and Cu working electrodes, respectively, with magnifications in the inset. (c) Time evolution of the lithium/electrolyte interphase resistance as determined by EIS measurements on symmetrical Li/Li cells. (d) Voltage profiles of lithium deposition/stripping tests at a constant current of 0.1 mA cm⁻² on Li/Li symmetrical cells (step time: 1h) with magnification in inset.

The electrochemical behavior of the solutions is additionally evaluated by assembling and cycling at a C/3 rate (1 C = 170 mA g⁻¹) Li/LFP batteries. **Figure 6.2** reports the voltage profiles (panels a, c, e) and the trends of capacity and coulombic efficiency (panels b, d, f) of the cells using the diglyme-based electrolytes (see panels a–b, c–d, and e–f for electrolytes A, B, and C, respectively). The voltage curves reveal the typical flat plateau of LFP centered at 3.5 V with negligible irreversible capacity after the formation of adequate electrode/electrolyte interphases and possible structural rearrangements in the cathode during the 1st cycle [186]. The cell using electrolyte A shows an initial polarization of about 160 mV, which gradually increases to 220 mV throughout the measurement (see **Figure 6.2a**). It is therefore worth noting that the final

segment of the charge/discharge curves at the 150th and 200th cycles shows a sloping profile of a diffusion-limited process, thereby suggesting a possible deterioration of the electrode/electrolyte interphases [77]. Such a change of the voltage profile after 100 cycles (see **Figure 6.2a**) adversely affects the energy efficiency and leads to a slight capacity fading from about 155 mAh g⁻¹ at the 100th cycle to 144 mAh g⁻¹ at the 200th cycle despite coulombic efficiency values above 99% (see **Figure 6.2b**)

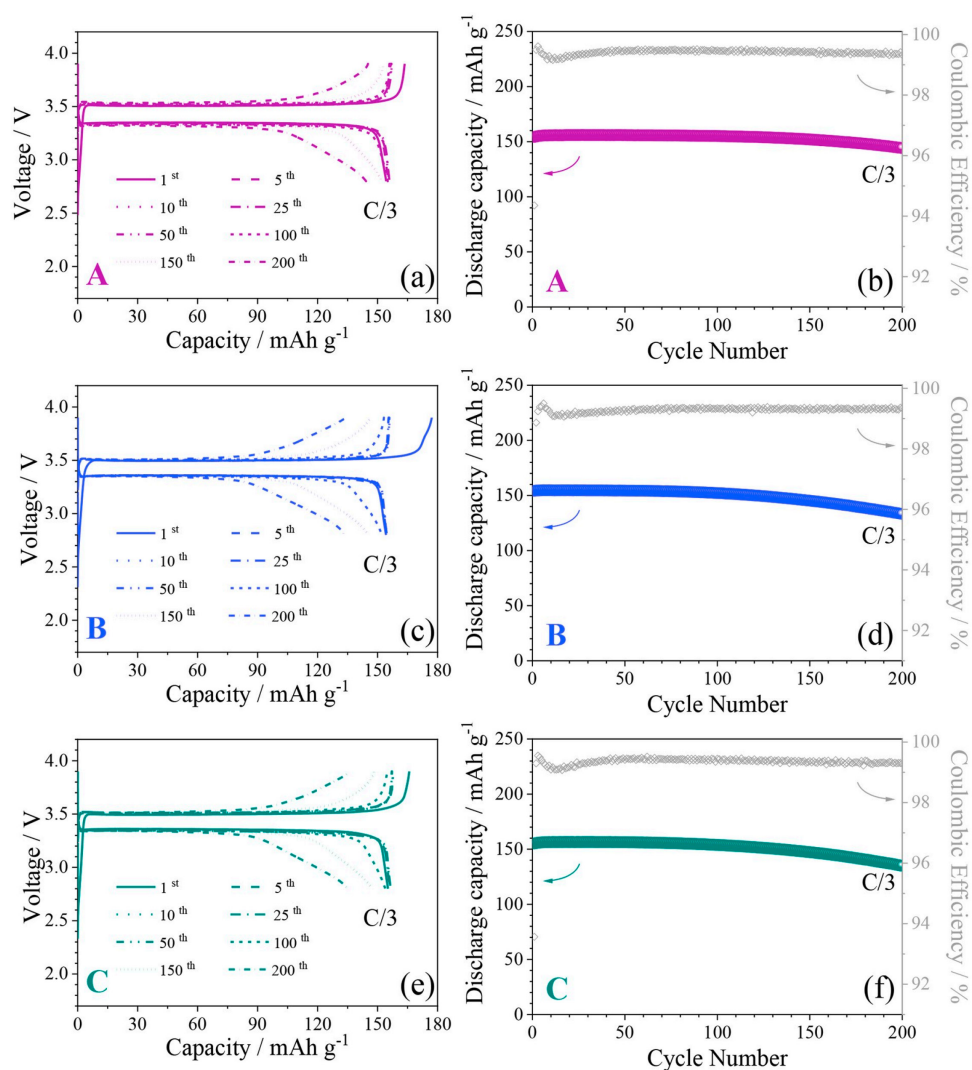


Figure 6.2 Cycling performances over 200 cycles of Li/LFP cells using electrolytes (a–b) A, (c–d) B and (e–f) C at a rate of C/3 in terms of (a, c, e) voltage profiles of the 1st, 5th, 10th, 25th, 50th, 100th, 150th, 200th cycles and (b, d, f) discharge capacity with coulombic efficiency (left y-axis and right- y-axis, respectively).

The cells employing electrolytes B and C exhibit a similar galvanostatic response but slightly more pronounced capacity fading (see **Figure 6.2c–f**). Thus, a gradual interphase deterioration affecting the final segment of the profiles is observed in both cells from the 100th cycle (see **Figure 6.2c** and **e**) in spite of lower polarization values (140 mV for electrolyte B and 130 mV increasing to 170 mV for electrolyte C). The cells deliver reversible capacities of 155 (B, **Figure 6.2d**) and 156 mAh g⁻¹ (C, **Figure 6.2f**), which decrease to 152 and 154 mAh g⁻¹ after 100 cycles and to 133 and 135 mAh g⁻¹ after 200 cycles, respectively. As observed for electrolyte A, panels **d** and **f** of **Figure 6.2** show coulombic efficiency values permanently above 99% after a stabilization during the initial cycles.

Interestingly, the increase of the glyme chain-length from DEGDME to TREGDME ensures a significant enhancement of the electrolyte behavior in the cell with the same amount of LiNO₃ (0.4 mol kg⁻¹). The remarkable effect of the solvent allows for the TREGDME-based cells stable voltage profiles, which overlap during cycling without any clear sign of degradation of the electrode/electrolyte interphases (see panels **a**, **c**, and **e** of **Figure 6.3** for electrolytes D, E, and F, respectively). Accordingly, the flat curves reflect the signature of the biphasic electrochemical process of LFP [187], characterized by a constant voltage during charge and discharge with a low polarization ranging from 140 to 170 mV, slightly increasing after 200 cycles, which suggests fast charge transfer and outstanding cell stability. The batteries deliver reversible capacities of 153 (electrolyte D) and 154 mAh g⁻¹ (electrolyte E and F) after activation during the first 5 cycles [186], without any decay over 200 cycles, and Coulombic efficiencies permanently within the range from 99.6 to 99.8% (see panels **b**, **d**, and **f** of **Figure 6.3** for electrolytes D, E, and F, respectively). Therefore, the addition of LiNO₃ to the electrolytes can effectively enhance cell behavior due to beneficial electrode-passivation properties, leading to remarkable cell stability [155]. Instead, the triglyme-based electrolytes with the present formulation exhibit excellent compatibility with the electrode components, as indeed demonstrated by outstanding cycling performances over 200 cycles. In particular, electrolyte E, i.e., using LiTFSI, shows the smallest lithium/electrolyte interphase resistance according to **Figure 6.1c** and the widest oxidative window according to **Figure 6.1b**.

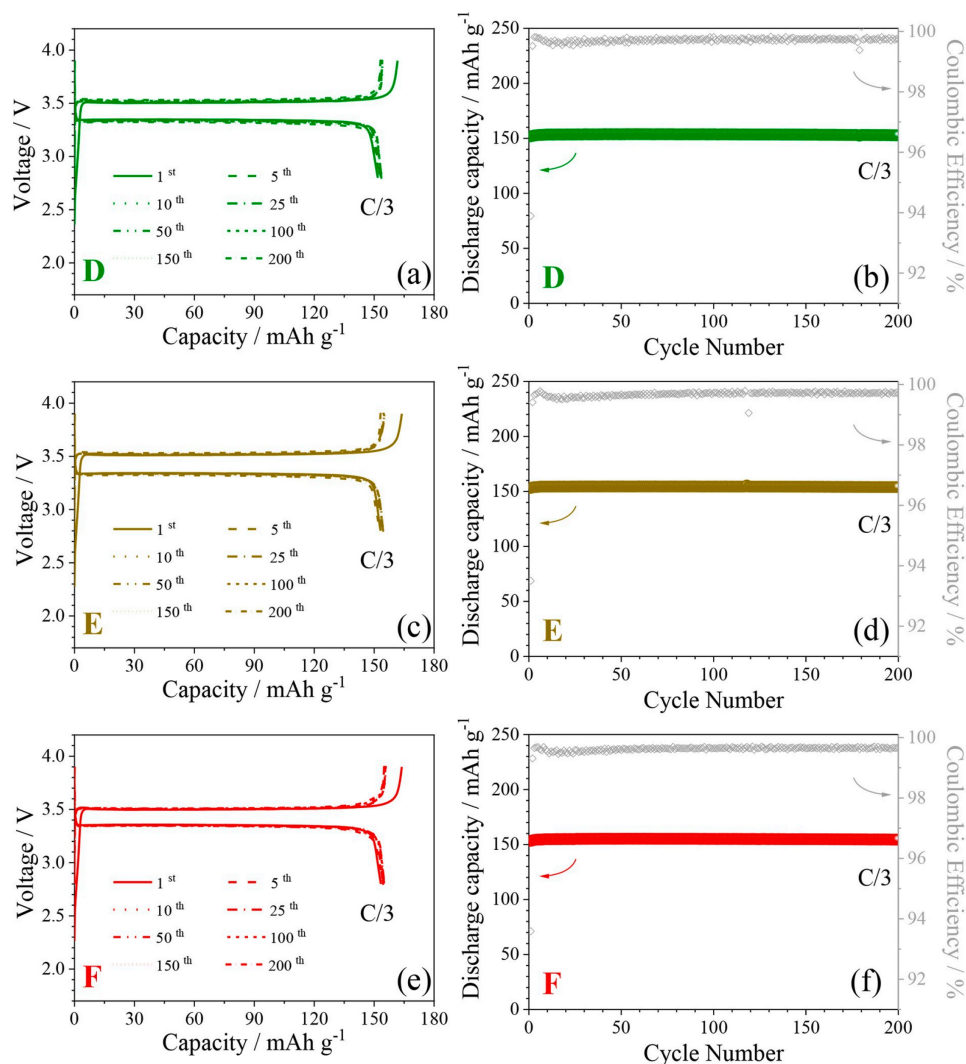


Figure 6.3 Cycling performances over 200 cycles of Li/LFP cells using electrolytes (a–b) D, (c–d) E and (e–f) F solutions at a rate of C/3 in terms of (a, c, e) voltage profiles of the 1st, 5th, 10th, 25th, 50th, 100th, 150th, 200th cycles and (b, d, f) discharge capacity with coulombic efficiency (left y-axis and right- y-axis, respectively).

All the cells of **Figures 6.2** and **6.3** exhibit the typical flat voltage plateau indicating a Li^+ (de)insertion in a biphasic regime before the 100th cycle. In addition, the voltage curves of the subsequent cycles reveal that the cell response is mostly affected by the glyme solvent rather than by the salt, thereby suggesting a possible effect of the ether-chain length on the passivation layer over the positive and negative electrodes. Thus, the DEGDME-containing cells show two main domains in the voltage plateau after the 100th cycle, namely (i) an initial biphasic regime

characterized by a rather constant voltage (initial section of charge and discharge) and (ii) a final regime presenting a sloping curve (the final section of charge and discharge), while the TREGDME-containing ones permanently exhibit mainly the typical two-phase response (compare **Figure 6.2a, c, and e** with **Figure 6.3a, c, and e**). The final domain of **Figure 6.2a, c, and e** might indicate a Li^+ (de)insertion in the olivine cathode by single-phase, diffusion-limited kinetics [188], as observed in LFP nanomaterials [187].

However, a possible increase of the cell resistance due to excessive growth of the passivation layers on anode and cathode during cycling, likewise leading to a decrease of the Li^+ concentration in the electrolyte, cannot be ruled out [77]. Furthermore, a sloping profile may arise from a gradual microstructural reorganization occurring in the cathode during cycling in terms of crystallite size distribution and surface free energies of the lithiated and the delithiated phases, possibly producing a change of the biphasic potential, rather than from a different insertion mechanism [189]. In this respect, a full elucidation of the observed cell responses is not straightforward. Therefore, additional EIS measurements on the positive and negative electrodes, and *ex situ* SEM and XRD analyses of the LFP cathode have been performed.

The EIS investigation on the Li/LFP cells has been carried out by employing a three-electrode configuration that can reveal the actual contribution of cathode and anode interphases on the overall cell resistance (**Figures 6.4**). Thus, impedance spectra of the LFP and Li electrodes have been recorded at the OCV and after 1, 10, 100, and 200 cycles (see the related Nyquist plots of main panels and insets of **Figure 6.4**, respectively). The analysis suggests a remarkable increase of the overall LFP/electrolyte interphase resistance (ΣR_i) at the 200th cycle for the cells using solutions A, B, and C (see **Figure 6.4a–c**). The lithium/electrolyte interphase resistance (**Figure 6.4a–c** insets) fluctuates below 120 Ω , indicating that the evolution of the SEI over the anode during 200 cycles does not significantly hinder the Li^+ diffusion [190]. As for solutions D, E, and F, EIS indicates rather stable interphases over both LFP and Li, with ΣR_i values permanently below 150 Ω during 200 cycles. Notably, the results of **Figure 6.4** indicate an excellent stability of the lithium/electrolyte interphase both under static and dynamic conditions for all the investigated formulations, although particular glyme-based compositions may be

poorly compatible with lithium metal [191]. Therefore, the significant increase in cathode/electrolyte interphase resistance for the DEGDMC containing cells might partially account for the capacity fading observed in **Figure 6.2**.

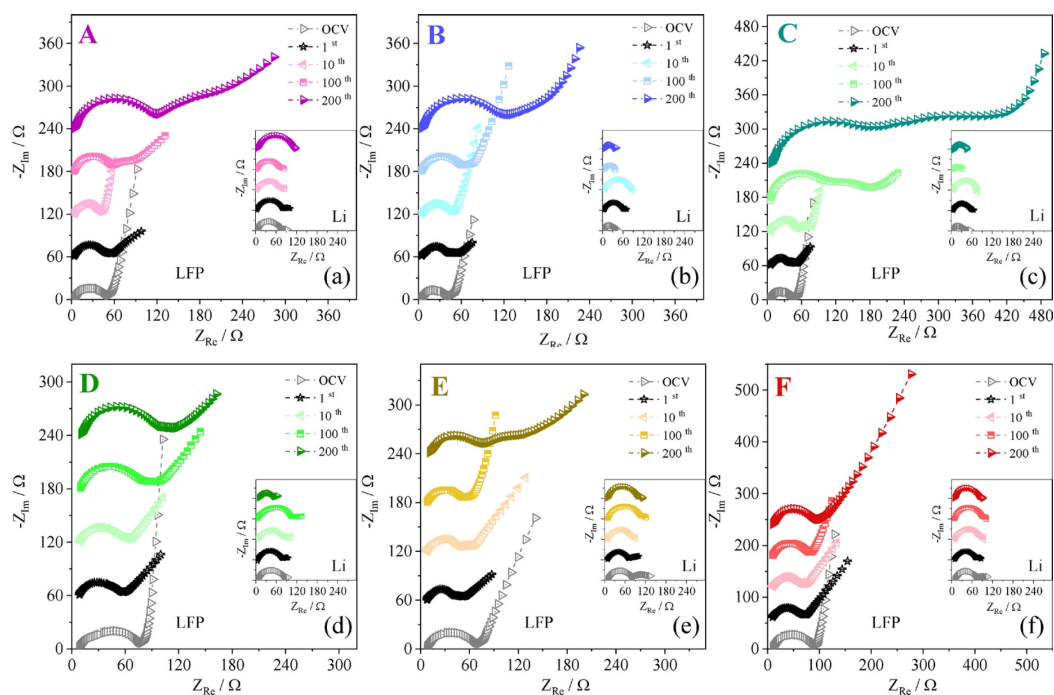


Figure 6.4 Nyquist plots of EIS measurements of the (main panels) positive LFP and (inset) negative Li electrodes performed in three-electrode T-type cells, using lithium metal as the reference electrode and solutions (a) A, (b) B, (c) C, (d) D, (e) E, and (f) F as the electrolyte; spectra recorded at the OCV and after the 1st, 10th, 100th, and 200th cycles at a 2C rate.

SEM images and XRD patterns of the LFP electrodes before and after 200 cycles in the lithium cells are shown in **Figure 6.5** (pristine LFP) and **Figure 6.6** (LFP after cycling). The LFP material is formed by spherical micrometric agglomerates of LiFePO₄ nanometric primary particles, as shown in **Figure 6.5**. Such a tailored morphology ensures a high tap density and excellent charge/discharge performances in lithium cells.

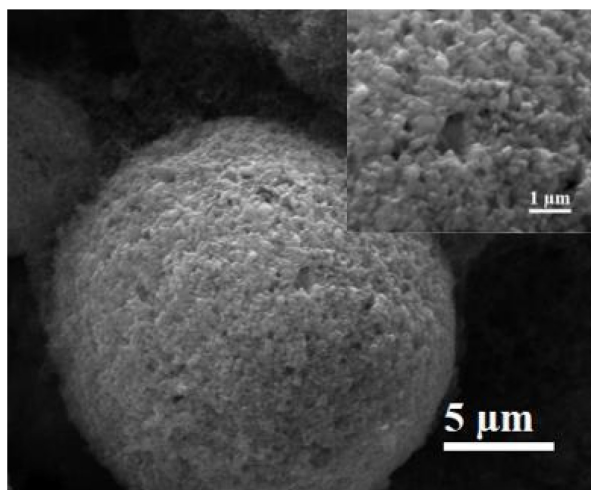


Figure 6.5 SEM images at two different magnifications of pristine LFP.

As widely discussed in the manuscript and shown in **Figure 6.6**, the electrolyte formulation may adversely affect the microstructure of the cathode material leading to a capacity decay during long term cycling. SEM suggests the deposition of a passivation layer over the spherical agglomerates of primary LFP particles along with a minor rearrangement occurring in the spherulites, possibly due to structural modifications. Such phenomena are particularly relevant for electrolytes B and C and partially in agreement with the EIS response of the positive electrode (**Figures 6.4**).

XRD reveals an increase in the full width at half maximum (FWHM) for the olivine during cycling (see **Figure 6.6g** and **h**), which might be associated with the change in voltage profile slope for the DEGDME-containing cells (see **Figure 6.2a, c, and e**). Indeed, a significant decrease in the average crystallite size typically observed as a broadening of the diffraction peaks may affect the voltage profile by changing either the local biphasic voltage or the insertion mechanism from a two-phase transformation to a single-phase, diffusion-limited process.

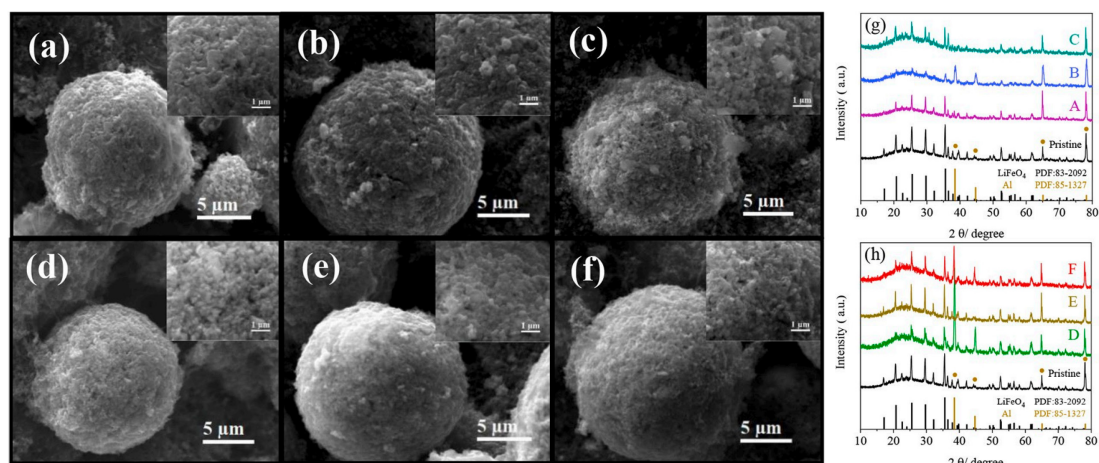


Figure 6.6 (a–f) *Ex situ* SEM images of the LFP electrodes recovered from the lithium cells analyzed, disassembled after 200 cycles at a rate of 2C. Cells using electrolytes **(a)** A, **(b)** B, **(c)** C, **(d)** D, **(e)** E, and **(f)** F. **(g–h)** XRD patterns of the same LFP electrodes materials (using electrolyte **(g)** A, B, and C, and electrolytes **(h)** D, E, and F) and of a pristine LFP electrode.

A detailed study of the electrolyte E (LiTFSI-LiNO₃-TREGDME) was carried out to assess the Li/LFP cell behavior upon long-term cycling by coupling galvanostatic charge/discharge and impedance measurements. **Figure 6.7a** reports the cycling response of the cell at 1C, 2C, and 5C rates as a trend of discharge capacity and coulombic efficiency. After the initial electrochemical activation of the LFP cathode, the battery delivers capacities of about 147 mAh g⁻¹ at 1C and 138 mAh g⁻¹ at 2C and 5C rates, slightly decreasing to 144, 137, and 131 mAh g⁻¹ at the 200th cycle. Coulombic efficiency values approaching 100% indicate reversible reaction with low electrolyte decomposition rate and suggest stable electrode/electrolyte interphases. This trend appears remarkable, particularly considering the relatively high current rates used for cycling (that is, 1C, 2C, and 5C). However, the discharge capacity decreases to values within the range from 103 and 106 mAh g⁻¹ at the 500th cycle. Hence, the partial fading likely suggests possible effects of the cycling conditions on the phenomena occurring in the cell [192]. The stability of electrode/electrolyte interphases at both the anode and the cathode sides may play a crucial role in the cell response upon prolonged charge/discharge cycles [193].

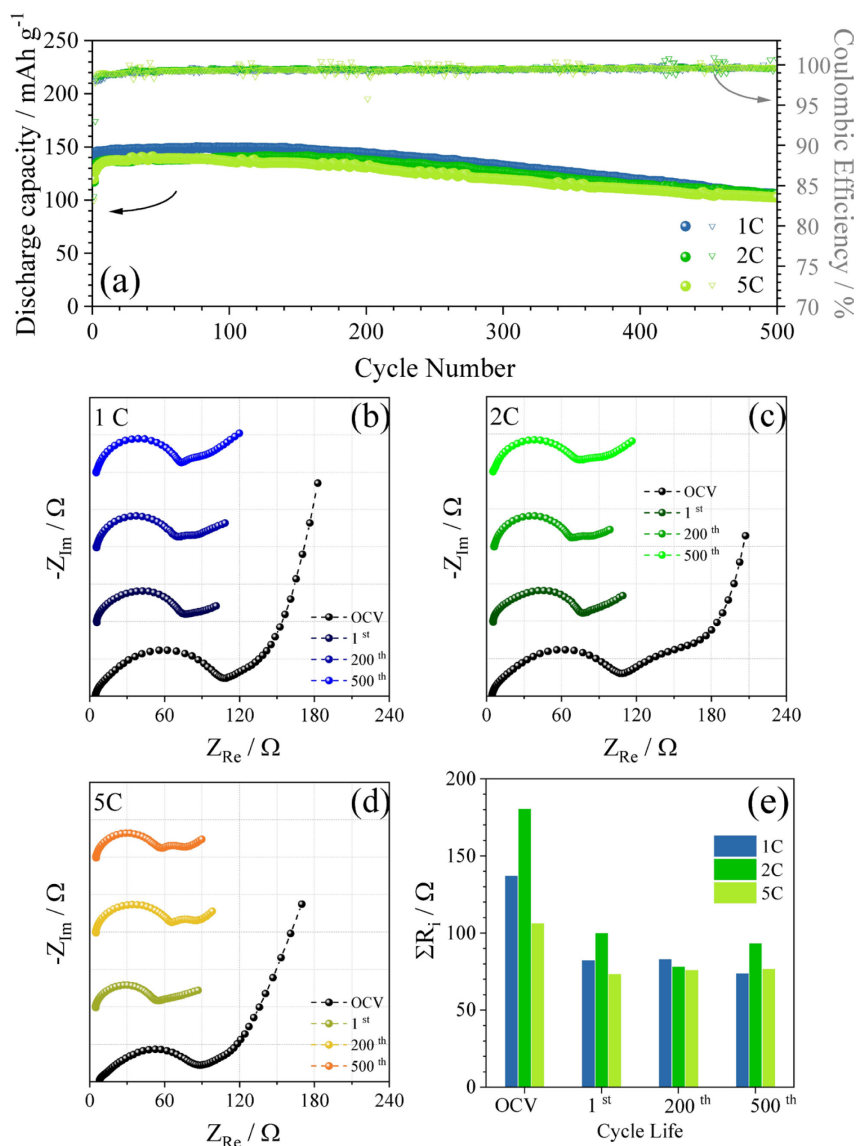


Figure 6.7 (a) Galvanostatic cycling trend in terms of discharge capacity with coulombic efficiency (left y-axis and right- y-axis, respectively) over 500 cycles of a Li/LFP cell using electrolyte E (LiTFSI-LiNO₃-TREGDME) at 1C, 2C and 5C rates. (b, c, d) Nyquist plots of EIS measurements performed on the Li/LFP cell using electrolyte E during the cycling tests at (b) 1C, (c) 2C, and (d) 5C rates. Impedance spectra (e) were carried out at OCV, after the 1st, 200th, and 500th cycle.

EIS measurements carried out during cycling may elaborate the cell resistance trend throughout the tests. Thus, panels b, c, and d of Figure 6.7 display the evolution of the related Nyquist plots at 1C, 2C, and 5C rates, respectively. Each spectrum consists of overlapped high to-middle frequency semicircles and a middle-to-low frequency response, which substantially modifies from the OCV to the following cycles. These impedance features are likely attributed to the

passivation films and charge transfer processes at the electrode/electrolyte interphases as well as to Li^+ diffusion phenomena and geometrical capacitance [194]. As mentioned, EIS reveals a remarkable change in the low-frequency region from a quasi-capacitive to a diffusion-type response after the 1st cycle, along with a significant decrease of the overall interphase resistance ($\sum R_i$, see **Figure 6.4e**). This drop may partially account for the electrochemical activation (an increase of capacity) observed during the very first cycles of the galvanostatic measurement (**Figure 6.7a**).

C rate	Cycle life	Equivalent Circuit	χ^2	$\sum R_i$ (Ω , $i = 1, 2, \dots, n$)
1C	OCV	$R_e(R_1Q_1)(R_2Q_2)(R_3Q_3)Q_g$	9.5×10^{-5}	140 ± 10
1C	1 cycle	$R_e(R_1Q_1)(R_2Q_2)(R_dQ_d)$	8.2×10^{-5}	82 ± 7
1C	200 cycles	$R_e(R_1Q_1)(R_2Q_2)(R_dQ_d)$	3.6×10^{-5}	83 ± 7
1C	500 cycles	$R_e(R_1Q_1)(R_2Q_2)(R_dQ_d)$	2.4×10^{-5}	74 ± 2
2C	OCV	$R_e(R_1Q_1)(R_2Q_2)(R_3Q_3)Q_g$	3.1×10^{-5}	181 ± 7
2C	1 cycle	$R_e(R_1Q_1)(R_2Q_2)(R_dQ_d)$	3.9×10^{-5}	100 ± 20
2C	200 cycles	$R_e(R_1Q_1)(R_2Q_2)(R_dQ_d)$	2.6×10^{-5}	78 ± 6
2C	500 cycles	$R_e(R_1Q_1)(R_2Q_2)(R_dQ_d)$	2.6×10^{-5}	90 ± 10
5C	OCV	$R_e(R_1Q_1)(R_2Q_2)(R_3Q_3)Q_g$	7.1×10^{-5}	110 ± 10
5C	1 cycle	$R_e(R_1Q_1)(R_2Q_2)(R_dQ_d)$	1.3×10^{-4}	70 ± 10
5C	200 cycles	$R_e(R_1Q_1)(R_2Q_2)(R_3Q_3)(R_dQ_d)$	9.8×10^{-6}	80 ± 10
5C	500 cycles	$R_e(R_1Q_1)(R_2Q_2)(R_dQ_d)$	6.4×10^{-5}	77 ± 4

Table 6.1 NLLS analysis of EIS data collected throughout galvanostatic cycling tests at 1C, 2C, and 5C rates of electrolyte E (LiTFSI-LiNO₃-TREGDME) in a Li/LFP cell. In detail: C rate, cycle life, equivalent circuit, χ^2 , and sum of electrode/electrolyte interphase resistances ($\sum R_i$, Ω , $i = 1, 2, \dots, n$) at high-medium frequency.

However, the NLLS analysis suggests a hindering to the Li^+ diffusion over the following cycles with relatively stable high-to-middle frequency resistance values. Although the slow Li^+ diffusion might partially reflect the capacity fade trend at the various rates, the favorable characteristics of the interphases at the anode and the cathode sides (**Figure 6.7e** and **Table 6.1**)

ensure a promising cell behavior over 500 cycles (**Figure 6.7a**) for a possible application of the glyme-based electrolyte. Relevantly, the absence of any dendrite evolution, the relatively high delivered capacity (i.e., over 100 mAh g⁻¹) at elevated current rate of 5C, and capacity retention exceeding 70 % after 500 cycles are considered remarkable results which may conduce to the development of a rechargeable lithium-metal battery operating at room temperature.

6.3 Conclusion

The six solutions exhibited room-temperature ionic conductivity within 10⁻³ and 10⁻² S cm⁻¹ and lithium transference numbers higher than 0.6. Cyclic voltammetry suggested that the LiNO₃ reduction between 1.7 and 1.4 V vs. Li⁺/Li may lead to a stable lithium/electrolyte interphase with low resistance (ranging from 20 to 30 Ω) and suitable lithium plating/stripping for prolonged cycling. Oxidative stability over 4.3 V vs. Li⁺/Li ensured promising electrochemical performances in Li/LFP cells with a reversible capacity of the order of 150 mAh g⁻¹ at a C/3 rate and coulombic efficiency above 99% upon 200 cycles. However, the diglyme-based cells showed a capacity fading to about 140 (for LiFSI) and 130 mAh g⁻¹ (LiTFSI and LiBETI), while the triglyme-based ones exhibit an outstanding performance without any evidence of degradation after 200 cycles and coulombic efficiency values above 99.6%. Notably, a change in voltage profile slope occurring in the cells using the diglyme may be directly associated with the observed capacity fading and a concurrent increase of the cathode/electrolyte interphase resistance.

Indeed, EIS and SEM measurement suggested the precipitation of a passivation layer on the positive electrode, while the SEI over the lithium-metal anode appears to be relatively stable and suitably permeable to the Li⁺ ions. Moreover, cycling with diglyme possibly leads to a decrease in the average crystallite size of the olivine phase, as suggested by *ex situ* XRD, and minor rearrangements of the primary particles forming the LFP spherulites.

Among the various electrolyte formulations, the one using triglyme, LiTFSI, and LiNO₃ was selected as the most promising combination. Therefore, EIS measurements throughout galvanostatic charge/discharge tests for 500 cycles indicate a capacity of about 150 mAh g⁻¹ at 1C, and 140 mAh g⁻¹ at 2C and 5C rates, which decrease to values within 103 and 106 mAh g⁻¹, as well as relatively stable SEI and charge transfer resistance at medium-high frequency ascribed to coulombic efficiency values approaching 100%. These results suggested the possible applicability of glyme-based, LiNO₃-containing solutions in high-energy lithium-metal batteries.

6.4 Experimental section

Prior to electrolyte preparation, the salts and the solvents were dried under the same conditions as last Chapter 5. Table 6.2 reports in detail the electrolyte compositions and sample acronyms (that is, A–F, respectively).

Salt 01	Salt 02	Solvent	Acronym
LiFSI; 1 mol kg ⁻¹	LiNO ₃ ; 0.4 mol kg ⁻¹	DEGDME	(A) LiFSI-LiNO ₃ -DEGDME
LiTFSI; 1 mol kg ⁻¹	LiNO ₃ ; 0.4 mol kg ⁻¹	DEGDME	(B) LiTFSI-LiNO ₃ -DEGDME
LiBETI; 1 mol kg ⁻¹	LiNO ₃ ; 0.4 mol kg ⁻¹	DEGDME	(C) LiBETI-LiNO ₃ -DEGDME
LiFSI, 1 mol kg ⁻¹	LiNO ₃ ; 0.4 mol kg ⁻¹	TREGDME	(D) LiFSI-LiNO ₃ -TREGDME
LiTFSI; 1 mol kg ⁻¹	LiNO ₃ ; 0.4 mol kg ⁻¹	TREGDME	(E) LiTFSI-LiNO ₃ -TREGDME
LiBETI; 1 mol kg ⁻¹	LiNO ₃ ; 0.4 mol kg ⁻¹	TREGDME	(F) LiBETI-LiNO ₃ -TREGDME

Table 6.2 Overview of all electrolyte solutions and corresponding sample acronyms (A–F).

6.4.1 Electrode preparation

Six electrolyte solutions were obtained by dissolving the LiFSI (Sigma-Aldrich), LiTFSI (Sigma-Aldrich), LiBETI (Sigma-Aldrich) salts either in $(\text{CH}_3\text{OCH}_2\text{CH}_2)_2\text{O}$ (DEGDME, Sigma-Aldrich) or $\text{CH}_3(\text{OCH}_2\text{CH}_2)_3\text{OCH}_3$ (TREGDME, Sigma-Aldrich) solvents respectively, by using a concentration of 1 mol kg^{-1} with respect to the solvent. LiNO_3 was added to the solutions with a concentration of 0.4 mol kg^{-1} with respect to the solvent.

6.4.2 Electrolyte characterization

The ionic conductivity of the electrolyte solutions was measured within the temperature range from 0 to 80 °C by EIS through a Princeton Applied Research Potentiostat/Galvanostat (PAR, VersaSTAT MC), employing an amplitude of 10 mV within the frequency range of 500 kHz to 10 Hz. EIS was performed on symmetric stainless steel/electrolyte/stainless steel CR2032 coin-cells, employing a Teflon separator to fix the cell constant. Each conductivity value was measured every 10 °C during a cooling scan, after at least 6 h of cell conditioning at a constant temperature.

The t^+ number was calculated by the electrochemical method [174] through combining chronoamperometry and EIS tests. Accordingly, t^+ was calculated by following **Equation 6.1** [174]:

$$t^+ = \frac{I_{SS} (\Delta V - I_0 R_0)}{I_0 (\Delta V - I_{SS} R_{SS})} \quad (6.1)$$

where I_0 and I_{SS} refer to the initial and steady-state current values of the chronoamperometry measurements, respectively.

R_0 and R_{SS} represent the charge-transfer resistance between lithium and electrolyte before and after polarization, respectively.

ΔV is the applied voltage.

R_0 and R_{SS} were calculated by NLLS analysis of the impedance spectra [180], in which the Warburg region at low frequency has not been considered [195–197]. Chi-square parameters below 10^{-4} further confirm the reliability of the fitting method.

Chronoamperometry was carried out on two-electrode, T-type symmetrical Li/Li cells, by applying a 30 mV (ΔV) direct current (DC) pulse for 90 min, while EIS measurement was performed by using an AC signal (10 mV amplitude) over the frequency range of 500 kHz to 100 mHz. Chronoamperometry was performed by adjusting the time intervals for data collection in order to get accurate I_0 and I_{SS} values: intervals of 0.05 and 10 s point⁻¹ were used within the time ranges from 0 (initial state) to 300 s and from 300 s to 90 min (steady-state), respectively. The cells for t^+ employed 10 glass fiber separators to increase the electrolyte resistance and allow the accuracy of the method [185]. The experiment for t^+ determination was performed through a Princeton Applied Research Potentiostat/Galvanostat (PAR, VersaSTAT MC). The errors on t^+ were estimated to be within 0.06 and 0.07 (*i.e.*, 10%), taking into account errors on current and resistance lower than 1% and 5%. The transference numbers have been measured at least three times, taking care the very first current values as I_0 . In spite of the relatively low error on t^+ , possible further deviation due to intrinsic instability of the SEI during the measurement leading to an increase of the electrode/electrolyte interface resistance cannot be discounted.

The ESW was investigated by LSV and CV at a scan rate of 0.1 mV s⁻¹ in high-potential and low-potential range, respectively. The LSV measurement was conducted from the OCV (about 3 V) to about 5 V vs. Li⁺/Li, in which the lithium-metal disks were employed as the counter and reference electrodes along with the carbon-coated aluminum as the working electrode (three-electrode T-type configuration), while the CV test was performed within 0.01 – 2 V vs. Li⁺/Li potential range by using the same cell configuration with carbon-coated copper as the working electrode. The LSV and CV measurements were performed via a Princeton Applied Research Potentiostat/Galvanostat (PAR, VersaSTAT MC).

EIS measurements on symmetrical Li/Li coin-cells were performed upon aging for 31 days to study the stability of lithium/electrolyte interphase using an alternate voltage with 10 mV

amplitude within a frequency range of 500 kHz to 100 mHz, through SP-200 system a SP-200 Potentiostat (Bio-Logic Instrument). The EIS measurements have been repeated twice in order to confirm the trends of interphase resistance. The lithium stripping/deposition process was investigated by using symmetrical Li/Li coin-cells through a HJ1001SM8A system (Hokuto Denko Co.). A constant current of 0.1 mA cm^{-2} was applied to the cell by alternating charge and discharge steps of 60 min. All the measurements, except the EIS to estimate the ionic conductivity, were performed at 25 °C.

6.4.3 Tests in lithium-metal cell

The electrolyte solutions were studied in Li/LFP coin-cells by galvanostatic charge/discharge cycling at a C/3 rate ($1\text{C} = 170 \text{ mA g}^{-1}$) using a voltage range of 2.8 – 3.9 V. These experiments were carried out through a HJ1001SM8A system (Hokuto Denko Co.). EIS measurements were done on 3-electrode T-type Li/LFP cells using a lithium probe at the OCV as well as after 1st, 10th, 100th, and 200th cycles. These cells were cycled at a 2C rate upon 200 cycles using a voltage range of 2.8 – 4.0 V with a battery test system (MACCOR Series 4000) in a two-electrode configuration. EIS spectra was collected in the frequency range from 500 kHz to 20 mHz with an alternate voltage of 10 mV amplitude through a Potentiostat/Galvanostat (Princeton Applied Research, VersaSTAT MC). The data were analyzed through a NLLS fit procedure [180], using an equivalent circuit that takes into account a high-frequency response ascribed to the electrolyte resistance (R_e), a middle-high frequency response attributed to n interphase pseudocapacitances (Q_i) and resistances (R_i) reflecting the passivation layer, the charge transfer and the double layer ($i = 1, 2, \dots, n$), and a low-frequency pseudocapacitance attributed to the Warburg-type Li^+ diffusion [198].

Li/LFP coin-cells using the E solution (see **Table 6.2** for the acronym) were also tested at 1C, 2C, and 5C rates upon 500 cycles within the 2.8 – 3.9 V, 2.8 – 4.0 V, 2.0 – 4.1 V voltage ranges, respectively. EIS measurements were carried out during the 500-cycle tests at the OCV, 1st, 200th, and 500th cycles, respectively. The EIS measurements were recorded within the frequency range from 500 kHz to 100 mHz (an amplitude of 10 mV) through a Princeton Applied Research Potentiostat/Galvanostat (PAR, VersaSTAT MC). All the cycling tests and the related

EIS measurements were conducted at room temperature (25 °C). All the EIS spectra were analyzed by the Boukamp software according to an NLLS method [180].

6.4.4 *Ex Situ* analysis of the cycled LFP electrodes

Structure and morphology of the LFP electrodes before and after 200 cycles in the various lithium cells using glyme solutions were investigated by XRD and SEM. After cell disassembly, the cathodes were rinsed with DMC to remove possible residuals and dried under vacuum for about 3 min. XRD experiments were carried out through a Bruker D8-Advance instrument with Cu K α radiation. XRD patterns were recorded in the 2θ range from 10 to 80° with a step size of 0.02° and a rate of 10 s step⁻¹. SEM images were taken by a Zeiss EVO 40 microscope, equipped with a tungsten thermionic source.

Chapter 7 Electrochemical behavior of nanostructured NiO@C anode in a lithium-ion battery

7.1 Introduction

This chapter is based on the content presented in *Journal of Alloys and Compounds*, 844 (2020) 155365, entitled “Electrochemical behavior of nanostructured NiO@C anode in a lithium-ion battery using LiNi_{1/3}Co_{1/3}Mn_{1/3}O₂ cathode”, copyright (2020) Elsevier.

Nanosized metal oxides with chemical formula M_xO_y (where M is typically a transition metal) may reversibly react in lithium cells by a multi-electron conversion mechanism leading to the formation of M₀ nano-domains embedded into a Li₂O matrix [107]. In spite of the attractive capacity in lithium cells, the conversion reaction is characterized by massive microstructural rearrangements, mostly leading to substantial volume changes of the electrode material and large voltage hysteresis, which may adversely affect the reversibility and efficiency of the process [199]. Careful tuning of the morphological features of metal oxide-carbon composites and carbon-coated metal oxide electrodes is a crucial requirement to effectively enhance the conversion reaction whilst limiting possible parasitic processes [116].

Electrochemical studies suitably combining material optimization in terms of structure and morphology, investigation in half-cells, and full-cell demonstration are considered crucial for this class of materials [6]. However, only a few works investigated the actual behavior of NiO anodes in lithium-ion cells [97,200] despite the tremendous amount of literature on the conversion-anode performance in half-cell configuration [110,201,202], even though a detailed investigation in the full cell employing a conventional cathode, such as LiNi_{1/3}Co_{1/3}Mn_{1/3}O₂ (NCM), is considered to be essential to assess the actual applicability [203].

Within this research context, a NiO anode in a lithium-ion battery using the high-performance NCM layered cathode was studied. Structure, morphology, and composition of the NiO composite material are carefully controlled by a two-step method involving carbon precipitation on metal-oxide nanoparticles in a reducing environment followed by oxidation at moderate temperature. The Li-conversion process of the NiO electrode in the cell was characterized exhaustively, thereby revealing promising behavior for possible applications.

7.2 Results and discussion

The dry mixture of sucrose and NiO was under an argon flow heated at 120 °C for 10 h and subsequently heated at 600 °C, held at 600 °C for 3 h to obtain Ni@C (step 1). Afterwards, the samples were under a dry air flow heated at 380 °C for 48 h to get NiO@C (step 2). **Figure 7.1** depicts the sucrose addition to bare NiO followed by pyrolysis (step 1) and the subsequent mild oxidation of the Ni@C intermediate to form the NiO@C material (step 2).

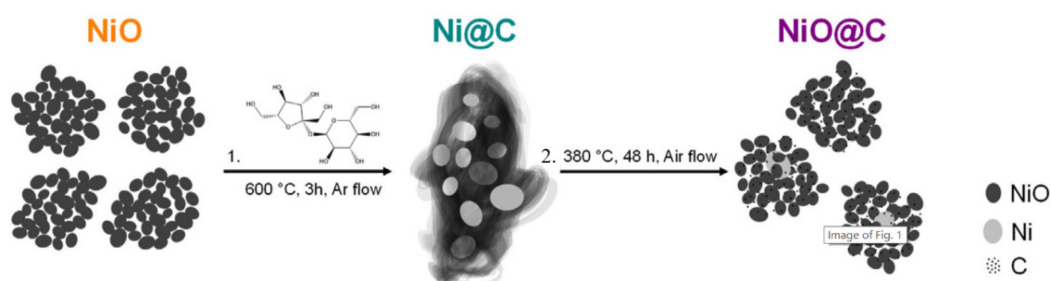


Figure 7.1 (step 1) sucrose precipitation on bare NiO followed by pyrolysis at 600 °C under an Ar flow; (step 2) mild oxidation of the Ni@C intermediate by heating at 380 °C under an air flow to form the NiO@C material.

The structural evolution of the composite electrode during the synthetic steps is reported in **Figure 7.2**. The indexed XRD patterns of NiO, Ni@C, and NiO@C reveal substantial phase changes promoted by the various treatments, with full reduction of the pristine NiO (ICSD # 9866) to Ni metal (ICSD # 260169) upon annealing in argon atmosphere (step 1), and its

subsequent oxidation after mild thermal treatment under air (step 2). Furthermore, the figure evidences that the final NiO@C sample contains NiO as the main phase along with traces of metallic nickel, thus suggesting partial oxidation during step 2 [204]. The absence of graphite peaks might suggest that the carbon coating produced by sucrose pyrolysis has low crystallinity. Therefore, the presence of the lowly crystalline carbon and traces of metallic Ni can suitably increase the electronic conductivity of the electrode material, thus possibly enhancing its electrochemical behavior in lithium cells [204].

A thermogravimetric analysis (TGA) under an air flow (**Figure 7.2b**) shows that the NiO@C powder undergoes weight change due to concomitant oxidation of C (weight loss) and Ni (weight increase), thereby leading to a final raise of 0.77% with respect to the initial mass. The Rietveld analysis of the XRD patterns of NiO@C indicates a Ni weight fraction of the crystalline domains of about 0.04 (see **Table 7.1**). Therefore, the carbon content in NiO@C was estimated below 4 wt.% considering the full oxidation of Ni to NiO upon the TGA scan.

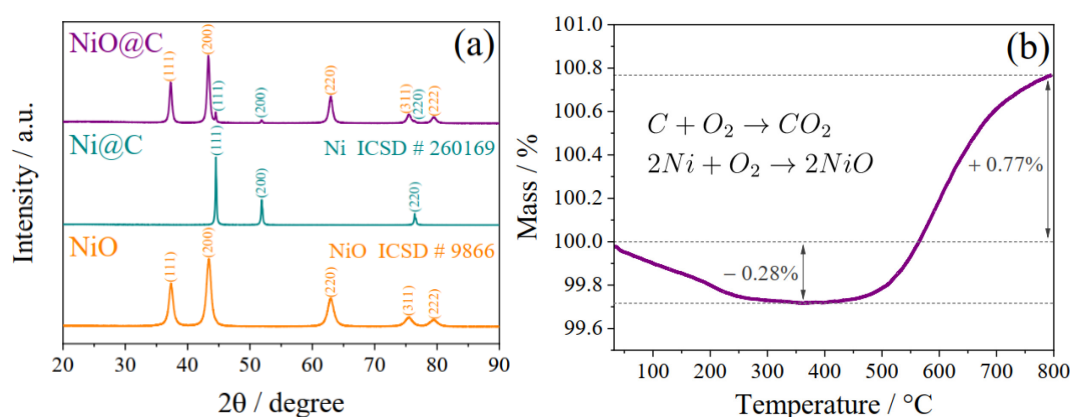


Figure 7.2 (a) XRD patterns of pristine NiO, Ni@C (after step 1), and NiO@C (after step 2). (b) TGA with a heating rate of $10\text{ }^\circ\text{C min}^{-1}$ between 30 and 800 $^\circ\text{C}$ under an air flow with rate of 50 mL min^{-1} (mass percent: left Y-axis), with suggested reactions occurring in the sample and mass percent variation in the inset.

A Rietveld refinement of the XRD patterns [205] indicates a Ni metal content in NiO@C of 4 wt.% with regard to the overall weight of the crystalline domains, and crystallite size of about 34 nm for the NiO phase and 140 nm for the Ni one (see **Table 7.1**). The patterns of both Ni

and NiO have been indexed to reference structures with cubic unit cell and space group (ICSD # 260169 and # 9866), despite the known rhombohedral distortion of the NiO crystal lattice at room temperature, which does not affect the X-ray reflections and, therefore, can be neglected in this study [46,47].

Phase	Space group	Weight fraction%	Crystallite size/Å	$a/\text{Å}$	$V/\text{Å}^3$	GOF(σ)	$R_{wp}\%$
NiO	$Fm\bar{3}m$ (No.225)	0.96±0.02	340.1±0.3	4.1794(1)	73.006(8)	1.6	9
Ni	$Fm\bar{3}m$ (No.225)	0.04±0.02	1400±100	3.5278(2)	43.905(7)		

Table 7.1 Results of Rietveld refinement for NiO@C in terms of space group, weight fraction, crystallite size, lattice parameter, unit cell volume of the crystalline NiO and Ni phases, along with good-of-fit (GOF, σ) parameter and weighted-profile R factor ($R_{wp}\%$).

The morphology and structure of the sample has been thoroughly studied using SEM, HRTEM, HAADF-STEM, and ZL-TEM imaging. Accordingly, SEM, HAADF-STEM, and ZL-EFTEM imaging of bare NiO (**Figure 7.3a, b, and c**, respectively) reveal aggregates with size ranging from 100 nm to 5 μm of nanometric grains (approximately between 5 and 20 nm), while elemental mapping (**Figure 7.3d and e**) and HRTEM analysis (**Figure 7.3f**) show the expected homogeneous distribution of Ni and O over the specimen and indicate a crystal structure in full agreement with the XRD patterns (ICSD # 9866), as clearly evidenced by the results of the fast Fourier transform (FFT, **Figure 7.3f** inset). Sucrose and NiO oxide reduction under an Ar flow (step 1) yields to Ni particles embedded in a carbon matrix, including residual O traces (below 5 wt.%). In detail, SEM, HAADF-STEM, and EFTEM analyses (**Figures 7.3g–k**) reveal nickel metal particles and clusters, mostly ranging from 10 nm to a few micrometers. HRTEM imaging of a Ni grain enclosed in a carbon shell indicates the crystalline cubic structure with the $Fm\bar{3}m$ space group (ICSD # 260169; **Figure 7.3l**) for the core and an amorphous nature for the outer layer. Hence, controlled oxidation of the Ni core (step 2) gives rise to a NiO@C material with similar morphological characteristic features to those of pristine NiO, in spite of expected slight

growth of the primary oxide grains forming the aggregates up to values approximately between 10 and 50 nm due to the thermal treatments (see the SEM, HAADF-STEM, and ZLTEM images of **Figure 7.3m, n, and o**). Moreover, EFTEM elemental mapping and HRTEM imaging (**Figure 7.3p–r**) suggest partial segregation of amorphous carbon and NiO oxide aggregates with cubic crystal structure with the $Fm\bar{3}m$ space group (ICSD # 9866). It is worth noting that nanograin agglomeration in micrometric and/or submicrometric cluster may ensure a suitable tap density in the electrode and fast reaction kinetics due to short electron paths [80,206], while a low carbon content (below 4 wt.% in the composite) may lead to a relevant gravimetric capacity. Besides such promising morphological characteristics for an application in lithium-ion cells, the NiO@C electrode is expected to benefit from conductive Ni metal particles, possibly enhancing the rate capability.

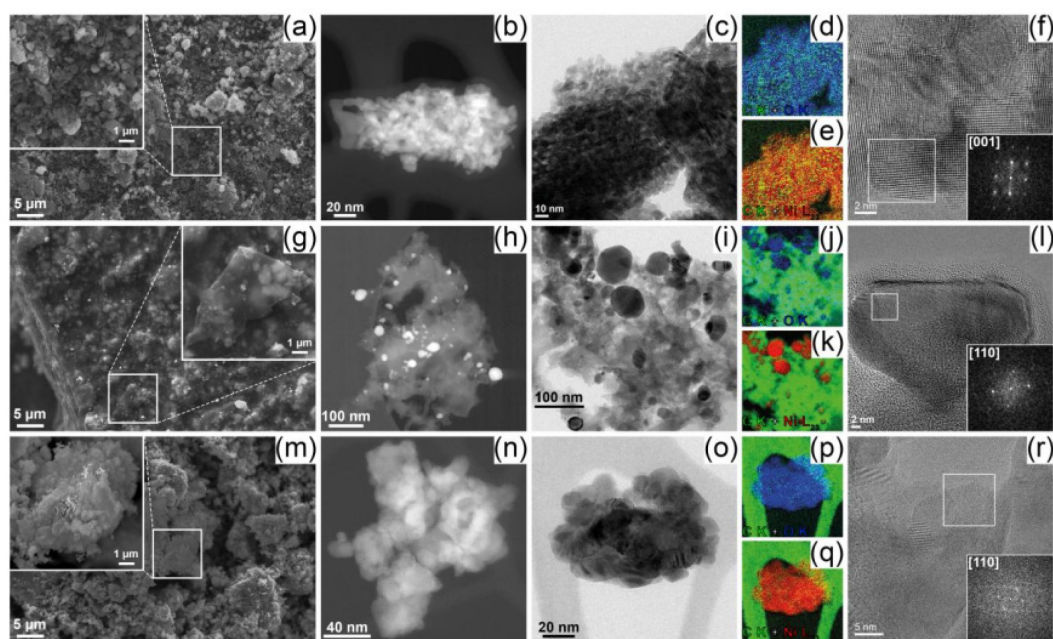


Figure 7.3 Electron microscopy analyses of **(a–f)** bare NiO, **(g–l)** Ni@C, and **(m–r)** NiO@C powders. In detail: **(a, g, and m)** SEM images of the three samples (magnified views in the insets); **(b, h, n)** HAADF-STEM images; **(c, i, and o)** ZL-TEM images and **(d and e, j and k, p and q)** corresponding EFTEM elemental maps, showing the distribution of **(d, j, and p)** C + O (green and blue, respectively) and C + Ni (green and red); **(f, l, and r)** HRTEM images and corresponding fast Fourier transforms (FFTs) results indexed to the **(f and r)** ICSD # 9866 and **(l)** ICSD # 260169 reference structures.

The sample composition has been investigated by elemental mapping upon SEM-EDS (**Figure 7.4**) as well as by EELS (**Figure 7.5**). No clear edge is visible for carbon in the EEL spectra of NiO@C, although it is still possible to obtain quantitative information suggesting a weight ratio below 5%, in full agreement with the value suggested by EDS analyses. Low carbon content is revealed by SEM-EDS (below 4 wt.%, **Figure 7.4**), along with the absence of a clear edge for carbon in the EEL spectra (**Figure 7.5**), thus confirming the more accurate estimation by XRD and TGA data (below 4 wt.%). Carbon content in Ni@C between 54 and 62 wt.% is detected, according to SEM-EDS and EELS (see **Figure 7.4c, d**, and **Figure 7.5a**). The data, shown in **Figures 7.3, 7.4**, and **7.5**, confirm significant rearrangements of pristine NiO particles after the subsequent thermal treatments.

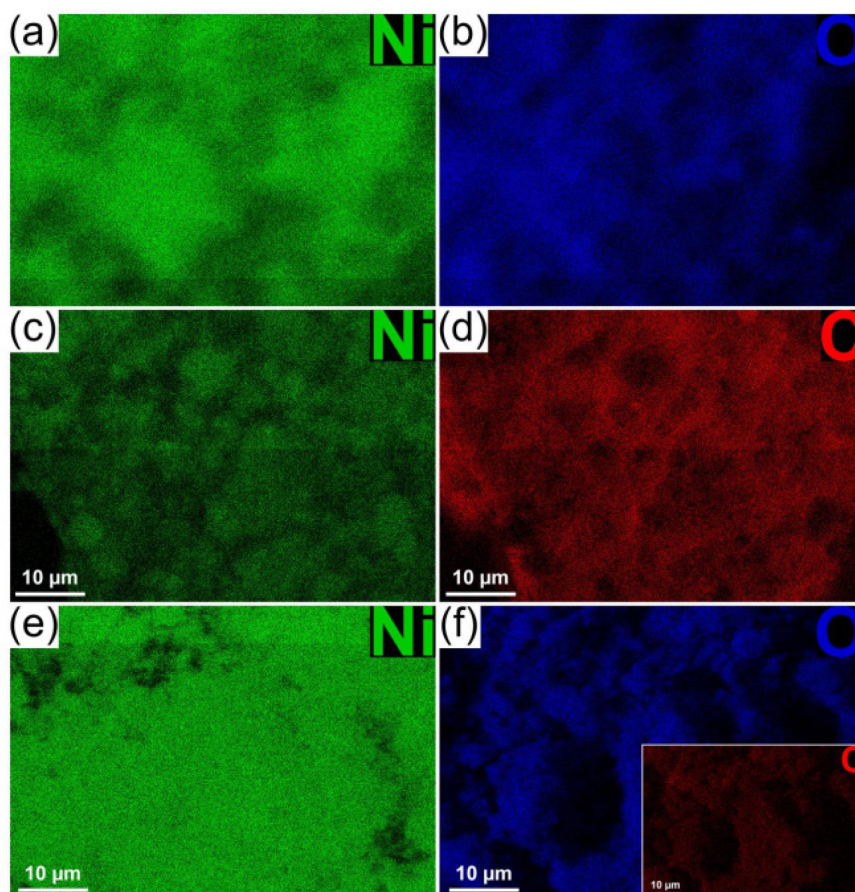


Figure 7.4. SEM-EDS elemental mapping of (green; **a**, **c**, and **e**) Ni, (blue; **b** and **f**) O, and (red; **d**, inset of panel **f**) C, over the particles of (**a** and **b**) bare NiO, (**c** and **d**) Ni@C, and (**e** and **f**) NiO@C.

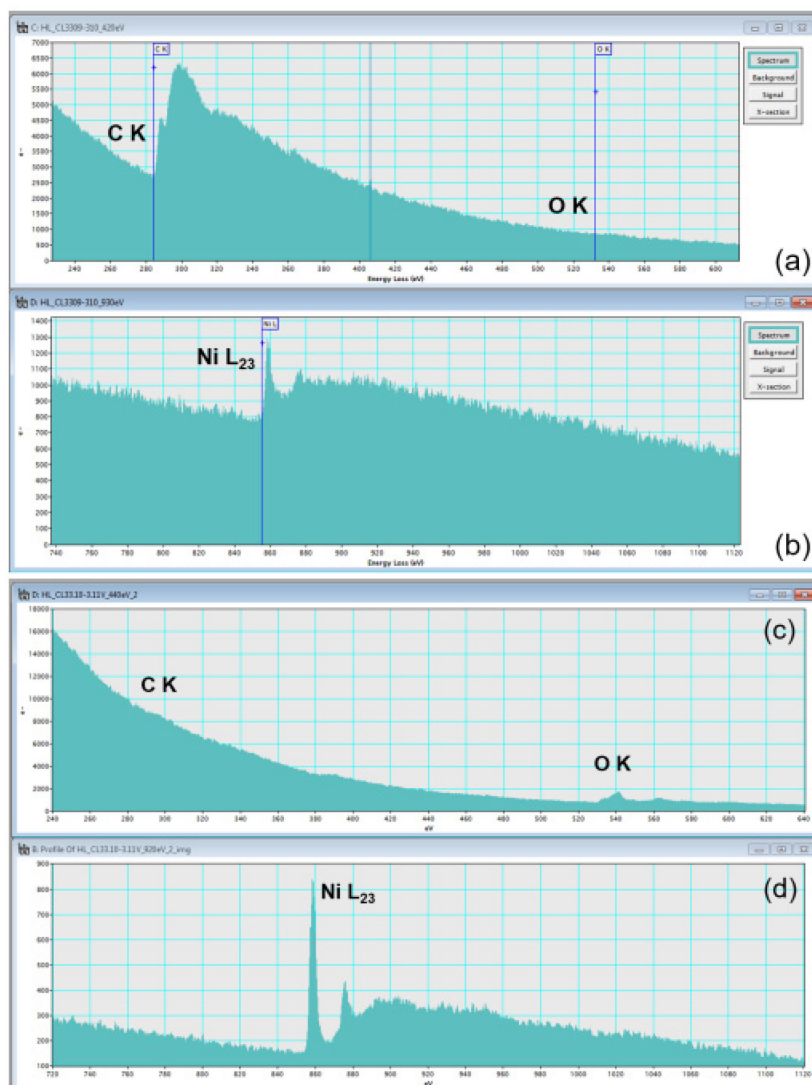


Figure 7.5 EELS acquired at (a and c) K ionization edges of C, O, and (b and d) at the L₂₃ ionization edge of Ni in (a and b) Ni@C and (c and d) NiO@C.

The conversion process of NiO and NiO@C has been comparatively characterized by coupling CV and EIS measurements in three-electrode cells. **Figure 7.6** reports the related voltammetry profiles upon 3 cycles, and the Nyquist plots (**Figure 7.6** insets) recorded at the OCV and after each discharge/charge cycle (working electrode in the charged condition). During the first voltammetry scan towards low potential, pristine NiO shows a minor cathodic peak at 0.8 V vs. Li⁺/Li, followed by a strong signal at 0.6 V vs. Li⁺/Li (**Figure 7.6a**), while NiO@C exhibits only a peak at 0.6 vs. Li⁺/Li (**Figure 7.6b**). These responses are attributed to the well-known

displacement of nickel oxide by reduction to form metallic Ni embedded into a Li₂O matrix [107] and to the formation of SEI [199]. Hence, both electrodes undergo reversible oxidation throughout the first scan towards high potential by electrochemical processes mostly occurring at 2.2 V vs. Li⁺/Li, although pristine NiO shows a further small peak at 1.4 V vs. Li⁺/Li [207]. During the subsequent cycles, the reduction peak of NiO and NiO@C shifts to higher potential, *i.e.*, to 1.1 and 1.3 V vs. Li⁺/Li, respectively, suggesting massive electrode rearrangements associated with the electrochemical conversion [199].

Despite the similar CV response, NiO@C exhibits a significantly lower polarization indicating improved electrode kinetics, further demonstrated by EIS (**Figure 7.6** insets). The EIS measurements show the pristine NiO electrode at OCV an electrode/electrolyte interphase represented by a medium-high frequency semicircle with a resistance of about 22 Ω, initially decreasing after the 1st cycle, and then increasing to about 30 Ω (inset of **Figure 7.6a**). Such an increase of the resistance might indicate microstructural reorganization within the electrodes as well as a gradual growth and modification of the SEI layer [199]. In addition, the EIS reveals a lower resistance for NiO@C at the OCV condition compared to the pristine NiO (about 17 Ω), and a less relevant rise upon 3 CV cycles (to about 20 Ω), thereby suggesting improved electronic conductivity due to the carbon traces and beneficial effects on the electrode/electrolyte interphase.

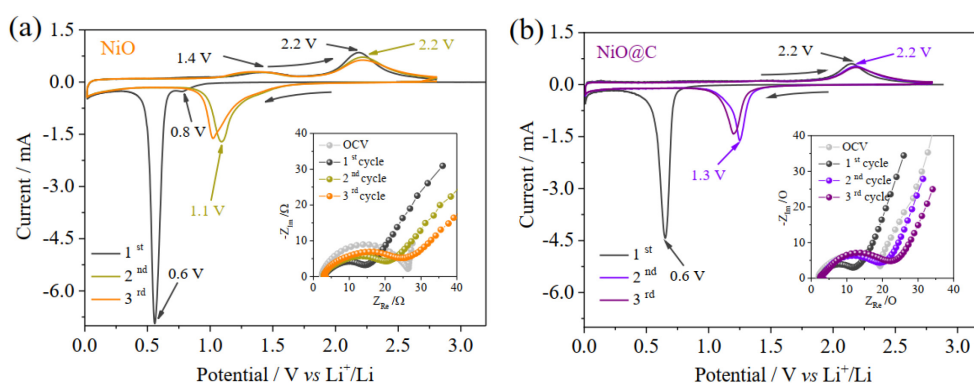


Figure 7.6 CV and (insets) EIS Nyquist plots of (a) NiO and (b) NiO@C in three-electrode lithium half-cells. CV performed between 0.01 and 2.8 V vs. Li⁺/Li at 0.1 mV s⁻¹. Impedance spectra recorded at the OCV and after 1, 2, and 3 full voltammetry cycles by applying an AC potential of 10 mV amplitude in the 500 kHz to 100 mHz frequency range.

Such an improvement is further revealed by comparative cycling tests at a C/5 rate of the bare nano powder, the metal-carbon precursor, and the final composite (**Figure 7.7a** and **b**, $1C = 718 \text{ mA g}^{-1}$). The first discharge of NiO and NiO@C, respectively, reveals plateaus at about 0.6 and 0.7 V with capacities of 970 and 1310 mAh g^{-1} partially ascribed to the SEI formation [80]. The subsequent charge evolves within a wide voltage range and is characterized by a plateau at about 2.2 and 2.1 V, according to the remarkable hysteresis of conversion materials [107], leading to reversible capacities of 690 and 820 mAh g^{-1} for the pristine and C-coated electrodes, respectively. Moreover, pristine NiO exhibits a further minor activity at about 0.8 V during discharge and at 1.4 V during charge (**Figure 7.7a**). A minor contribution of carbon to the lithium exchange by insertion at low voltage might partially account for the higher reversible capacity of NiO@C with respect to the theoretical capacity of NiO (i.e., 718 mAh g^{-1}) [208]. However, the Ni@C synthesis' intermediate shows a modest reversible electrochemical activity (about 100 mAh g^{-1}) mainly due to lithium (de)insertion into the lowly crystalline carbon of Ni@C, beside first-cycle electrolyte decomposition at low voltage.

Although both NiO and NiO@C exhibit reversible displacement upon three cycles, **Figure 7.7b** reveal an abrupt failure of NiO after 10 cycles and much-improved capacity retention and coulombic efficiency for NiO@C. Furthermore, the galvanostatic profiles (**Figure 7.7a**) show that the electroreduction processes of NiO@C occur at a lower voltage than that of bare NiO, that is, about 1.3 V for the former and about 1.1 V for the latter after the first cycle. Such a shift of the reaction potentials towards higher value after the two-step treatment might reflect an improvement of the charge transfer at the electrode/electrolyte interphase, thus leading to a decrease in cell polarization [194]. Hence, **Figure 7.7b** reveals a fast capacity fade down to about 100 mAh g^{-1} for bare NiO, while NiO@C exhibits a much more stable behavior with a reversible capacity of 580 mAh g^{-1} after 50 cycles and satisfactory coulombic efficiency.

The rate capability of the NiO@C material has been assessed by performing cycling tests at increasing current rates. **Figure 7.7c** and **d** show the related voltage profiles and capacity trend, respectively. The nanocomposite anode displays a moderate polarization increasing by raising the current (**Figure 7.7c**) and reversible capacities of about 910, 860, 770, 690, 610, 510, and

390 mAh g⁻¹ at C/10, C/8, C/5, C/3, C/2, 1C, and 2C rates, respectively. This promising rate capability might be ascribed to the carbon traces (below 4 wt. %) as well as to the presence of conductive nickel (3–4 wt.%) [209]. However, the material exhibits a capacity fade as the current is lowered down to the rate of C/10 at the 36th cycle, with a final value of about 730 mAh g⁻¹ at the 40th cycle most likely attributed to partially irreversible rearrangement of the electrode material during the conversion process [203,210].

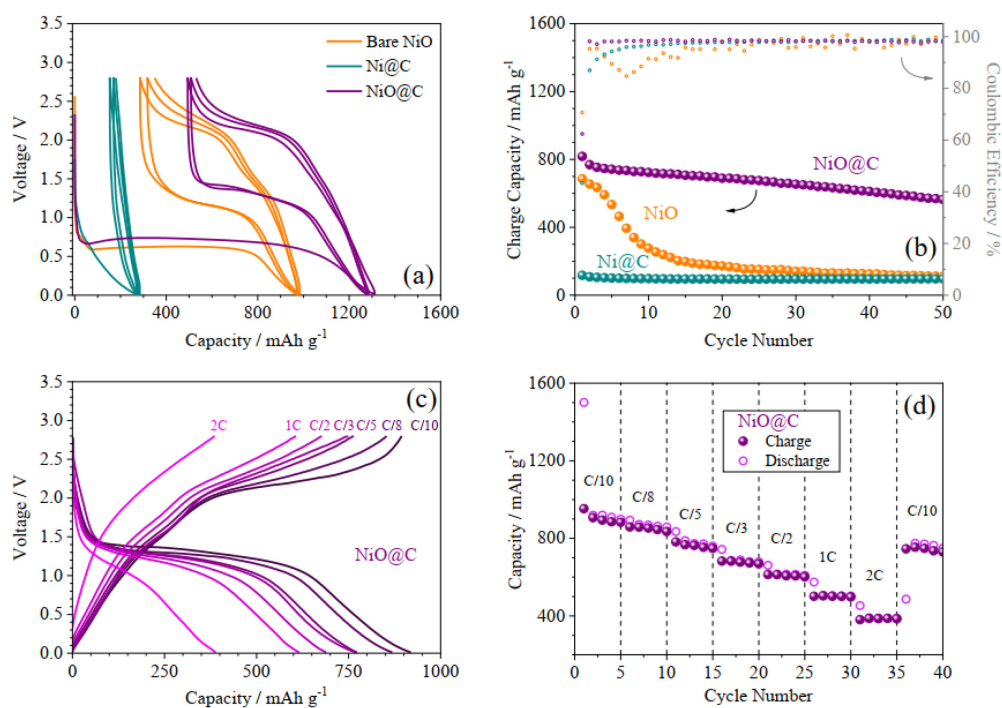


Figure 7.7 (a and b) Cycling response of NiO, Ni@C, and NiO@C in two-electrode half-cells at a C/5 rate in terms of (a) voltage profiles and (b) cycling trend. (c and d). Rate capability tests of NiO@C in a two-electrode half-cell at various rates ranging from C/10 to 2C, in terms of (c) voltage profiles and (d) cycling trend.

Figure 7.8 reports the NiO@C/NCM battery response in terms of selected voltage profile (panel a) and cycling behavior (panel b) at a constant current of C/2 rate referred to the cathode mass (where 1C is arbitrarily set at 170 mA g_{cathode}⁻¹). During the first cycle, the cell delivers about 160 mAh g_{cathode}⁻¹ in spite of an irreversible capacity of about 67 mAh g_{cathode}⁻¹, corresponding to a low initial coulombic efficiency (around 70%), which indicates oxidative

electrolyte decomposition possibly related to the formation of a passivation layer over the cathode electrode (see **Figure 7.8a** inset) [211]. Afterwards, the voltage signature stably reflects the combination of reversible Li^+ exchange by conversion process at the anode and (de)intercalation at the cathode, leading to sloped plateaus within the range from 1.5 to 4.3 V, which are centered at about 2.5 V (see **Figure 7.8a**). Accordingly, the NiO@C/NCM battery shows a reversible capacity slightly increasing to almost $170 \text{ mAh g}_{\text{cathode}}^{-1}$ over the first 30 cycles with a steady-state coulombic efficiency above 99%, and then slowly decreasing to about $140 \text{ mAh g}_{\text{cathode}}^{-1}$ after 80 cycles (ca. 88% of the initial value) due to a decrease in coulombic efficiency to about 97% (**Figure 7.8b**), and a gradual decay of the average voltage (**Figure 7.8a**).

On the other hand, the responses of NCM and NiO@C electrodes during full-cell operation have been monitored by the support of the additional lithium reference electrode. **Figure 7.8c-f** reports the voltage profiles of the NiO@C/NCM cell (blue curve) cycled at a rate of $C/2$ ($1C = 170 \text{ mA g}_{\text{cathode}}^{-1}$) within a voltage range between anode and cathode of 0.8 – 4.3 V as a function of time at the 1st, 10th, 50th, and 80th cycles. The potentials of NiO@C and NCM vs. Li^+/Li monitored through the lithium electrode upon cycling are also reported in **Figure 7.8c-f** (purple and red colors, respectively). Accordingly, the measurement reveals that the voltage decay of the cell actually reflects a gradual increase in the potential of the negative electrode, that is, a progressive anode de-lithiation during cycling, which leads to a rise in the potential of the positive electrode up to full-charge values exceeding 5 V vs. Li^+/Li after 50 cycles. This phenomenon may be ascribed to irreversible parasitic processes occurring in the cell besides the Li-intercalation at the cathode and NiO conversion at the anode [23]. Notably, a remarkable cycle life may be achieved by ensuring coulombic efficiency values approaching 100% [190] or a suitable compensation of the irreversible capacity losses occurring at the anode side [212]. It is worth considering that the wide working potential window of metal oxide anodes alongside a relevant hysteresis between charge and discharge may further magnify this gradual cell unbalancing [107].

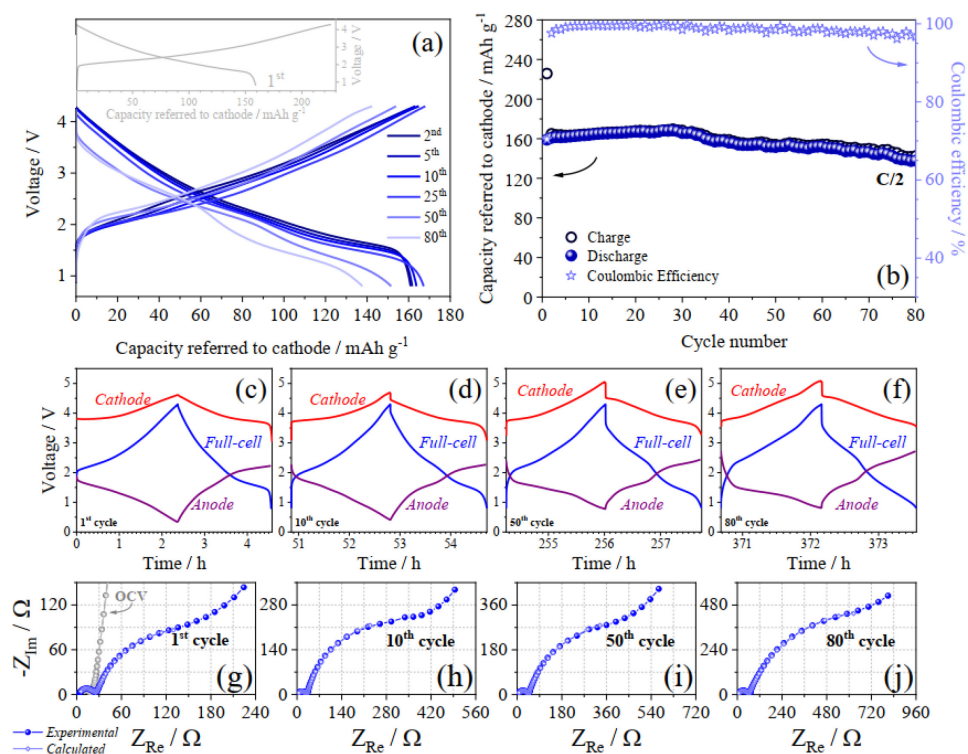


Figure 7.8 Electrochemical characterization of the NiO@C/NCM cell. In detail: (a–b) galvanostatic cycling at a rate of C/2 in terms of (a) selected voltage profiles and (b) cycling behavior ($1C = 170 \text{ mA g}_{\text{cathode}}^{-1}$); (c–f) potential of anode and cathode vs. Li^+/Li as measured by a lithium-metal reference probe in the cell and corresponding voltage profile of the full cell (i.e., cathode vs. anode) for the (c) 1st, (d) 10th, (e) 50th, and (f) 80th cycles; (g–j) experimental and simulated EIS Nyquist plots of the full cell at the (g) OCV and after the (g) 1st, (h) 10th, (i) 50th, and (j) 80th cycles at the charged state.

The evolution of the anode and cathode interphases in a NiO@C/NCM cell during galvanostatic cycling have been investigated by EIS measurements performed by utilizing a lithium metal reference probe as reference electrode for monitoring either NiO@C or NCM interphases (see **Figure 7.9**). Indeed, EIS measurements of the full-cell have been carried out at the OCV and after the 1st, 10th, 50th, and 80th cycle at the charged state (**Figure 7.9g–j** shows the related Nyquist plots). The obtained data have been modelled by the $R_e(R_{(hf)1}Q_{(hf)1})(R_{(hf)2}Q_{(hf)2})(R_{(lf)}Q_{(lf)})$ equivalent circuit (see **Table 7.2**). This circuit takes into account the electrolyte resistance (R_e) and several resistive and pseudocapacitive elements that simulate the cell response within the investigated frequency range, thus enabling the study of various kinetic processes attributable

to the NiO@C and NCM electrodes. In detail, the $(R_{(hf)i}Q_{(hf)i})$ sub-circuit ($i = 1, 2$) reflects the response of the cell at the high-medium frequency (briefly indicated as the high-frequency region), occurring as a small semicircle in the Nyquist plots of **Figure 7.9g–j**, while the $(R_{(lf)}Q_{(lf)})$ sub-circuit describes the large semicircle at the medium-low frequency (briefly indicated as the low-frequency region).

Further spectra of the NiO@C and NCM electrodes performed employing the additional lithium reference probe (**Figure 7.9a, c, e, g, and i** for Li/NiO@C side and **Figure 7.9b, d, f, h, and j** for Li/NCM side) suggest a characteristic low-frequency response for NiO@C and NCM, that is, a Warburg-type diffusion for the former and a slow charge transfer for the latter after the 1st cycle, as well as a high-frequency region mostly reflecting the lithium passivation [198]. It is noteworthy that such a high charge transfer resistance at the cathode is in full agreement with the expected low Li^+ content in the NCM lattice in charged condition [213]. The $(R_{(lf)}Q_{(lf)})$ sub-circuit (large low-frequency semicircle in **Figure 7.8g–j**) refers to the cathode charge transfer resistance and double-layer capacitance. Besides, the $(R_{(hf)i}Q_{(hf)i})$ sub-circuit ($i = 1, 2$) can ascribe to the passivation layers over the electrodes [214].

Notably, the EIS data at the OCV indicate the absence of charge transference in the cathode, which behaves as blocking electrode at about 3 V vs. Li^+/Li [198] (shown in **Figure 7.8g** and **Figure 7.9b**), and overall high-frequency electrode/electrolyte interphase resistance of the order of 20 Ω in the lithium-ion cell ($\Sigma R_{(hf)i}$ in **Table 7.2**). Galvanostatic cycling leads to an expected gradual increase of $\Sigma R_{(hf)i}$ up to values approaching 60 Ω at the 80th cycle, which might be attributed to the growth of passivation layers over the electrodes owing to the abovementioned parasitic reactions [208], along with a raise of the cathode charge transfer resistance ($R_{(lf)}$) from about 240 Ω after the 1st cycle to about 1200 Ω after the 80th cycle (see **Table 7.2**). This raise may be directly related to the increase in potential vs. Li^+/Li of the positive electrode during cycling promoted by the concomitant change of the anode profile (see **Figure 7.8c–f**), which reflects a decreasing Li^+ concentration in the NCM lattice at the charged state [213]. This trend suggests an increasing influence of the microstructural reorganization of

the anode during the final stages of the cycling test leading to a progressive change of the cell balance [199].

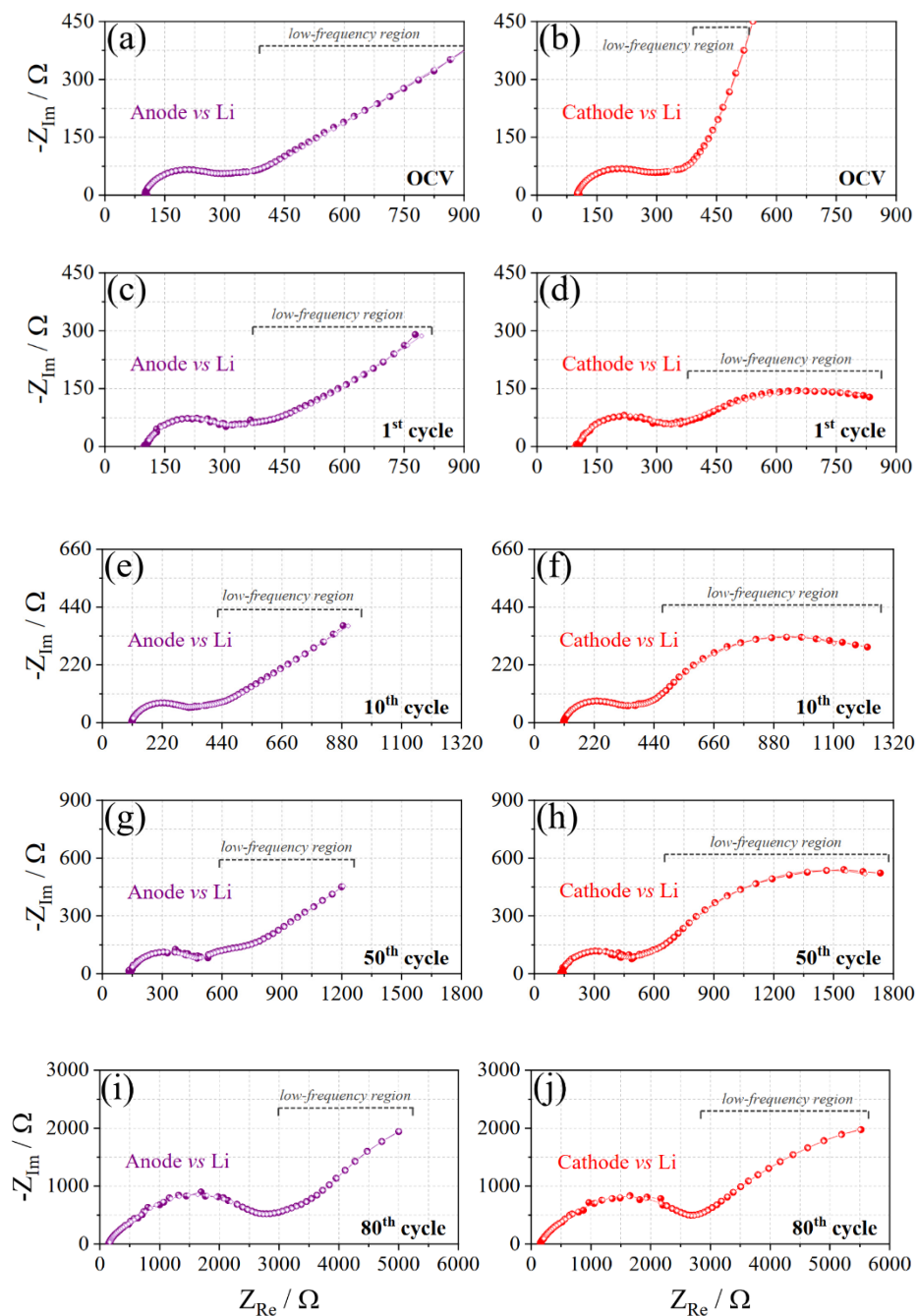


Figure 7.9 EIS Nyquist plots of (a, c, e, g, and i) NiO@C and (b, d, f, h, and j) NCM in the NiO@C/NCM full cell as measured by using a lithium-metal reference. EIS carried out at the (a–b) OCV and after the (c–d) 1st, (e–f) 10th, (g–h) 50th, and (i–j) 80th cycles at the charged state.

Cell condition	Equivalent Circuit	χ^2	$\sum R_{(hf)i}/\Omega$ (i = 1, 2)	$R_{(lf)}/\Omega$
OCV	$R_e(R_{(hf)1}Q_{(hf)1})(R_{(hf)2}Q_{(hf)2})Q_{(hf)}$	1.8×10^{-4}	21 ± 7	–
1 st cycle	$R_e(R_{(hf)1}Q_{(hf)1})(R_{(hf)2}Q_{(hf)2})(R_{(hf)}Q_{(hf)})$	2.5×10^{-4}	22 ± 10	238 ± 8
10 th cycle	$R_e(R_{(hf)1}Q_{(hf)1})(R_{(hf)2}Q_{(hf)2})(R_{(hf)}Q_{(hf)})$	2.6×10^{-4}	29 ± 15	570 ± 20
50 th cycle	$R_e(R_{(hf)1}Q_{(hf)1})(R_{(hf)}Q_{(hf)})$	4.0×10^{-4}	42.5 ± 0.5	790 ± 30
80 th cycle	$R_e(R_{(hf)1}Q_{(hf)1})(R_{(hf)2}Q_{(hf)2})(R_{(hf)}Q_{(hf)})$	5.2×10^{-4}	58 ± 14	1260 ± 40

Table 7.2 Results of NLLS analysis of EIS data on the NiO@C/NCM cell at the OCV and after the 1st, 10th, 50th, and 80th cycles at the charged state in terms of χ^2 parameter and electrode/electrolyte interphase resistance. $\sum R_{(hf)i}/\Omega$ (i = 1, 2) is the sum of interphase resistances at the high-medium frequency (briefly high-frequency region) and $R_{(lf)}/\Omega$ is the interphase resistance at the medium-low frequency (briefly low-frequency region).

The effect of the electrode kinetics on the battery performance is further revealed by a rate capability test of a full NCM/NiO@C cell using the additional lithium probe reference to monitor the anode and the cathode potentials at C-rates from C/5 to 2C. The results are reported in **Figure 7.10** as cycling trend (panel **a**), potential profiles of NiO@C and NCM electrodes vs. the lithium-metal reference (panels **b** and **c**, respectively), and voltage curves of the full NiO@C/NCM cell (panel **d**). The lithium-ion battery exhibits a decrease in capacity as the current increases, delivering about 178, 173, 161, 137, and 98 mAh g_{cathode}^{-1} at current rates of C/5, C/3, C/2, 1C, and 2C, respectively; a current decrease back to the initial value of C/5 rate at the 51st cycle leads to a capacity of about 171 mAh g_{cathode}^{-1} .

An increase of cell polarization by current rising (see **Figure 7.10d**) reflects the expected overvoltage at the anode and cathode sides (see **Figure 7.10b** and **c**, respectively), while the modification of the electrode potential measured by the lithium probe suggests a gradual decrease in the Li^+ concentration in both NiO@C and NCM during cycling, which is in accordance with the results of **Figure 7.8**. In this regard, mitigation of parasitic Li^+ consumption

due to irreversible processes, occurring in the so-called “*rocking chair*” battery besides the (de)intercalation within the cathode and metal oxide conversion, is considered a crucial challenge that needs to be overcome for application [215].

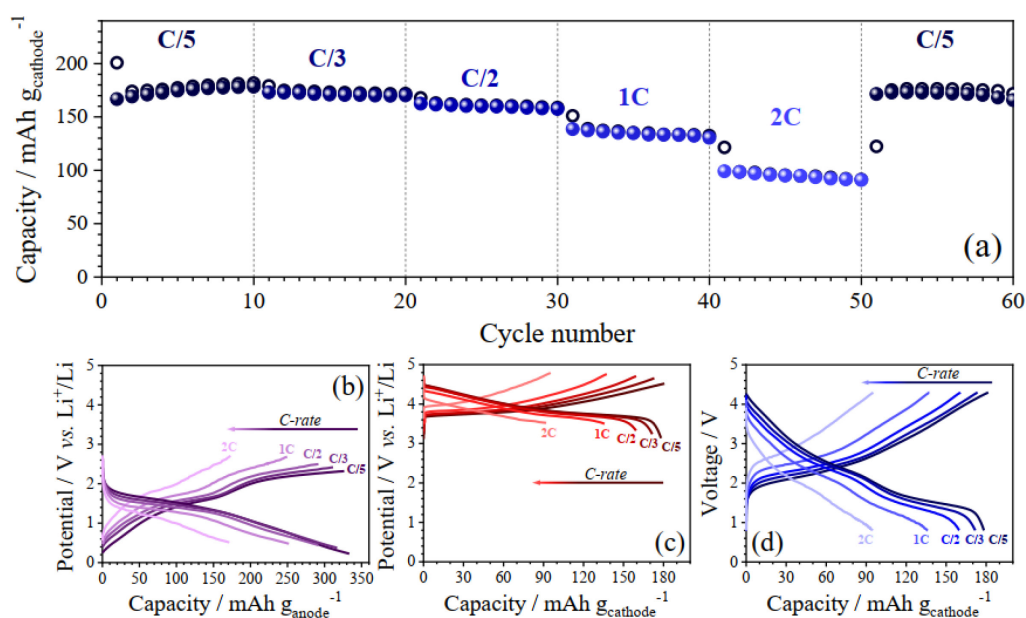


Figure 7.10 A rate capability test at C-rates from C/5 to 2C ($1C = 170 \text{ mA g}_{\text{cathode}}^{-1}$) in terms of (a) cycling life, potential profiles of (b) NiO@C and (c) NCM vs. Li^+/Li as measured by a lithium-metal reference probe in the cell, and (d) voltage curves of the NiO@C/NCM cell.

7.3 Conclusion

A NiO anode was prepared by a simple two-step pathway based on the reduction of oxide nanoparticles to metallic Ni embedded into a carbon matrix and subsequent mild oxidation of the metallic core. A comprehensive structural, compositional, and morphological investigation revealed NiO grains around between 10 and 50 nm forming aggregates ranging from about 100 nm to about 5 μm , as well as metallic Ni particles (3–4 wt.%) with crystallite size of the order of 100 nm and C traces (below 4 wt.%). The resulting NiO@C nanocomposite showed high reactivity in the cell, exchanging Li^+ by a conversion process mostly occurring at 1.3 V vs. Li^+/Li during discharge and at 2.2 V vs. Li^+/Li during charge.

Preliminary results indicated that the two-step treatment remarkably enhances the characteristics of the metal oxide leading to a composite electrode delivering almost 800 mAh g⁻¹ at a C/5 rate. In particular, the material exhibited a higher specific capacity, faster kinetics at the electrode/electrolyte interphase, and a significantly longer cycle life than the pristine nano-powder. Accordingly, a suitable rate capability within the C-rates range from C/10 to 2C suggested possible application of the electrode in LIBs.

The NiO@C/NCM battery operated at about 2.5 V through sloped curves within the wide window from 1.0 to 4.3 V by delivering about 160 mAh g_{cathode}⁻¹ with reversibility and coulombic efficiency suitable to ensure about 80 cycles. Electrochemical measurements monitoring the potential vs. Li⁺/Li of anode and cathode revealed a gradual decrease in Li⁺ concentration in both electrodes ascribable to parasitic processes leading to a progressive increase in interphase resistance. These changes yielded a decrease in the average voltage of the cell during the cycling process. These results clarified the actual behavior of an enhanced nanostructured metal oxide anode in a lithium-ion battery, thereby providing valuable electrochemical contribution for further debating the applicability of the conversion anodes.

7.4 Experimental section

7.4.1 NiO@C samples

2 g of NiO (Sigma-Aldrich, <50 nm) was suspended in a water/ethanol solution (50 mL, 1:1 v/v). 4 g of sucrose was added to the above-mentioned suspension, and the solvent was evaporated at 70 °C under stirring. The dry mixture was under an argon flow heated at 120 °C for 10 h and subsequently heated at 600 °C, held at 600 °C for 3 h to obtain Ni@C (step 1). Afterwards, the samples were under a dry air flow heated at 380 °C for 48 h to get NiO@C (step 2). Steps 1 and 2 were carried out in a tubular furnace (GHA, Carbolite) with a heating rate of 10 °C min⁻¹ and natural cooling.

7.4.2 Material characterization

The sample structure (NiO, Ni@C, and NiO@C) was investigated by XRD using a Bruker D8 Advance diffractometer (Cu K α source) by performing scans from 20 to 70° with a step size of 0.02° at 10 s step⁻¹. Rietveld refinement of the diffraction pattern of anode material (NiO@C) was carried out through the MAUD software [44] by using reference structures with cubic unit cell and space group (ICSD # 260169 and # 9866) for NiO and Ni. The atom occupancies for the NiO phase have been fixed to the stoichiometric values, and the atomic displacement parameters have been forced to have the same value for each element. Lattice parameters, crystallite size, and crystal phase ratio were refined to get suitable weighted-profile ($R_{wp}\%$) and goodness-of-fit (σ) values (see **Table 7.1**). A TGA was performed under an air flow (50 mL min⁻¹) by heating a NiO@C sample from 30 to 800 °C at 10 °C min⁻¹ heating rate through a TGA Q500 from TA instruments.

Morphology, structure, and elemental composition (NiO, Ni@C, and NiO@C) were studied by SEM, SEM-energy dispersive X-ray spectroscopy (SEM-EDS), energy-filtered TEM (EFTEM), high-resolution TEM (HRTEM), HAADF-STEM, and EELS. A Zeiss EVO MA10 scanning electron microscope employing a tungsten thermionic electron gun and an INCA X-ACT Oxford Instrument analyzer, were used for the SEM and SEM-EDS analysis, respectively.

Each sample for TEM (NiO, Ni@C and NiO@C) was prepared by suspending a spatula tip in ethanol and mildly sonicating; afterwards, the supernatant was drop cast onto a holey amorphous carbon film on Cu grid. The TEM analyses was conducted with a JEOL JEM-2200FS microscope (Schottky emitter) at 200 kV operation, equipped with a CEOS corrector for the objective lens and an in-column image filter (Ω -type). EFTEM imaging was used to acquire elastically filtered (zero-loss, ZL) TEM images by selecting only electrons within 10 eV from the ZL peak, and for elemental mapping, carried out by using the three windows method at the K edge of C (16 eV slit width) and O (20 eV slit width) and the L₂₃ edge of Ni (30 eV slit width). EEL spectra were acquired on regions of the samples suspended on holes in the support film, in diffraction mode ($\alpha = 3.5$ mrad, $\beta = 5.4$ mrad). EELS-based quantification

was performed employing the hydrogenic model for all edges (K edge of C and O and L₂₃ edge of Ni), with the background fit in a 30 eV window before the edge and 70 eV window from the edge onset.

7.4.3 Electrode preparation

The anode active material (*i.e.*, bare NiO, Ni@C, and NiO@C) was mixed with Super P carbon (Timcal) and polyvinylidene fluoride (PVDF 6020, Solvay) in the 8:1:1 weight ratio. The mixture was spread in N-methyl pyrrolidone (NMP, Sigma-Aldrich) and pressed on a copper foil through a doctor blade. The cathode active material (NCM), PVDF 6020 (Solvay), and Super P carbon were mixed with a weight proportion of 8:1:1 in NMP and cast on an aluminum foil through a doctor blade. The cast slurry was heated for 3 h at 70 °C on a hot plate under a fume hood and then dried at 110 °C overnight under vacuum conditions. The anode materials (*i.e.*, bare NiO, Ni@C, and NiO@C) had a mass loading over the electrodes ranging from 1.5 to 2.5 mg cm⁻². The NCM electrodes had an active mass loading ranging from 3.1 and 3.5 mg cm⁻². Disks with diameter of 10 and 14 mm were cut out from these dried foils and employed as working electrodes in three-electrode and two-electrode cells (T-type; 10 mm) and CR2032 coin cells (MTI Corporation; 14 mm), as well as counter electrode in two-electrode full-cells (T-type; 10 mm). Disks with a diameter of 10 mm were cut out from this electrode sheet and employed as working electrodes in two-electrode, lithium-ion cells. The cells were prepared in an argon-filled glove box (pure gas, H₂O and O₂ levels below 1 ppm, MBraun) with lithium metal disks as counter and reference electrodes.

Lithium-ion batteries were assembled by coupling a NiO@C anode (between 1.7 and 2.3 mg cm⁻²) and an NCM cathode (between 3.1 and 3.6 mg cm⁻²) in a T-type two-electrode cell, as well as in a T-type three-electrode cell. The anode was electrochemically activated, as reported below. The glass fiber separator (Whatman, GF/A) was imbibed by an electrolyte solution formed of LiPF₆ (1 M) in a mixture (1:1 w/w) of EC and DMC.

7.4.4 Electrode measurements

CV and EIS tests of the two electrodes (NiO and NiO@C) were performed on three-electrode half-cells (T-type) via a VersaSTAT MC (AMETEK, Princeton Applied Research) multichannel potentiostat. CV was carried out by using a scanning rate of 0.1 mV s^{-1} between the potential range 0.01 and 2.8 V vs. Li^+/Li . Impedance spectra were recorded by applying over the frequency range of 500 kHz to 100 mHz with an AC voltage of 10 mV amplitude at the OCV condition and after 1, 2, and 3 full voltammetry cycles.

Cycling tests of the anode electrodes (NiO, Ni@C, and NiO@C) were performed on two-electrode half-cells (CR2032 coin-cells, MTI Corporation) at a rate of $C/5$ ($1C = 718 \text{ mA g}^{-1}$). Furthermore, the NiO@C electrode rate capability was evaluated by galvanostatic cycling in lithium coin-cells (CR2032 coin-cells, MTI Corporation) with current rates (from $C/10$ to $2C$) increasing every 5 cycles and then decreasing to $C/10$ at the 36th cycle. The voltage window of the galvanostatic measurements was 0.01 to 2.8 V.

7.4.5 Full cell measurements

Prior to the NiO@C/NCM full-cell assembly, the anode was activated by 3 discharge/charge cycles at a $C/5$ rate in a T-type, two-electrode half-cell within the 0.01 – 2.8 V range with a final charge up to 2.2 V. Afterwards, the electrochemically activated NiO@C electrode was recovered from the cell, rinsed with DMC solvent, dried few minutes under vacuum, and used to build the full-cell.

A two-electrode NiO@C/NCM cell was cycled at a rate of $C/2$ (where $1C$ is 170 mA g^{-1} as referred to the positive electrode) in the voltage range from 0.8 to 4.3 V. A three-electrode NiO@C/NCM cell employing a lithium-metal reference probe was cycled at a $C/2$ rate in a voltage range of 0.8 – 4.3 V between the NiO@C and NCM electrodes. The potential vs. Li^+/Li of NiO@C and NCM during two-electrode cycling was measured by the abovementioned lithium-metal probe. EIS measurements were carried on the NiO@C/NCM cell at the OCV and after the 1st, 10th, 50th, and 80th cycle (after discharging) by applying an AC voltage of 10 mV

amplitude in the frequency range of 500 kHz – 20 mHz. A NLLS procedure fitting procedure is used for the analysis of impedance spectra [216]

Further EIS measurements Li/NiO@C and Li/NCM sides of the full cell were carried out by using the lithium-metal probe and collected in the frequency range from 500 kHz to 20 mHz with an AC amplitude of 10 mV. Simulation of the spectra has been carried out by NLLS analysis [58] according to the $R_e(R_{(hf)1}Q_{(hf)1})(R_{(hf)2}Q_{(hf)2})(R_{(lf)}Q_{(lf)})$ equivalent circuit. These EIS analyses were applied on the same VersaSTAT MC multichannel potentiostat.

A rate capability test was carried out on the NiO@C/NCM cell by galvanostatic cycling within the current range from C/5 to 2C rates (where 1C is 170 mA g⁻¹ as referred to the positive electrode) and the voltage range between NiO@C and NCM of 0.8 – 4.3 V. Furthermore, the potential vs. Li⁺/Li of NiO@C and NCM during the above cycling was monitored by using the lithium-metal probe. All the galvanostatic measurements were conducted by means of a Maccor Series 4000 battery system at room temperature.

Chapter 8 Conclusions

The electrolyte formulations comprising glymes with various chain lengths dissolved various lithium salts have advantages over conventional electrolytes owing to their suitable ion transport properties, greater electrochemical stability window, and suitable safety content. With regards to transition metal oxides, NiO is an appealing anode candidate because of its high lithium storage capacity, high abundance, and cheap price. Hence, this thesis has characterized the electrochemical features of twelve glyme-based electrolytes and investigated the microstructural features and electrochemical performance of NiO anode material.

The comparative study revealed that the electrolyte formulation in terms of lithium salt nature and ether chain length plays a crucial role in determining suitable electrochemical features for ensuring remarkable cell performances, as presented in **Chapter 5**. Electrolyte solutions based on low-molecular-weight glymes can be efficiently employed in rechargeable batteries coupling insertion LFP olivine cathode and high-energy lithium metal anode. For example, the solutions of LiFSI in DEGDME and TREGDME had promising characteristics for application and formed suitable interphase with the lithium metal electrode, thereby leading to lithium cells with stable capacity ranging between 134 and 144 mAh g⁻¹ upon 100 cycles at a C/3 rate (1C = 170 mA g⁻¹). The results in **Chapter 5** demonstrated the suitable electrochemical characteristics of glyme-based solutions for lithium cells employing olivine cathodes.

In **Chapter 6**, diglyme and triglyme-based solutions using LiFSI, LiTFSI, and LiBETI, enhanced by the LiNO₃ additive, were investigated. A detailed electrochemical study revealed optimal characteristics in terms of ionic transport and stability against the lithium-metal anode. The results confirmed the beneficial effect of LiNO₃ on both the positive and negative interphases, suggesting that the electrochemical stability of a particular glyme-based electrolyte formulation against the cathode is not exclusively related to the electrochemical stability window. Indeed, LiNO₃ ensured the formation of a stable interphase at the anode for all the

electrolyte formulations, although the glyme length strongly affected the interphase behavior at the cathode.

In **Chapter 7**, the NiO@C anode exhibited a charging potential higher than that of graphite, which actually penalizes the working voltage of the lithium-ion cell as compared to conventional batteries, although it may deliver a reversible capacity as high as 800 mAh g^{-1} , thereby decreasing the overall cell weight. Accordingly, the NiO@C/NCM cell had a lower energy density than that of standard LIBs. Meanwhile, this comparative investigation revealed how the anode electrochemistry may affect the characteristics of the lithium-ion battery in terms of working voltage, coulombic efficiency, and cycling stability.

Chapter 9 Outlook

Fossil fuel combustion, increasing prices of petroleum and natural gas, global warming, and the ever-growing energy demand stimulate a worldwide shift towards the integration of RES and the development of sustainable storage technologies. Developing novel electrolytes that are relatively stable against lithium metals and a competitive electrode material that exhibit higher energy density in lithium-ion full cell remain a crucial issue for solving the requirements of large-scale energy storage and smart grids in the future. This investigation has been devoted to developing glyme-based electrolytes for lithium metal batteries and high-performance NiO@C anode for lithium-ion batteries.

The results in this thesis demonstrate that glyme-based electrolytes may be of interest for efficient and safe use of the metal anode in high-energy batteries, which can create a certain degree of possibility to make the lithium metal battery a reality, and the straightforward two-step technique might facilitate a possible application of conversion anodes in the full cell. However, a number of research questions about glyme-based electrolytes and electrode materials remain which require further study.

A possible effect of the anion on cathode/electrolyte interphase might be investigated by coupling electrochemical and spectroscopic techniques in further works aiming at cell performance optimization. However, the minor effects of cell assembling and electrode morphology on the magnitude of the observed activation trend cannot be excluded.

In the NiO@C/NCM full cell, the massive potential hysteresis between charge and discharge has an adverse effect on energy efficiency. The higher working voltage than that of graphite might mitigate possible lithium plating at the anode side, that is, a detrimental phenomenon with a crucial impact on the safety level of cells and battery packs. Lithium electrodeposition on graphite is promoted by charging at low temperature and may lead to poor cycling performance, capacity fading, and, in the worst-case scenario, thermal runaways and

uncontrolled exothermic reactions [217,218]. Therefore, high-voltage anodes might be more suitable than graphite for low-temperature applications [194].

Our results on full cell highlighted the issues still hindering a transition of conversion metal oxides from the laboratory to the market, which might be underestimated in the various works focusing on the synthesis, characterization, and tests in the half cell.

Hence, some concrete ways could be explored further:

- Cycling tests of NiO@C anode in lithium half cells at low temperatures.
- Using layered or spinel oxide cathode materials (LFP and LNMO) in lithium-ion full cells to replace NCM.
- Employing X-ray nano-computed tomography to study the structural and morphological modifications in transition metal oxides, for example, α -Fe₂O₃@C anode material.
- Galvanostatic measurements for NiO@C and α -Fe₂O₃@C anodes in sodium ion batteries.

References

- [1] H. Zabed, J.N. Sahu, A. Suely, A.N. Boyce, G. Faruq, *Renew. Sustain. Energy Rev.* 71 (2017) 475–501.
- [2] D. Larcher, J.M. Tarascon, *Nat. Chem.* 7 (2015) 19–29.
- [3] F. Weschenfelder, G. de Novaes Pires Leite, A.C. Araújo da Costa, O. de Castro Vilela, C.M. Ribeiro, A.A. Villa Ochoa, A.M. Araújo, *J. Clean. Prod.* 257 (2020) 120617.
- [4] J. Meng, L. Cai, D. Stroe, J. Ma, G. Luo, R. Teodorescu, *Energy* 206 (2020) 118140.
- [5] G. Notton, M.-L. Nivet, C. Voyant, C. Paoli, C. Darras, F. Motte, A. Fouilloy, *Renew. Sustain. Energy Rev.* 87 (2018) 96–105.
- [6] D. Di Lecce, R. Verrelli, J. Hassoun, *Green Chem.* 19 (2017) 3442–3467.
- [7] H. Yang, H.H. Wu, M. Ge, L. Li, Y. Yuan, Q. Yao, J. Chen, L. Xia, J. Zheng, Z. Chen, J. Duan, K. Kisslinger, X.C. Zeng, W.K. Lee, Q. Zhang, J. Lu, *Adv. Funct. Mater.* 29 (2019) 1808825.
- [8] F. Wu, J. Maier, Y. Yu, *Chem. Soc. Rev.* 49 (2020) 1569–1614.
- [9] A. Manthiram, *Nat. Commun.* 11 (2020) 1550.
- [10] B. Dunn, H. Kamath, J.-M. Tarascon, *Science* (80-.). 334 (2011) 928–935.
- [11] Y. Li, K. Liu, A.M. Foley, A. Zülke, M. Bercibar, E. Nanini-Maury, J. Van Mierlo, H.E. Hoster, *Renew. Sustain. Energy Rev.* 113 (2019) 109254.
- [12] C.X. Zu, H. Li, *Energy Environ. Sci.* 4 (2011) 2614–2624.
- [13] K.J. Laidler, *Can. J. Chem.* 75 (1997) 1552–1565.
- [14] G. Fryer, *Philos. Trans. R. Soc. London* 126 (1836) 107–124.
- [15] In: *Batter. Manag. Syst.*, Springer Netherlands, Dordrecht, 2008, pp. 11–45.
- [16] B. Scrosati, *J. Solid State Electrochem.* 15 (2011) 1623–1630.
- [17] W.S. Harris, *Electrochemical Studies in Cyclic Esters*, Livermore, CA (United States), 1958.
- [18] A. Mauger, C.M. Julien, J.B. Goodenough, K. Zaghib, *J. Electrochem. Soc.* 167 (2020) 070507.
- [19] M.S. WHITTINGHAM, *Science* (80-.). 192 (1976) 1126–1127.

-
- [20] D. Aurbach, M.L. Daroux, P.W. Faguy, E. Yeager, *J. Electrochem. Soc.* 134 (1987) 1611–1620.
- [21] K. Mizushima, P.C. Jones, P.J. Wiseman, J.B. Goodenough, *Mater. Res. Bull.* 15 (1980) 783–789.
- [22] M. Hasegawa, H. Kobayashi, F. Application, P. Data, United States Pat. (1985).
- [23] J.-M. Tarascon, M. Armand, *Nature* 414 (2001) 359–367.
- [24] X. Yu, H. Wu, J.H. Koo, A. Manthiram, *Adv. Energy Mater.* 10 (2020) 1902872.
- [25] S. Fang, D. Bresser, S. Passerini, *Adv. Energy Mater.* 10 (2020) 1902485.
- [26] H. Jung, R. Silva, M. Han, *World Electr. Veh. J.* 9 (2018) 46.
- [27] Y. Ding, Z.P. Cano, A. Yu, J. Lu, Z. Chen, *Electrochem. Energy Rev.* 2 (2019) 1–28.
- [28] R.C. Massé, C. Liu, Y. Li, L. Mai, G. Cao, *Natl. Sci. Rev.* 4 (2017) 26–53.
- [29] D. Stampatori, P.P. Raimondi, M. Noussan, *Energies* 13 (2020) 2638.
- [30] M. Raugei, E. Leccisi, V.M. Fthenakis, *Energy Technol.* 1901146 (2020) 1901146.
- [31] L. Zhou, K. Zhang, Z. Hu, Z. Tao, L. Mai, Y.-M.M. Kang, S.-L.L. Chou, J. Chen, *Adv. Energy Mater.* 8 (2018) 1701415.
- [32] M. Li, J. Lu, Z. Chen, K. Amine, *Adv. Mater.* 30 (2018) 1800561.
- [33] R.S. Rubino, H. Gan, E.S. Takeuchi, *J. Electrochem. Soc.* 148 (2001) A1029.
- [34] F. Rossi, A. Nicolini, *J. Fuel Cell Sci. Technol.* 8 (2011) 051012 (1–9).
- [35] S. Aktas, *Hydrometallurgy* 104 (2010) 106–111.
- [36] Y. Wu, W. Wang, J. Ming, M. Li, L. Xie, X. He, J. Wang, S. Liang, Y. Wu, *Adv. Funct. Mater.* 29 (2019) 1805978.
- [37] M. Chen, X. Jin, Z. Chen, Y. Zhong, Y. Liao, Y. Qiu, G. Cao, W. Li, *J. Mater. Chem. A* 7 (2019) 13120–13129.
- [38] Q. Liu, Z. Hu, M. Chen, C. Zou, H. Jin, S. Wang, S. Chou, Y. Liu, S. Dou, *Adv. Funct. Mater.* 30 (2020) 1909530.
- [39] M.S. Whittingham, *Chem. Rev.* 104 (2004) 4271–4302.
- [40] J. Xu, S. Dou, H. Liu, L. Dai, *Nano Energy* 2 (2013) 439–442.
- [41] X. Lin, M. Salari, L.M.R. Arava, P.M. Ajayan, M.W. Grinstaff, *Chem. Soc. Rev.* 45 (2016) 5848–5887.

-
- [42] F. Wu, G. Yushin, *Energy Environ. Sci.* 10 (2017) 435–459.
- [43] A. Aishova, G. Park, C.S. Yoon, Y. Sun, *Adv. Energy Mater.* 10 (2020) 1903179.
- [44] T. Tian, T.-W. Zhang, Y.-C. Yin, Y.-H. Tan, Y.-H. Song, L.-L. Lu, H.-B. Yao, *Nano Lett.* 20 (2020) 677–685.
- [45] J. Abou-Rjeily, I. Bezza, N.A. Laziz, C. Autret-Lambert, M.T. Sougrati, F. Ghamouss, *Energy Storage Mater.* 26 (2020) 423–432.
- [46] C. Julien, A. Mauger, K. Zaghib, H. Groult, *Materials (Basel)*. 9 (2016) 595.
- [47] K. Lahtinen, T. Rauhala, S. Räsänen, E. Rautama, T. Kallio, *Electrochim. Acta* 327 (2019) 135012.
- [48] M.M. Thackeray, W.I.F. David, P.G. Bruce, J.B. Goodenough, *Mater. Res. Bull.* 18 (1983) 461–472.
- [49] A. Manthiram, *ACS Cent. Sci.* 3 (2017) 1063–1069.
- [50] F. Kong, C. Liang, L. Wang, Y. Zheng, S. Peranathan, R.C. Longo, J.P. Ferraris, M. Kim, K. Cho, *Adv. Energy Mater.* 9 (2019) 1802586.
- [51] L. Mu, W.H. Kan, C. Kuai, Z. Yang, L. Li, C.J. Sun, S. Sainio, M. Avdeev, D. Nordlund, F. Lin, *ACS Appl. Mater. Interfaces* 12 (2020) 12874–12882.
- [52] M.H. Lee, Y.J. Kang, S.T. Myung, Y.K. Sun, *Electrochim. Acta* 50 (2004) 939–948.
- [53] Y.-S. Hong, Y.J. Park, K.S. Ryu, S.H. Chang, Y.-J. Shin, *J. Power Sources* 147 (2005) 214–219.
- [54] S. Yang, X. Wang, X. Yang, Z. Liu, Y. Bai, Y. Wang, H. Shu, *J. Solid State Electrochem.* 16 (2012) 2823–2836.
- [55] T. Ohzuku, Y. Makimura, *Chem. Lett.* 30 (2001) 642–643.
- [56] G. Lee, J. Wu, D. Kim, K. Cho, M. Cho, W. Yang, Y. Kang, *Angew. Chemie Int. Ed.* 59 (2020) 8681–8688.
- [57] J.C. Hunter, *J. Solid State Chem.* 39 (1981) 142–147.
- [58] J.-S.S. Kim, K. Kim, W. Cho, W.H. Shin, R. Kanno, J.W. Choi, *Nano Lett.* 12 (2012) 6358–6365.
- [59] C. Qing, Y. Bai, J. Yang, W. Zhang, *Electrochim. Acta* 56 (2011) 6612–6618.
- [60] A. Manthiram, K. Chemelewski, E.S. Lee, *Energy Environ. Sci.* 7 (2014) 1339–1350.

-
- [61] Y. Nie, W. Xiao, C. Miao, M. Xu, C. Wang, *Electrochim. Acta* 334 (2020) 135654.
- [62] F. Xin, H. Zhou, X. Chen, M. Zuba, N. Chernova, G. Zhou, M.S. Whittingham, *ACS Appl. Mater. Interfaces* 11 (2019) 34889–34894.
- [63] D. Liu, W. Zhu, J. Trottier, C. Gagnon, F. Barray, A. Guerfi, A. Mauger, H. Groult, C.M. Julien, J.B. Goodenough, K. Zaghbi, *RSC Adv.* 4 (2014) 154–167.
- [64] J. Ma, P. Hu, G. Cui, L. Chen, *Chem. Mater.* 28 (2016) 3578–3606.
- [65] N. Kiziltas-Yavuz, M. Yavuz, S. Indris, N.N. Bramnik, M. Knapp, O. Dolotko, B. Das, H. Ehrenberg, A. Bhaskar, *J. Power Sources* 327 (2016) 507–518.
- [66] X. Zhang, F. Cheng, K. Zhang, Y. Liang, S. Yang, J. Liang, J. Chen, *RSC Adv.* 2 (2012) 5669.
- [67] S. Brutti, G. Greco, P. Reale, S. Panero, *Electrochim. Acta* 106 (2013) 483–493.
- [68] H.B. Lin, Y.M. Zhang, J.N. Hu, Y.T. Wang, L.D. Xing, M.Q. Xu, X.P. Li, W.S. Li, *J. Power Sources* 257 (2014) 37–44.
- [69] H. Sun, B. Xia, W. Liu, G. Fang, J. Wu, H.H. Wang, R. Zhang, S. Kaneko, J. Zheng, H.H. Wang, D. Li, *Appl. Surf. Sci.* 331 (2015) 309–314.
- [70] G. Liang, V.K. Peterson, K.W. See, Z. Guo, W.K. Pang, *J. Mater. Chem. A* 8 (2020) 15373–15398.
- [71] G. Liu, Y. Du, W. Liu, L. Wen, *Electrochim. Acta* 209 (2016) 308–314.
- [72] H.-G. Jung, M.W. Jang, J. Hassoun, Y.-K. Sun, B. Scrosati, *Nat. Commun.* 2 (2011) 516.
- [73] A.K. Padhi, K.S. Nanjundaswamy, J.B. Goodenough, *J. Electrochem. Soc.* 144 (1997) 1188–1194.
- [74] X. Wang, Z. Feng, X. Hou, L. Liu, M. He, X. He, J. Huang, Z. Wen, *Chem. Eng. J.* 379 (2020) 122371.
- [75] Y.G. Huang, F.H. Zheng, X.H. Zhang, Q.Y. Li, H.Q. Wang, *Electrochim. Acta* 130 (2014) 740–747.
- [76] J. Come, P.L. Taberna, S. Hamelet, C. Masquelier, P. Simon, *J. Electrochem. Soc.* 158 (2011) 1090–1093.
- [77] Y.C. Zhang, C.Y. Wang, X.D. Tang, *J. Power Sources* 196 (2011) 1513–1520.
- [78] S.H. Yu, S.H. Lee, D.J. Lee, Y.E. Sung, T. Hyeon, *Small* 12 (2016) 2146–2172.
- [79] S. Chae, S.H. Choi, N. Kim, J. Sung, J. Cho, *Angew. Chemie - Int. Ed.* 59 (2020) 110–135.

-
- [80] J. Hassoun, B. Scrosati, *J. Electrochem. Soc.* 162 (2015) A2582–A2588.
- [81] M. V. Reddy, A. Mauger, C.M. Julien, A. Paoella, K. Zaghbi, *Materials (Basel)*. 13 (2020) 1884.
- [82] J. Lu, Z. Chen, F. Pan, Y. Cui, K. Amine, *Electrochem. Energy Rev.* 1 (2018) 35–53.
- [83] V.A. Sethuraman, L.J. Hardwick, V. Srinivasan, R. Kostecki, *J. Power Sources* 195 (2010) 3655–3660.
- [84] Y. Zhai, Y. Dou, D. Zhao, P.F. Fulvio, R.T. Mayes, S. Dai, *Adv. Mater.* 23 (2011) 4828–4850.
- [85] M. Holzapfel, C. Jost, P. Novák, *Chem. Commun.* (2004) 2098–2099.
- [86] S. Liu, X. Xia, S. Deng, L. Zhang, Y. Li, J. Wu, X. Wang, J. Tu, *Energy Storage Mater.* 15 (2018) 31–36.
- [87] M. Fehse, E. Ventosa, *Chempluschem* 80 (2015) 785–795.
- [88] L. Zhao, Y.S. Hu, H. Li, Z. Wang, L. Chen, *Adv. Mater.* 23 (2011) 1385–1388.
- [89] W. Ma, K. Yin, H. Gao, J. Niu, Z. Peng, Z. Zhang, *Nano Energy* 54 (2018) 349–359.
- [90] B. Liu, P. Soares, C. Checkles, Y. Zhao, G. Yu, *Nano Lett.* 13 (2013) 3414–3419.
- [91] M. Marinaro, M. Weinberger, M. Wohlfahrt-Mehrens, *Electrochim. Acta* 206 (2016) 99–107.
- [92] J. Hassoun, P. Reale, S. Panero, B. Scrosati, *Isr. J. Chem.* 48 (2008) 229–234.
- [93] G.A. Elia, F. Nobili, R. Tossici, R. Marassi, A. Savoini, S. Panero, J. Hassoun, *J. Power Sources* 275 (2015) 227–233.
- [94] Y. An, Y. Tian, C. Wei, H. Jiang, B. Xi, S. Xiong, J. Feng, Y. Qian, *ACS Nano* 13 (2019) 13690–13701.
- [95] J. Wang, W. Huang, Y.S. Kim, Y.K. Jeong, S.C. Kim, J. Heo, H.K. Lee, B. Liu, J. Nah, Y. Cui, *Nano Res.* 13 (2020) 1558–1563.
- [96] J. Zhu, K.Y.S. Ng, D. Deng, *ACS Appl. Mater. Interfaces* 6 (2014) 2996–3001.
- [97] Y. Huang, H. Yang, T. Xiong, D. Adekoya, W. Qiu, Z. Wang, S. Zhang, M.S. Balogun, *Energy Storage Mater.* 25 (2020) 41–51.
- [98] V. Etacheri, R. Marom, R. Elazari, G. Salitra, D. Aurbach, *Energy Environ. Sci.* 4 (2011) 3243.
- [99] S. Wei, X. Wang, R. Yu, R. Zhang, M. Liu, Z. Yang, H. Hu, *J. Alloys Compd.* 702 (2017) 372–380.
- [100] S. Wei, X. Wang, M. Liu, R. Zhang, G. Wang, H. Hu, *J. Energy Chem.* 27 (2018) 573–581.

-
- [101] L. Zhang, J. Mu, Z. Wang, G. Li, Y. Zhang, Y. He, *J. Alloys Compd.* 671 (2016) 60–65.
- [102] J. Wang, Y. Liu, S. Wang, X. Guo, Y. Liu, *J. Mater. Chem. A* 2 (2014) 1224–1229.
- [103] M.V. Reddy, C. Yao Quan, S. Adams, *Mater. Lett.* 212 (2018) 186–192.
- [104] X. Gu, J. Yue, L. Li, H. Xue, J. Yang, X. Zhao, *Electrochim. Acta* 184 (2015) 250–256.
- [105] W.-J. Yu, L. Zhang, P.-X. Hou, F. Li, C. Liu, H.-M. Cheng, *Adv. Energy Mater.* 6 (2016) 1501755.
- [106] S. Brutti, J. Hassoun, B. Scrosati, C.Y. Lin, H. Wu, H.W. Hsieh, *J. Power Sources* 217 (2012) 72–76.
- [107] J. Cabana, L. Monconduit, D. Larcher, M.R. Palacín, *Adv. Mater.* 22 (2010) 170–192.
- [108] Y. Zhao, J. Li, Y. Ding, L. Guan, *Chem. Commun.* 47 (2011) 7416.
- [109] V. Aravindan, Y.-S. Lee, S. Madhavi, *Adv. Energy Mater.* 7 (2017) 1602607.
- [110] S. Hwan Oh, J.S. Park, M. Su Jo, Y.C. Kang, J.S. Cho, *Chem. Eng. J.* 347 (2018) 889–899.
- [111] X. Liu, W. Si, J. Zhang, X. Sun, J. Deng, S. Baunack, S. Oswald, L. Liu, C. Yan, O.G. Schmidt, *Sci. Rep.* 4 (2015) 7452.
- [112] S. Chaudhari, M. Srinivasan, *J. Mater. Chem.* 22 (2012) 23049.
- [113] C. Xu, J. Sun, L. Gao, *J. Power Sources* 196 (2011) 5138–5142.
- [114] K. Chang, W. Chen, *Chem. Commun.* 47 (2011) 4252–4254.
- [115] J. Tian, Q. Shao, X. Dong, J. Zheng, D. Pan, X. Zhang, H. Cao, L. Hao, J. Liu, X. Mai, Z. Guo, *Electrochim. Acta* 261 (2018) 236–245.
- [116] G. Zhou, J. Ma, L. Chen, *Electrochim. Acta* 133 (2014) 93–99.
- [117] A. Palmieri, N. Spinner, S. Zhao, W.E. Mustain, *Carbon N. Y.* 130 (2018) 515–524.
- [118] K. Xu, *Chem. Rev.* 104 (2004) 4303–4417.
- [119] W. Li, H. Yao, K. Yan, G. Zheng, Z. Liang, Y.-M. Chiang, Y. Cui, *Nat. Commun.* 6 (2015) 7436.
- [120] W. Xu, J. Wang, F. Ding, X. Chen, E. Nasybulin, Y. Zhang, J.G. Zhang, *Energy Environ. Sci.* 7 (2014) 513–537.
- [121] S. Choudhury, R. Mangal, A. Agrawal, L.A. Archer, *Nat. Commun.* 6 (2015) 1–9.
- [122] J. Vetter, P. Novák, M.R. Wagner, C. Veit, K.-C. Möller, J.O. Besenhard, M. Winter, M. Wohlfahrt-Mehrens, C. Vogler, A. Hammouche, *J. Power Sources* 147 (2005) 269–281.

-
- [123] P. Verma, P. Maire, P. Novák, *Electrochim. Acta* 55 (2010) 6332–6341.
- [124] S. Tobishima, H. Morimoto, M. Aoki, Y. Saito, T. Inose, T. Fukumoto, T. Kuryu, *Electrochim. Acta* 49 (2004) 979–987.
- [125] Q.T. Qu, B. Wang, L.C. Yang, Y. Shi, S. Tian, Y.P. Wu, *Electrochem. Commun.* 10 (2008) 1652–1655.
- [126] F. Barzegar, D.Y. Momodu, O.O. Fashedemi, A. Bello, J.K. Dangbegnon, N. Manyala, *RSC Adv.* 5 (2015) 107482–107487.
- [127] G. Quijano, A. Couvert, A. Amrane, *Bioresour. Technol.* 101 (2010) 8923–8930.
- [128] D.J.S. Patinha, L.C. Tomé, C. Florindo, H.R. Soares, A.S. Coroadinha, I.M. Marrucho, *ACS Sustain. Chem. Eng.* 4 (2016) 2670–2679.
- [129] A.R. Neale, P. Goodrich, T.L. Hughes, C. Hardacre, S.C. Ball, J. Jacquemin, *J. Electrochem. Soc.* 164 (2017) H5124–H5134.
- [130] K.S. Ngai, S. Ramesh, K. Ramesh, J.C. Juan, *Ionics (Kiel)*. 22 (2016) 1259–1279.
- [131] A. Arya, A.L. Sharma, *Ionics (Kiel)*. 23 (2017) 497–540.
- [132] Y. Li, W. Zhang, Q. Dou, K.W. Wong, K.M. Ng, *J. Mater. Chem. A* 7 (2019) 3391–3398.
- [133] Z. Xue, D. He, X. Xie, *J. Mater. Chem. A* 3 (2015) 19218–19253.
- [134] M. Yan, W.-P. Wang, Y.-X. Yin, L.-J. Wan, Y.-G. Guo, *EnergyChem* 1 (2019) 100002.
- [135] S. Ramesh, K.N. Bing, *J. Mater. Eng. Perform.* 21 (2012) 89–94.
- [136] S. Ramesh, C.-W. Liew, E. Morris, R. Durairaj, *Thermochim. Acta* 511 (2010) 140–146.
- [137] X. Yao, B. Huang, J. Yin, G. Peng, Z. Huang, C. Gao, D. Liu, X. Xu, *Chinese Phys. B* 25 (2015) 018802.
- [138] P.-J. Lian, B.-S. Zhao, L.-Q. Zhang, N. Xu, M.-T. Wu, X.-P. Gao, *J. Mater. Chem. A* 7 (2019) 20540–20557.
- [139] D. Zhang, X. Xu, Y. Qin, S. Ji, Y. Huo, Z. Wang, Z. Liu, J. Shen, J. Liu, *Chem. – A Eur. J.* 26 (2020) 1720–1736.
- [140] A. Sakuda, A. Hayashi, M. Tatsumisago, *Sci. Rep.* 3 (2013) 2261.
- [141] L. Carbone, P.T. Moro, M. Gobet, S. Munoz, M. Devany, S.G. Greenbaum, J. Hassoun, *ACS Appl. Mater. Interfaces* 10 (2018) 16367–16375.
- [142] J.-D. Xie, W.-J. Liu, C. Li, J. Patra, Y.A. Gandomi, Q.-F. Dong, J.-K. Chang, *Electrochim.*

- Acta 319 (2019) 625–633.
- [143] D. Shanmukaraj, S. Lois, S. Fantini, F. Malbosc, M. Armand, *Chem. Mater.* 30 (2018) 246–251.
- [144] W.A. Henderson, *Macromolecules* 40 (2007) 4963–4971.
- [145] L. Carbone, M. Gobet, J. Peng, M. Devany, B. Scrosati, S. Greenbaum, J. Hassoun, *ACS Appl. Mater. Interfaces* 7 (2015) 13859–13865.
- [146] A. Benítez, D. Di Lecce, Á. Caballero, J. Morales, E. Rodríguez-Castellón, J. Hassoun, *J. Power Sources* 397 (2018) 102–112.
- [147] D. Morales, R.E. Ruther, J. Nanda, S. Greenbaum, *Electrochim. Acta* 304 (2019) 239–245.
- [148] B. Qin, S. Jeong, H. Zhang, U. Ulissi, D. Vieira Carvalho, A. Varzi, S. Passerini, *ChemSusChem* 12 (2019) 208–212.
- [149] S.S. Zhang, *J. Power Sources* 162 (2006) 1379–1394.
- [150] L. Carbone, D. Di Lecce, M. Gobet, S. Munoz, M. Devany, S. Greenbaum, J. Hassoun, *ACS Appl. Mater. Interfaces* 9 (2017) 17085–17095.
- [151] T. Yang, W. Fan, C. Wang, Q. Lei, Z. Ma, L. Yu, X. Zuo, J. Nan, *ACS Appl. Mater. Interfaces* 10 (2018) 31735–31744.
- [152] J. Li, J. Wang, X. He, L. Zhang, A. Senyshyn, B. Yan, M. Muehlbauer, X. Cao, B. Vortmann-Westhoven, V. Kraft, H. Liu, C. Luerenbaum, G. Schumacher, E. Paillard, M. Winter, J. Li, *J. Power Sources* 416 (2019) 184–192.
- [153] A. Ramanujapuram, G. Yushin, *Adv. Energy Mater.* 8 (2018) 1802624.
- [154] B.D. Adams, E. V. Carino, J.G. Connell, K.S. Han, R. Cao, J. Chen, J. Zheng, Q. Li, K.T. Mueller, W.A. Henderson, J.G. Zhang, *Nano Energy* 40 (2017) 607–617.
- [155] F. Qiu, X. Li, H. Deng, D. Wang, X. Mu, P. He, H. Zhou, *Adv. Energy Mater.* 9 (2019) 1803372.
- [156] L. Carbone, S.G. Greenbaum, J. Hassoun, *Sustain. Energy Fuels* 1 (2017) 228–247.
- [157] D. Di Lecce, L. Carbone, V. Gancitano, J. Hassoun, *J. Power Sources* 334 (2016) 146–153.
- [158] T. Placke, R. Kloepsch, S. Dühnen, M. Winter, *J. Solid State Electrochem.* 21 (2017) 1939–1964.
- [159] J. Qian, W.A. Henderson, W. Xu, P. Bhattacharya, M. Engelhard, O. Borodin, J.-G. Zhang,

- Nat. Commun. 6 (2015) 6362.
- [160] J. Park, J. Jeong, Y. Lee, M. Oh, M.-H. Ryou, Y.M. Lee, *Adv. Mater. Interfaces* 3 (2016) 1600140.
- [161] Y. Zhang, J. Yang, Y. Zhang, C. Li, W. Huang, Q. Yan, X. Dong, *ACS Appl. Mater. Interfaces* 10 (2018) 12722–12730.
- [162] B. Zhu, Y. Jin, X. Hu, Q. Zheng, S. Zhang, Q. Wang, J. Zhu, *Adv. Mater.* 29 (2017) 1603755.
- [163] X. Fan, L. Chen, O. Borodin, X. Ji, J. Chen, S. Hou, T. Deng, J. Zheng, C. Yang, S.-C. Liou, K. Amine, K. Xu, C. Wang, *Nat. Nanotechnol.* 13 (2018) 715–722.
- [164] D. Di Lecce, P. Andreotti, M. Boni, G. Gasparro, G. Rizzati, J.Y. Hwang, Y.K. Sun, J. Hassoun, *ACS Sustain. Chem. Eng.* 6 (2018) 3225–3232.
- [165] K. Ngamchuea, S. Eloul, K. Tschulik, R.G. Compton, *J. Solid State Electrochem.* 18 (2014) 3251–3257.
- [166] P.T. Kissinger, W.R. Heineman, *J. Chem. Educ.* 60 (1983) 702.
- [167] L. Nadjo, J.M. Savéant, *J. Electroanal. Chem. Interfacial Electrochem.* 48 (1973) 113–145.
- [168] R. Bernhard, A. Latini, S. Panero, B. Scrosati, J. Hassoun, *J. Power Sources* 226 (2013) 329–333.
- [169] D. Lin, Y. Liu, Y. Cui, *Nat. Nanotechnol.* 12 (2017) 194–206.
- [170] K. Zhang, G.-H. Lee, M. Park, W. Li, Y.-M. Kang, *Adv. Energy Mater.* 6 (2016) 1600811.
- [171] L. Carbone, T. Coneglian, M. Gobet, S. Munoz, M. Devany, S. Greenbaum, J. Hassoun, *J. Power Sources* 377 (2018) 26–35.
- [172] K. Xu, *Chem. Rev.* 114 (2014) 11503–11618.
- [173] L. Carbone, J. Peng, M. Agostini, M. Gobet, M. Devany, B. Scrosati, S. Greenbaum, J. Hassoun, *ChemElectroChem* 4 (2017) 209–215.
- [174] J. Evans, C.A. Vincent, P.G. Bruce, *Polymer (Guildf)*. 28 (1987) 2324–2328.
- [175] S.H. Lapidus, N.N. Rajput, X. Qu, K.W. Chapman, K.A. Persson, P.J. Chupas, *Phys. Chem. Chem. Phys.* 16 (2014) 21941–21945.
- [176] J. Wahlers, K.D. Fulfer, D.P. Harding, D.G. Kuroda, R. Kumar, R. Jorn, *J. Phys. Chem. C* 120 (2016) 17949–17959.
- [177] J. Peng, L. Carbone, M. Gobet, J. Hassoun, M. Devany, S. Greenbaum, *Electrochim. Acta* 213

- (2016) 606–612.
- [178] J. Heine, P. Hilbig, X. Qi, P. Niehoff, M. Winter, P. Bieker, *J. Electrochem. Soc.* 162 (2015) A1094–A1101.
- [179] L. Carbone, T. Coneglian, M. Gobet, S. Munoz, M. Devany, S. Greenbaum, J. Hassoun, *J. Power Sources* 377 (2018) 26–35.
- [180] B.A. Boukamp, *Solid State Ionics* 20 (1986) 31–44.
- [181] B. BOUKAMP, *Solid State Ionics* 18–19 (1986) 136–140.
- [182] D. Di Lecce, T. Hu, J. Hassoun, *J. Alloys Compd.* 693 (2017) 730–737.
- [183] D. Di Lecce, J. Hassoun, *J. Phys. Chem. C* 119 (2015) 20855–20863.
- [184] C. Zhang, A. Yamazaki, J. Murai, J.W. Park, T. Mandai, K. Ueno, K. Dokko, M. Watanabe, *J. Phys. Chem. C* 118 (2014) 17362–17373.
- [185] S. Wei, Z. Li, K. Kimura, S. Inoue, L. Pandini, D. Di Lecce, Y. Tominaga, J. Hassoun, *Electrochim. Acta* 306 (2019) 85–95.
- [186] D. Di Lecce, R. Brescia, A. Scarpellini, M. Prato, J. Hassoun, *ChemSusChem* 9 (2016) 223–230.
- [187] K. Zaghbi, A. Guerfi, P. Hovington, A. Vijh, M. Trudeau, A. Mauger, J.B. Goodenough, C.M. Julien, *J. Power Sources* 232 (2013) 357–369.
- [188] N. Meethong, Y.-H. Kao, W.C. Carter, Y.-M. Chiang, *Chem. Mater.* 22 (2010) 1088–1097.
- [189] A. Van der Ven, M. Wagemaker, *Electrochem. Commun.* 11 (2009) 881–884.
- [190] G.A. Elia, U. Ulissi, S. Jeong, S. Passerini, J. Hassoun, *Energy Environ. Sci.* 9 (2016) 3210–3220.
- [191] D. Aurbach, G. Eran, *Electrochim. Acta* 42 (1997) 697–718.
- [192] S.S. Zhang, *J. Power Sources* 161 (2006) 1385–1391.
- [193] G.A. Elia, U. Ulissi, F. Mueller, J. Reiter, N. Tsiouvaras, Y.-K. Sun, B. Scrosati, S. Passerini, J. Hassoun, *Chem. - A Eur. J.* 22 (2016) 6808–6814.
- [194] D. Di Lecce, R. Verrelli, J. Hassoun, *Electrochim. Acta* 220 (2016) 384–390.
- [195] T.Q. Nguyen, C. Breitkopf, *J. Electrochem. Soc.* 165 (2018) E826–E831.
- [196] P. Ravn Sørensen, T. Jacobsen, *Electrochim. Acta* 27 (1982) 1671–1675.
- [197] F. Wohde, M. Balabajew, B. Roling, *J. Electrochem. Soc.* 163 (2016) A714–A721.

-
- [198] D. Di Lecce, V. Gancitano, J. Hassoun, *ACS Sustain. Chem. Eng.* 8 (2020) 278–289.
- [199] D. Di Lecce, S. Levchenko, F. Iacoviello, D.J.L. Brett, P.R. Shearing, J. Hassoun, *ChemSusChem* 12 (2019) 3550–3561.
- [200] B. Ng, X. Peng, E. Faegh, W.E. Mustain, *J. Mater. Chem. A* 8 (2020) 2712–2727.
- [201] X. Sun, C. Yan, Y. Chen, W. Si, J. Deng, S. Oswald, L. Liu, O.G. Schmidt, *Adv. Energy Mater.* 4 (2014) 1300912.
- [202] Y. Wang, X. Guo, Z. Wang, M. Lü, B. Wu, Y. Wang, C. Yan, A. Yuan, H. Yang, *J. Mater. Chem. A* 5 (2017) 25562–25573.
- [203] R. Verrelli, R. Brescia, A. Scarpellini, L. Manna, B. Scrosati, J. Hassoun, *RSC Adv.* 4 (2014) 61855–61862.
- [204] H.H. Wei, Q. Zhang, Y. Wang, Y.J. Li, J.C. Fan, Q.J. Xu, Y.L. Min, *Adv. Funct. Mater.* 28 (2018) 1704440.
- [205] L. Lutterotti, D. Chateigner, S. Ferrari, J. Ricote, *Thin Solid Films* 450 (2004) 34–41.
- [206] I. Hasa, J. Hassoun, S. Passerini, *Nano Res.* 10 (2017) 3942–3969.
- [207] F. Zou, Y.M. Chen, K. Liu, Z. Yu, W. Liang, S.M. Bhaway, M. Gao, Y. Zhu, *ACS Nano* 10 (2016) 377–386.
- [208] D. Di Lecce, R. Verrelli, D. Campanella, V. Marangon, J. Hassoun, *ChemSusChem* 10 (2017) 1607–1615.
- [209] Y. Fu, Z. Yang, X. Li, X. Wang, D. Liu, D. Hu, L. Qiao, D. He, *J. Mater. Chem. A* 1 (2013) 10002–10007.
- [210] R. Verrelli, J. Hassoun, *ChemElectroChem* 2 (2015) 988–994.
- [211] M. Gauthier, T.J. Carney, A. Grimaud, L. Giordano, N. Pour, H.-H. Chang, D.P. Fenning, S.F. Lux, O. Paschos, C. Bauer, F. Maglia, S. Lupart, P. Lamp, Y. Shao-Horn, *J. Phys. Chem. Lett.* 6 (2015) 4653–4672.
- [212] G. Gabrielli, M. Marinaro, M. Mancini, P. Axmann, M. Wohlfahrt-Mehrens, *J. Power Sources* 351 (2017) 35–44.
- [213] D. Di Lecce, D. Campanella, J. Hassoun, *J. Phys. Chem. C* 122 (2018) 23925–23933.
- [214] S. Wei, S. Inoue, D. Di Lecce, Z. Li, Y. Tominaga, J. Hassoun, *ChemElectroChem* 7 (2020).
- [215] B. Scrosati, *J. Electrochem. Soc.* 139 (1992) 2776.

- [216] B. BOUKAMP, *Solid State Ionics* 20 (1986) 31–44.
- [217] B.P. Matadi, S. Geniès, A. Delaille, C. Chabrol, E. de Vito, M. Bardet, J.-F. Martin, L. Daniel, Y. Bultel, *J. Electrochem. Soc.* 164 (2017) A2374–A2389.
- [218] A. Friesen, F. Horsthemke, X. Mönnighoff, G. Brunklaus, R. Krafft, M. Börner, T. Risthaus, M. Winter, F.M. Schappacher, *J. Power Sources* 334 (2016) 1–11.

Publications and conferences

Publications

1. **S. Wei**, Z. Li, K. Kimura, S. Inoue, L. Pandini, D. Di Lecce, Y. Tominaga, J. Hassoun, Glyme-based electrolytes for lithium metal batteries using insertion electrodes: An electrochemical study, *Electrochimica Acta* 2019, 306, 85–95. IF = 5.383
2. **S. Wei**, S. Inoue, D. Di Lecce, Z. Li, Y. Tominaga, J. Hassoun, Towards a High-Performance Lithium-Metal Battery with Glyme Solution and an Olivine Cathode, *ChemElectroChem* 2020, 7, 2376–2388. IF = 4.154
3. **S. Wei**, D. Di Lecce, R. Brescia, G. Pugliese, P. R. Shearing, J. Hassoun, Electrochemical behavior of nanostructured NiO@C anode in a lithium-ion battery using LiNi_{1/3}Co_{1/3}Mn_{1/3}O₂ cathode, *Journal of Alloys and Compounds* 844 (2020) 155365. IF = 4.175
4. **S. Wei**, D. Di Lecce, J. Hassoun, A high-voltage, multi-metal LiNi_{0.35}Cu_{0.1}Mn_{1.45}Fe_{0.1}O₄ spinel cathode for lithium batteries, *Journal of The Electrochemical Society, Under review*, IF = 3.721
5. **S. Wei**, D. Di Lecce, R. M. D'Agostini, P. R. Shearing, J. Hassoun, α -Fe₂O₃@C anode in lithium-ion battery with LiFePO₄, LiNi_{1/3}Mn_{1/3}Co_{1/3}O₂, and LiNi_{0.5}Mn_{1.5}O₄ cathodes, *Submitted*.
6. **S. Wei**, J. Hassoun, Double substitution with copper and aluminum in spinel LiNi_{0.5}Mn_{1.5}O₄ towards high-performance lithium-ion battery, *Submitted*.
7. **S. Wei**, J. Hassoun, Electrochemical behavior of high voltage LiNi_{0.4}Fe_{0.1}Mn_{1.4}Al_{0.1}O₄ spinel cathode in lithium-ion battery using NiO@C anode, *Submitted*.

Conferences

1. S. Wei, Z. Li, K. Kimura, S. Inoue, L. Pandini, D. Di Lecce, Y. Tominaga, J. Hassoun, ECS 69th Annual Meeting of the International Society of Electrochemistry, Bologna, Italy, Sept. 2-7, 2018, **Poster**.
2. S. Wei, Z. Li, K. Kimura, S. Inoue, L. Pandini, D. Di Lecce, Y. Tominaga, J. Hassoun, XVIII Giornata della Chimica dell'Emilia Romagna, Parma, Italy, Dec. 17, 2018, **Poster**.
3. S. Wei, S. Inoue, D. Di Lecce, Z. Li, Y. Tominaga, J. Hassoun, XIX Giornata della Chimica dell'Emilia Romagna, Modena, Italy, Dec. 6, 2019, **Poster**.

Parts of this thesis have been already published in the following three papers:

S. Wei, Z. Li, K. Kimura, S. Inoue, L. Pandini, D. Di Lecce, Y. Tominaga, J. Hassoun, Glyme-based electrolytes for lithium metal batteries using insertion electrodes: An electrochemical study, *Electrochimica Acta* 2019, 306, 85–95.

<https://www.sciencedirect.com/science/article/pii/S0013468619304542>

Copyright © 2019 Elsevier Ltd. All rights reserved.

S. Wei, S. Inoue, D. Di Lecce, Z. Li, Y. Tominaga, J. Hassoun, Towards a High-Performance Lithium-Metal Battery with Glyme Solution and an Olivine Cathode, *ChemElectroChem* 2020, 7, 2376–2388.

<https://chemistry-europe.onlinelibrary.wiley.com/doi/full/10.1002/celec.202000272>

Copyright © 2020 Wiley-VCH Verlag GmbH & Co. KGaA, Weinheim

S. Wei, D. Di Lecce, R. Brescia, G. Pugliese, P. R. Shearing, J. Hassoun, Electrochemical behavior of nanostructured NiO@C anode in a lithium-ion battery using $\text{LiNi}_{1/3}\text{Co}_{1/3}\text{Mn}_{1/3}\text{O}_2$ cathode, *Journal of Alloys and Compounds* 844 (2020) 155365.

<https://www.sciencedirect.com/science/article/pii/S092583882031728X>

Copyright © 2020 Elsevier B.V. All rights reserved.

Acknowledgments

First and foremost, I am incredibly grateful to my supervisor Prof. Jusef Hassoun. Throughout the past three years, he has provided tremendous support, professional guidance, encouragement, motivation, and inspiration despite his busy schedule. It has been a pleasure to work under his supervision. I appreciate the pleasant working atmosphere, generous support of various group activities and conferences, as well as good opportunities to work independently in his research group. I am so grateful for this opportunity to be his first PhD student in the Department of Chemical and Pharmaceutical Sciences. His suggestions and guidance in the lithium battery field would be priceless.

Secondly, Dr. Daniele Di Lecce was exceptionally helpful, and I was touched by his efforts to make me feel welcome in our lab. Additionally, I would like to thank my colleagues, Mr. Vittorio Marangon, Mr. Loris Pandini, the visiting PhD students Miss. Celia Hernández-Rentero, Dr. Almudena Benítez for their fantastic teamwork.

During the first two years of this PhD program, I am honored to have an opportunity to collaborate with Prof. Yoichi Tominaga at Tokyo University of Agriculture and Technology, Graduate School of Bio-Applications and Systems Engineering (BASE). His collaborator Dr. Zhenguang Li, and Dr. Kento Kimura, and the rest of the group (Shoichi Inoue, Gnie Ramlee), who made my stay become an enjoyable experience.

I would also like to thank the technical staff, Daniela Palmeri, to assist in data collection and her kind help, as well as the staffs of IUSS offices, Daniela Siri, Elena Caniato, and Lena Fabbri, to send and prepare all types of documents and their patience and friendliness.

Special thanks go to my friends, Min Li, Elisabeth Sandra Dewi Oktaviani, Zhifu Feng, Jinlu Liang, Tien Nguyen Thi Minh, and Giao Nguyen for providing the kindness that now makes Italy feel like a second home to me.

I also must thank my parents (Guojian Wei and Xiangyan Jiang), my brother (Cao Wei), my grandmother (Fengying Yi), my aunt (Guoyuan Wei), and my uncle (Hua Jiang) for their love, understanding, unwavering support, and encouragement throughout my PhD and all other aspects of my life at any other time.

University of Ferrara Nov. 2020

Resume

Personal information

Full name: Shuangying Wei
Date/Place of Birth: Sept. 17. 1991/Hunan, China
Nationality: Chinese
Gender: Female

Education

Nov. 2017 – now PhD student in Chemical Science,

University of Ferrara, Italy

Sep. 2014 – Jul. 2017 Master of Physical Chemistry,

Xiangtan University, China

Sep. 2010 – Jul. 2014 Bachelor of Chemistry,

Hengyang Normal University, China

Research Experience

Nov. 2017 - now University of Ferrara, Ferrara, Italy.

Topic: Advance electrolyte and electrode material for high performance lithium battery.

Sep. 2018 – Nov. 2018 Tokyo University of Agriculture and Technology, Graduate School of Bio-Applications and Systems Engineering (BASE), Tokyo, Japan.

Visiting student, topic: Glyme electrolyte for lithium metal battery.

Language

Mandarin: native

English: fluent

Italian: basic